



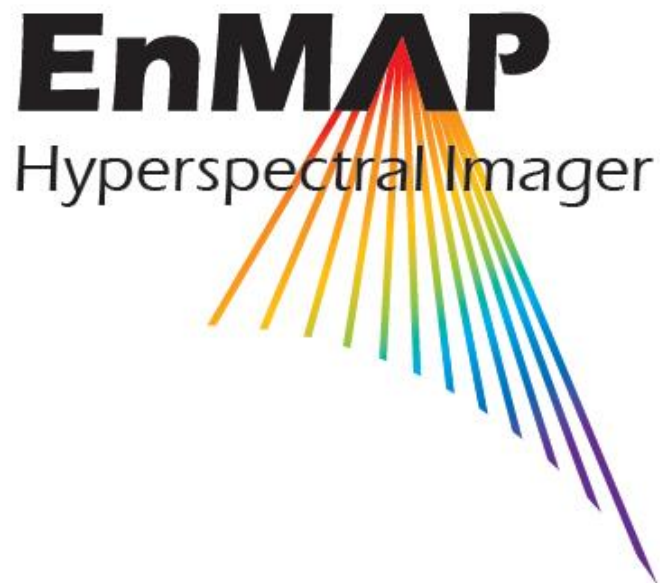
EnMAP Ground Segment

Level 1C Processor (Geometric Correction) ATBD

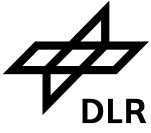
Restriction: Public

Doc. ID	EN-PCV-TN-5006
Issue	1.7
Date	07.10.2024

Under Configuration Control: Yes



German Remote Sensing Data Center (DFD)
Remote Sensing Technology Institute (IMF)
German Space Operation Center (GSOC)



– blank page –



TABLE OF SIGNATURES

Prepared

Date	Mathias Schneider Subsystem Engineer DEV
------	---

Reviewed

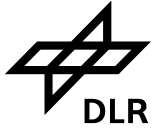
Date	Peter Schwind Subsystem Manager DEV
------	--

Approved

Date	Miguel Pato System Manager PCV
------	-----------------------------------

Released

Date	Emiliano Carmona GS Project Manager
------	--





DISTRIBUTION LIST

This EnMAP Ground Segment document is stored in the Design Definition File (DDF) of the EnMAP Ground Segment Teamsite.

This document is accessible by all participants of the EnMAP Ground Segment as well as by the EnMAP Ground Segment Customer. This document may be further distributed by the EnMAP Project Management as necessary.

After commissioning phase, the document is provided to the EnMAP user community on www.enmap.org.

CHANGE RECORD

Version	Date	Chapter	Comment
0.80	29.08.2009	all	Draft Version
1.00	01.06.2010	all	First issue
1.10	12.08.210	4.4	Adjustment of figure; flight direction arrow changed [VON-A-0317]
		5.4.2	Explanation of angles between master STS and HSI [VON-A-0321]
	06.09.2010	6.3	Improvement of inclusion of this chapter [VON-A-0321 c)
	22.10.2010	6.4.2,6.4.4	Elimination of cost calculation and revision of corresponding document sections [VON-A-0322]
1.2	29.03.2016	all	Adaptions due to new product level names L2geo->L1C, L1-> L1B, L2->L2A, no L2atm product anymore, also changed in document name (SCR-00018)
		6.3, 6.4.2, 6.4.3, 6.4.4., 6.4.5, 6.5,	Removed, obsolete (SCR-00044)
		5.6.1	Added Tandem-X DEM as possible source for global DEM database (SCR-00044)
	06.04.2016	5.9	Added chapter on geolayer generation (SCR-00044)
		7	Added chapter on rational polynomial functions (SCR-00044)
		6.3	Added chapter on SIFT matching (SCR-00044)
	07.04.2016	6.4.2	Added chapter on possible sources for global reference databases (SCR-00044)
	28.04.2016	5.5.3	Least Squares Spline Interpolation for attitude reconstruction added and noted that this is now the baseline (SCR-00044)
1.3	23.12.2016	6.1	Clarified text on preparation of images for matching according to GSDCDR RID FIS-S-0045
		5.8.4	Added chapter and TBD on handling of dead pixels according to GSDCDR RID FIS-S-0041.
		5.4.3, 2.2	Added statement on effect different wavelengths for atmospheric refraction correction according to GSDCDR RID FIS-S-0037, added reference [RD-57]
		15	Updated due dates of TBCs/TBDs
1.4	13.11.2020	15, 5.8.4, 5.5.1	Removed TBDs on Dead Pixel Handling and JitterCorrectionTime
		5.5.2	Changed Position Interpolation from Lagrange to Spline Approximation
		5.6.1	Changed database to COP30 DEM, removed TBD
		6.4.2	Changed database to Sentinel-2 images
		6.5.2	Removed section on determination of weights, as a consistent reference image database is used. Removed TBD.
		6.5.2	Removed TBD on blunder reduction techniques
		5.7.1	Added clarification on UPS projection
		Table of signatures	Replaced Gintautas Palubinskas by Emiliano Carmona
1.5	29.07.2021	5.7.2, 5.7.3	Added clarification on Geographic and LAEA projections (fallback to UTM) according to ICR-00198-04
	12.01.2022	5.4.1	Updated calculation of interior orientation to fit with OHB delivery, added values for polynomial coefficients. Added reference
	17.01.2022	15	Updated table of TBC/TBD
	17.01.2022	2.1	Updated issue numbers for reference documents
1.6	27.09.2022	5.4.2	Added statement that during commissioning phase STS 1 is selected as master STS, added initial mounting angles
		Header, distribution list	Changed restriction from mission internal to public
		2.1	Updated version numbers
1.7	07.10.2024	10	Added chapter 10 on viewing angles in metadata
		Table of signatures	Updated table of signatures



Document Preparation

The EnMAP Ground Segment "Level 1C Processor" ATBD was prepared with contributions from DLR personnel as listed below.

First Name, Last Name	Organizational Unit / Chapters
Remote Sensing Technology Institute / Institut für Methoden der Fernerkundung (DLR-MF)	
Mathias Schneider	MF-PB Chapters 6.2/ 6.3/ 6.4.2/ 7/ 10
Rupert Müller	MF-PB Chapters 4/ 5/ 6.1/ 6.5/ 8/ 9/ 11/ 12/ 13/ 14/ 15
Peter Schwind	MF-PB Chapters 8.1
German Remote Sensing Data Center / Deutsches Fernerkundungsdatenzentrum (DLR-DFD)	
Heike Gerighausen	DFD-BN Chapters 6.4.1

EXTERNAL Document REVIEW

Dr.-Ing. Karsten Jacobsen
Institut für Photogrammetrie und GeoInformation
Nienburger Str.1
D-30167 Hannover

reviewed on 17.05.2010
comments from external review processed and included in the document



CONTENTS

1. Introduction	12
1.1 Purpose	12
1.2 Scope	12
2. Applicable and Reference Documents	12
2.1 Applicable Documents	12
2.2 Reference Documents	13
3. Terms, Definitions and Abbreviations	15
4. Overview	16
4.1 What is Orthorectification.....	16
4.2 Which Orthorectification Methods and Algorithms exist	16
4.3 Which Geometric Correction Method is used for EnMAP	16
4.4 The EnMAP Mission and Instrument Characteristics.....	18
4.5 The EnMAP Processing Chain and the generated Products	19
4.6 How Image Tiles are processed	20
5. Algorithm Description of Direct Georeferencing	22
5.1 Direct Georeferencing (generic)	22
5.2 EnMAP Satellite Coordinate Frames and Alignment Cubes	23
5.3 Direct Georeferencing (EnMAP HSI)	24
5.4 Line-Of-Sight Vector.....	24
5.4.1 Interior Orientation	24
5.4.2 Instrument Mounting Angles (Boresight Alignment Angles)	28
5.4.3 Atmospheric Refraction Correction	29
5.4.4 Attitude	30
5.4.5 Light Aberration (Speed of Light Correction)	32
5.4.6 State Vector	32
5.5 Time Synchronization and Approximation	32
5.5.1 Time Scale for Data Synchronization	32
5.5.2 Position and Velocity Approximation	33
5.5.3 Attitude Approximation	33
5.6 DEM Intersection Model	34
5.6.1 Global DEM Database	34
5.6.2 Iterative Determination of Object Points.....	35
5.7 Map Projections	36
5.7.1 Universal Transverse Mercator UTM	36
5.7.2 Geographic	36
5.7.3 Lambert Azimuthal Equal Area ETRS89 (European Projection)	37
5.8 Image Resampling	37
5.8.1 Nearest Neighbor	38
5.8.2 Bilinear.....	38
5.8.3 Cubic Convolution.....	38
5.8.4 Dead pixel handling	38
5.9 Geolayer Generation	39
6. Improvements of Sensor Model Parameters	39
6.1 Processing Chain for Orthorectification	39
6.2 Intensity based Image Matching	41
6.2.1 Basic concept	41
6.2.2 Blunder reduction	44
6.3 SIFT Matching	44
6.4 Optical Reference Image Databases	44
6.4.1 Requirements for Reference Database	45
6.4.2 Reference Database	45
6.5 Mathematics of Model Parameter Estimation (inverse modeling)	45
6.5.1 Least Squares Adjustment.....	45



6.5.2	Blunder Detection	47
7.	Rational Polynomial Functions.....	49
7.1	Generation of Rational Polynomial Coefficients	49
8.	VNIR – SWIR Co-registration	50
8.1	Simulation of Co-registration Accuracy	50
9.	Product Quality Indicators.....	51
9.1	Root Mean Square Values (orthoRMSE)	51
9.2	Residual Plot (orthoResidual)	52
9.3	DEM related Errors (orthoTerrain)	52
10.	Metadata.....	52
10.1	Scene Azimuth Angle	53
10.2	Off-Nadir Angles	53
10.3	Viewing Zenith Angle.....	54
10.4	Viewing Azimuth Angle	55
11.	Verification	55
11.1	Standard Geometric Processing.....	55
11.2	Auxiliary Geometric Processing.....	56
11.2.1	Image2006	56
11.2.2	UrbanAtlas	58
12.	Output	60
13.	Appendix A: Orthogonal Transformations (Basics).....	61
14.	Appendix B: Definitions of Coordinate Frames and Transformations	64
14.1	Geocentric Earth Fixed Cartesian Coordinate frame (ECEF or ECR)	64
14.2	Ellipsoidal Geographic Coordinate Frame	64
14.3	Local Topocentric Frame (LTS).....	64
14.4	Transformation between Geographic and Geocentric Coordinate Frames	65
14.5	Transformation between Geocentric (ECR) and Local Topocentric (LTS) Coordinate Frame	66
14.6	Geodetic Datum	66
14.7	Map Projections	67
14.8	Geoid and Ellipsoid Heights	67
14.9	Quasi Inertial Coordinate Frame (ECI Earth Centered Inertial)	68
15.	Appendix C: Composed Rotation Matrix and Rotation Angle Extraction	70
16.	List of On-Going TBC & TBD	72

LIST OF FIGURES

Figure 4-1	4-step Process of Orthorectification	17
Figure 4-2	EnMAP mission and instrument characteristics	18
Figure 4-3	EnMAP HSI Processing Chain	20
Figure 4-4	Simulation of time synchronized overlay of the VNIR and SWIR part of a L1B product (descending orbit). Green: VNIR tile; Red: SWIR tile. The usable overlap area is about 1004 lines x 998 columns depending on the latitude (loss of about 2% of data)	20
Figure 4-5	Tile processing by orthorectification. The example shows a data take with 3 image tiles. The second tile is the current one which is processed. The right part shows a seamless mosaic of the three orthorectified tiles.	21
Figure 5-1	Concept of Direct Georeferencing	22
Figure 5-2	Scheme of coordinate frames and alignment cubes of the EnMAP satellite. The blue dashed arrows show the alignment measurements on ground between the coordinate frames using the installed alignment cubes. The red arrows show the coordinate frame transformations finally used in the geometric correction processor L1C.	23
Figure 5-3	Definition of object sided pixel view direction angles	26
Figure 5-4	Method of determination of the actual sensor look direction with the DEM by an iterative approach	35
Figure 5-5	Polygons (triangles) of the input image, defined by the center of adjacent pixels, are transformed to the pixel grid of the orthoimage and filled with bilinear interpolated pixel value	37
Figure 6-1	Overview of orthorectification using automatically extracted GCP	40
Figure 6-2	Processing scheme of the matching algorithm	42
Figure 6-3	Histogram of the residuals ($RMSE_{xy}$) after least squares adjustment for one SPOT 4 HRVIR scene. Dark bars: before blunder removal; bright bars: after blunder removal using 2 pixel sizes as GCP rejection level.	47
Figure 6-4	Histogram of the residuals ($RMSE_{xy}$) after least squares adjustment for 100 SPOT 4 HRVIR and SPOT 5 HRG scenes. Dark bars: before blunder removal; bright bars: after blunder removal using 2 pixel sizes as GCP rejection level.	48
Figure 7-1	Virtual object points from rigorous sensor model to estimate RPC by least squares adjustment	49
Figure 8-1	Example of the approximation of the attitude controller deviation. Blue: the real deviation; Green: periodic attitude measurements including pointing knowledge error; Red: Approximated deviation for the duration of an EnMAP scene	50
Figure 9-1	Example of a residual plot, which shows the deviations in pixel – here by factor 55 enlarged - of automatically determined ICPs from the reference image versus image coordinates of the orthorectified scene after correction with GCPs	52
Figure 10-1:	Scene azimuth angle (nadir case)	53
Figure 10-2:	Along-track (θ) and across-track (β) off-nadir angles	54
Figure 10-3:	Viewing zenith and azimuth angle	55
Figure 11-1	Geometric accuracy (RMSE) of Image2006 products w.r.t. reference images (relative accuracy). $RMSE_x$ (blue) and $RMSE_y$ (red) for European coverage 1 (first two columns of country) and European coverage 2 (last two columns of country)	57
Figure 11-2	Geometric accuracy (RMSE) of ALOS AVNIR-2 orthorectified scenes w.r.t. reference images (relative accuracy). $RMSE_x$ (blue) and $RMSE_y$ (red)	59
Figure 14-1	Definition of local topocentric system (LTS) and earth centered earth fixed (ECEF) coordinate system	65
Figure 14-2	Steps to change a map projection	67
Figure 14-3	Height definitions used for digital elevation models DEM	68



LIST OF TABLES

Table 5-1	Mnemonic synonym of coordinate frame terms.....	24
Table 5-2	Description of the collinearity equation components	24
Table 5-3	Definition of Sensor Coordinate Frame	25
Table 5-4	Initial (pre-launch) polynomial coefficients to calculate the look direction angles for pixels of the VNIR and SWIR instrument. Values from OHB laboratory calibration, AD-21. .	26
Table 5-5	Definition of Body Coordinate Frame	28
Table 5-6	Initial mounting angles valid for the VNIR and SWIR instrument (after first update during commissioning phase)	29
Table 5-7	Name of coefficients used in the product metadata file	29
Table 5-8	Definition of ECR Coordinate Frame.....	30
Table 5-9	Displacements caused by DEM error	34
Table 5-10	Supported Map Projection.....	36
Table 5-11	Supported image resampling methods	37
Table 6-1	Methods of image matching techniques	41
Table 8-1	Absolute mean displacement and standard deviation between the matches found in the orthorectified VNIR and SWIR images in meters (generated over 1000 iterations)	50
Table 10-1	Pointing knowledge simulated with sensor model used for EnMAP (not all error influences are included)	56
Table 10-2	Absolute geometric accuracy for different zones in Europe determined by different operators to increase the reliability.	57

1. Introduction

1.1 Purpose

This document describes all aspects of geometric processing of the EnMAP hyperspectral data. The content of the document is as far as possible self-contained for external use. It therefore contains an extended overview including mission, satellite and instrument characteristics. The document describes the algorithms for the geometric correction of Level 1B (L1B) data in order to generate

- Level 1C (L1C) products

1.2 Scope

This EnMAP Ground Segment ATBD (Algorithm Theoretical Basis Document) is structured as follows:

- Chapters 1 to 3 are the usual ECSS prompted introductory chapters.
- Chapter 4 introduces to the principles of geometric correction of optical satellite images. It gives a short overview of the mission, the instrument, the processing chain and the products.
- Chapter 5 describes the geometrical model. This chapter is the most important one for external users who like to develop own geometric correction SW.
- Chapter 6 describes the method to improve the geometric accuracy by automatically extracted ground control information using global reference image databases.
- Chapter 7 describes the generation of rational polynomial coefficients (RPCs).
- Chapter 8 describes the co-registration of data from the two instruments VNIR and SWIR
- Chapter 9 describes the product quality indicators
- Chapter 10 describes metadata entries on the viewing angles
- Chapter 11 describes the verification of the used algorithms
- Chapter 12 describes the Output of the L1C processor
- Chapters 13, 14 and 15 are appendices to clarify and amplify the mathematics and coordinate frame definitions
- Chapter 16 contains the TBC/TBD list

2. Applicable and Reference Documents

2.1 Applicable Documents

The following documents are applicable to the extent specified herein.

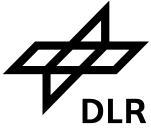
Document ID	Document Title	Issue
AD-01	EN-KT-DD-001 EnMAP Design Document – Instrument, Volume III	4
AD-02	EN-OHB-DD-006 Attitude Control Subsystem – Design Description	5
AD-03	EN-OHB-TN-005 S/C Bus ACS Performance Analysis	3
AD-04	EN-PCV-TN-6007 Level 2A Processor (Atmospheric Correction – Land) ATBD	2.4
AD-05	EN-PCV-TN-8005 HSI Geometric Calibration and Quality Control Concept	1.4
AD-06	EN-PCV-DD-8004 Quality Control Design Document	1.4
AD-07	EN-PCV-TN-1004 Definition of Product Levels	1.2
AD-08	EN-PCV-ICD-2009-1 EnMAP HSI Level 0 Product Specification Document	1.6
AD-09	EN-PCV-ICD-2009-2 EnMAP HSI Level 1/Level 2 Product Specification Document	1.9
AD-11	EN-PCV-ICD-7008 Calibration Data Product Specification	1.7
AD-12	EN-PCV-ICD-2002 PCV-Internal-ICD	1.6
AD-13	EN-PCV-RSP-2013 PCV System Requirements Specification	1.3
AD-14	EN-KT-TN-031 Algorithms for Data Processing	11
AD-15	EN-KT-PL-005 Calibration Characterization Plan	5
AD-16	EN-PCV-DD-2004 Processor Design Document	1.6
AD-17	EN-PCV-TN-4006 Level 1B Processor (Systematic and Radiometric Correction) ATBD	1.9
AD-19	EN-GS-DD-2011 Product Conventions	1.4
AD-20	EN-KT-RP-009 Technical Budgets	4
AD-21	EN-KT-RP-835 HSI Characterization & Calibration Report	1

2.2 Reference Documents

The following documents, though not formally part of this document, amplify or clarify its content.

Document ID	Document Title
RD-01	Toutin, T. (2004). Geometric Processing of Remote Sensing Images: Models, Algorithms and Methods. International Journal of Remote Sensing, vol. 25, no. 10, pp. 1893-1924(32).
RD-02	Jacobsen, K. (2008). Geometric modelling of linear CCDs and panoramic imagers. In: Li, Z.; Chen, J.; Baltasvias, E. (Hrsg.): Advances in Photogrammetry, Remote Sensing and Spatial Information Science. London: Taylor and Francis, 2008, S. 145-155
RD-03	Daniela Poli (2005): Modelling of Spaceborne Linear Array Sensors; Diss. ETH NO. 15894; Institut für Geodäsie und Photogrammetrie; ETH Zürich; ISBN 3-906467-50-3.
RD-04	Müller, Rupert; Lehner, Manfred; Reinartz, Peter; Schroeder, Manfred (2005): EVALUATION OF SPACEBORNE AND AIRBORNE LINE SCANNER IMAGES USING A GENERIC ORTHO IMAGE PROCESSOR. In: Heipke, C.; Jacobsen, K.; Gerke, M. [Hrsg.]: High Resolution Earth Imaging for Geospatial Information, IAPRS, Vol. XXXVI, High Resolution Earth Imaging for Geospatial Information, Hannover, 17.-20. Mai 2005, ISBN ISSN No. 1682-1777. http://www.isprs.org/publications/related/hannover05/paper/046-mueller.pdf
RD-05	Müller, Rupert, Krauß, Thomas, Lehner, Manfred, Reinartz, Peter, Schroeder, Manfred, Hörsch, Bianca (2008): GMES Fast Track Land Service 2006-2008 - Orthorectification of SPOT 4/5 and IRS-P6 LISS III Data. In: ISPRS Congress Beijing 2008, 2008, Beijing. http://www.isprs.org/congresses/beijing2008/proceedings/7_pdf/11_SS-7/04.pdf
RD-06	Reinartz, P., Müller, R., Lehner, M., Schroeder, M. (2006): Accuracy Analysis for DSM and orthoimages derived from SPOT HRS Stereo Data using Direct Georeferencing, ISPRS Journal of Photogrammetry and Remote Sensing, Vol. 60/3, (2006), pp. 160-169
RD-08	Lehner M. and Gill R.S. (1992): Semi-automatic derivation of digital elevation models from stereoscopic 3-line scanner data, IAPRS, Vol. 29, Part B4, Washington, USA, pp. 68-75.
RD-09	Roth, A.; Knöpfle, W.; Strunz, G.; Lehner, M.; Reinartz, P. (2002): "Towards a Global Elevation Product: Combination of Multi-Source Digital Elevation Models", Symposium on Geospatial Theory, Processing and Applications, Ottawa, 2002
RD-10	Stuffer, T.; Hofer, S.; Leopold, M.; Förster, K.-P.; Sang, B.; Schubert, J.; Penné, B.; Kaufmann, H.; Müller, A.; Chlebek, C. (2009): EnMAP – Space Segment – Instrument and Mission Parameters. In: EARSeL SIG-IS Workshop, Tel Aviv, Israel.
RD-11	Lehner M., Gill, R.S., 1992: "Semi-Automatic Derivation of Digital Elevation Models from Stereoscopic 3-Line Scanner Data", IAPRS, Vol. 29, part B4, Commission IV, pp. 68-75, Washington, USA
RD-12	Kornus W., Lehner M., Schroeder, M., 2000, "Geometric inflight calibration by block adjustment using MOMS-2P 3-line-imagery of three intersecting stereo-strips", SFPT (Société Française de Photogrammétrie et Télédétection), Bulletin Nr. 159, pp. 42-54
RD-13	Map Projections of Europe; European Commission, JRC; 2003 A. Annoni, C. Luzet, E. Gubler and J. Ihde http://www.ec-gis.org/sdi/publist/pdfs/annoni-et-al2003eur.pdf
RD-14	OGP Surveying and Positioning Guidance Note number 7, part 2 – November 2009; Coordinate Conversions and Transformations including Formulas; Revised - November 2009 http://www.epsg.org/guides/docs/G7-2.pdf
RD-25	Schwind, P., Müller, R., Storch, T., Makasy, C.; A geometric simulator for the hyperspectral mission EnMAP, in ISPRS symposium 2010
RD-27	Müller, R., Bachmann, M., Makasy, C., De Miguel, A., Müller, A., Neumann, A., Palubinskas, G., Richter, R., Schneider, M., Storch, T., Walzel, T., Kaufmann, H., Guanter, L., Segl, K., Heege, T., Kiselev, V., 2010. The Processing Chain and Cal/Val Operations of the Future Hyperspectral Satellite Mission EnMAP. IEEE . 2010 IEEE Aerospace Conference, 6.-13. März 2010, Big Sky, USA. ISBN 978-1-4244-3888-4. ISSN 1095-323X
RD-28	Schwind, P., Schneider, M., Palubinskas, G., Storch, T., Müller, R., Richter, R., 2009. Processors for ALOS Optical Data: Deconvolution, DEM Generation, Orthorectification, and Atmospheric Correction, IEEE Transactions on Geoscience and Remote Sensing, doi: 10.1109/TGRS.2009.2015941.
RD-29	Müller, R., Lehner, M., Reinartz, P., Schroeder, M., Vollmer, B., 2002. A program for direct georeferencing of airborne and spaceborne line scanner images. In: IAPRS, Vol. XXXIV, part 1, ISSN 1682-1750, edited by S Morain & A Budge (ISPRS Comm.I)
RD-30	EN-PCV-TN-1003 Comments on Keystone, Smile, Co-registration
RD-31	EN-GS-TN-6007 Comments on Sun Calibration and Pointing Knowledge

RD-32	Bannari, A., Morin, D., Be´ Nie´ , G. B., Bonn, F. J. (1995): A theoretical review of different mathematical models of geometric corrections applied to remote sensing images. <i>Remote Sensing Reviews</i> , 13, pp. 27–47.
RD-36	Bronstein I. N., Semendjajew K. A. (1991): Taschenbuch der Mathematik, Teubner Verlagsgesellschaft Stuttgart, Leipzig, Nauka Moskau, 25. Auflage.
RD-37	Brown, L. G. (1992): A survey of image registration techniques. <i>ACM Computing Surveys</i> , 24(4), pp. 325-376.
RD-38	Davis, J.C. (1986): <i>Statistics and Data Analysis in Geology</i> . - John Wiley & Sons New York (2nd Edition).
RD-39	Dai, X. L., Khorram, S. (1999): A Feature-based Image Registration Algorithm using Improved Chain Code Representation Combined with Moment Invariants. <i>IEEE Trans. on Geoscience and Remote Sensing</i> , 37(5), pp.2351-2362.
RD-43	Harrison, B.A. (1995): <i>Remote Sensing: Image Rectification and Registration Volume 4</i> , CSIRO Publishing.
RD-48	Toutin, T. (2004): Review article: Geometric processing of remote sensing images: models, algorithms and methods. <i>Int. J. Remote Sensing</i> , 25, pp. 1893–1924.
RD-49	Ventura, A. D., Rampini, A., Schettini, R. (1990): Image registration by recognition of corresponding structures. <i>IEEE Trans. Geoscience and Remote Sensing</i> , 28(3), pp. 305-314.
RD-50	Schwind, P. (2008): Critical Evaluation of the SIFT Operator for Remote Sensing Imagery, Diploma Thesis, Fachhochschule Landshut
RD-51	S. J Baillarin, A. Meygret, C. Dechoz, B. Petrucci, S. Lacherade, T. Tremas, C. Isola, P. Martimort, F. Spoto (2012): SENTINEL-2 LEVEL 1 PRODUCTS AND IMAGE PROCESSING PERFORMANCES. <i>International Archives of the Photogrammetry, Remote Sensing and Spatial Information Sciences</i> , Volume XXXIX-B1, XXII ISPRS Congress, 25 August – 01 September 2012, Melbourne, Australia
RD-52	http://landsat.usgs.gov/science_GLS.php
RD-53	SciPy, 2011. Scientific Tools for Python. < http://www.scipy.org/ > (accessed 09.08.11).
RD-54	Dierckx, P., 1993. <i>Curve and Surface Fitting with Splines</i> . Monographs on Numerical Analysis. Oxford University Press.
RD-55	P. Schwind, R. Müller, G. Palubinskas, and T. Storch, "An indepth simulation of EnMAP acquisition geometry," <i>ISPRS Journal of Photogrammetry and Remote Sensing</i> , 70, pp. 99-106, 2012.
RD-56	https://spacedata.copernicus.eu/web/cscda/dataset-details?articleId=394198
RD-57	Noerdlinger, P., 1999 Atmospheric refraction effects in Earth remote sensing, <i>ISPRS Journal of Photogrammetry and Remote Sensing</i> , 54:360–373.
RD-58	Copernicus Digital Elevation Model Product Handbook, AIRBUS Defence and Space, https://spacedata.copernicus.eu/documents/20126/0/GEO1988-CopernicusDEM-SPE-002_ProductHandbook_11.00.pdf/082dd479-f908-bf42-51bf-4c0053129f7c?t=1586526993604



3. Terms, Definitions and Abbreviations

Terms, definitions and abbreviations for the EnMAP Ground Segment and the EnMAP Space are collected and published on <http://www.enmap.org/> together with the mission description.

4. Overview

The geometric correction of remotely sensed image data is one of the key issues in data interpretation, added value product generation and multi-source data integration. It is one of the main processing steps prior to further evaluation of the image data – namely fusion and analysis with data from different sources and times, overlaying with existing data sets or maps, change detection, map updating or integration into Geographic Information Systems (GIS). Each image acquisition system like the Hyper-Spectral Imager (HSI) on the EnMAP (Environmental Mapping and Analysis Program) satellite produces geometric distorted raw imagery caused by the satellite / sensor system itself (e.g. camera internal geometry, satellite attitude and position changes during data acquisition) as well as external effects (e.g. terrain displacements, light refraction by the Earth atmosphere). Additionally end-users need for their applications images, which are transformed to a map projection system.

Today well geometric characterized sensor systems, high precision on-board position determination with Global Navigation Systems (GNS) in combination with integrated attitude measurements using Star Tracker Systems (STS) and Inertial Measurement Units (IMU) as well as accurate Digital Elevation Models (DEM) allow physically understanding and describing the image generation process. Therefore a geometric correction of the raw images with certain accuracy is possible depending on the accuracies of the on-board measuring systems. For the EnMAP mission the specification for the pointing knowledge is 100 m (at nadir and sea level, LE68) according to about 3 Ground Sampling Distances (GSD). In order to achieve geometric accuracies better than one GSD the parameters of the sensor model have to be improved using Ground Control Point (GCP) information. Within an operational processing chain the GCP have to be extracted automatically from existing reference images (already geometric corrected image data) of superior geometric quality. This procedure leads to high quality geometric corrected images (orthorectified products) or at least to a geometric consistent EnMAP data set in terms of relative accuracy.

4.1 What is Orthorectification

Orthorectification is the process to convert imagery into map-accurate forms by removing sensor, satellite motion and terrain related geometric distortions from raw imagery. Orthorectification – also called *explicit geocoding* due to explicit image resampling– belongs to the generic term Georeferencing, which is the process of assigning data - e.g. streets, home addresses or image pixels - to geo-spatial reference information (e.g. earth bound coordinate frames like longitude / latitude).

4.2 Which Orthorectification Methods and Algorithms exist

Today various methods and models of different complexity exist for geometric correction of optical sensor data, which are based on affine (or higher order polynomial) transformations, Direct Linear Transformation (DLT), Rational Polynomial Functions (RPF) or Direct Georeferencing (DG) techniques. Mainly two approaches are in common use: First the rigorous sensor models as used in DG techniques, which describes physically the image generation process from the focal plane location of an instrument pixel to an earth surface location in terms of earth bound coordinate frames, and second universal sensor models like RPF, which provides a standardized and easy to use mathematical model to map object coordinates to image column and row values of the original image. Empirical methods always need Ground Control Points (GCP) to produce orthoimages, whereas physical based models also work without GCP using measurements like position and attitude during image acquisition and laboratory / in-flight geometric calibration values. GCP (in most cases only few) for the physical models are used for fine adjustment. Very good overviews of existing correction methods can be found in [RD-01] [RD-02] [RD-03].

4.3 Which Geometric Correction Method is used for EnMAP

For the EnMAP HSI instrument a physical sensor model is used employing the method of Direct Georeferencing. This sensor model is based on a pixel Line-of-Sight (LoS) model, which extensively utilizes on-board measurements from Star Tracker Systems, Inertial Measurement Units (gyros), Global Positioning System (GPS) as well as the geometric sensor characterization by laboratory and/or in-flight calibration. The 4-step process of orthorectification is illustrated in Figure 4-1, which additionally shows derivational products used as independent product or as starting point to complete orthorectification.

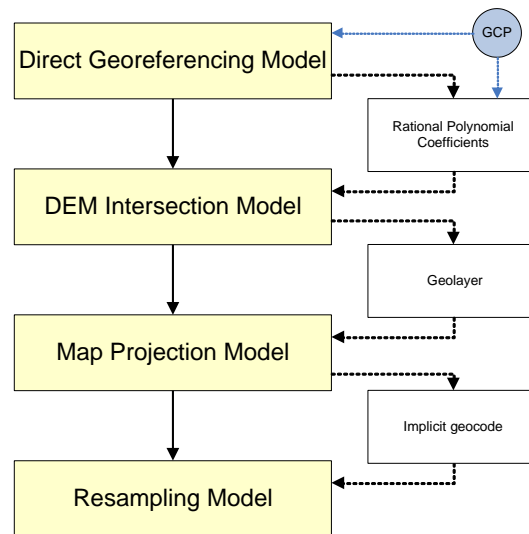


Figure 4-1 4-step Process of Orthorectification

Step 1 Direct Georeferencing Model

- Synchronization of attitude and position/velocity measurements with time tagged image lines using appropriated interpolation
- Establishment of the pixel view vectors (also called pixel Line-of-Sight LoS vector) using the sensor internal geometry, payload assembly geometry and time dependant satellite motion during image acquisition
- Setting up the collinearity equation to relate locations of image pixels with an earth reference coordinate frame

Step 2 DEM Intersection Model

- Projection of the DEM to the coordinate frame specified in the DG model
- Interpolation of the DEM to generate a dense grid of height values appropriate for the orthorectification task
- Connection of the DEM and LoS vector by an iterative procedure in order to retrieve object point coordinates for each image pixel

Step 3 Map Projection Model

- Provision of a geodetic datum transformation database and map projection functionality
- Transformation of the object points to a map projection like global (e.g. UTM Universal Transverse Mercator projection with WGS84 datum), continental (e.g. European LAEA Lambert Azimuthal Equal Area with ETRS89 datum) or National systems (e.g. country reference system GK Gauss-Krüger with Potsdam datum)

Step 4 Resampling Model

- Provision of different resampling techniques (Nearest Neighbor, Bi-linear, Cubic Convolution, B-Spline, Truncated Window) appropriate for further processing

From the DG model Rational Polynomial Coefficients (RPC) can be derived. The RPC encode implicitly the exterior and interior sensor orientation, which is applied to images in form of RPF using third order polynomials for nominator and denominator (80 coefficients). This Universal Sensor Model (USM) provides a standard format for the transformation of object-space coordinates to image-space coordinates. Both models - DG and RPF - can be refined using the information from GCP. A Geolayer provides for each pixel of the geometric uncorrected image geo-spatial information (e.g. longitude / latitude geographic coordinates) and includes geometric correction caused by the terrain. This layer offers the possibility to simply apply different map projections and resampling techniques. The Implicit Geocoding layer provides for each pixel of the geometric uncorrected image geo-spatial information in

form of map projection values and is used for a fast extraction of Geo-Information from the pixel location of an input image. This layer is a specialized form of the Geolayer. Only the resampling step separates implicit geocoded images from orthorectified images (explicit geocoded images). In case the keystone effect has to be taken into account, for each channel an individual RPC has to be produced.

The DG technique used for EnMAP is separated into two procedures depending on the feasibility to automatically extract GCP from reference images in order to improve the geometric accuracy. The procedures are¹

- DG without refinement of the model – referred to as **standard geometric processing**
- DG with improved model parameters using automatically determined GCP from reference images – referred to as **auxiliary geometric processing**

4.4 The EnMAP Mission and Instrument Characteristics

The major objectives of the EnMAP mission (RD-10) are to measure and analyze quantitative parameters describing environmental key processes of land and water surfaces. Derived geochemical, biochemical and biophysical parameters serve as input for physically based ecosystem models and ultimately provide information reflecting the status and evolution of various terrestrial ecosystems. Applications comprise agriculture, coastal zones, land degradation, geology and forest themes. The mission and instrument characteristics are shown in Figure 4-2.

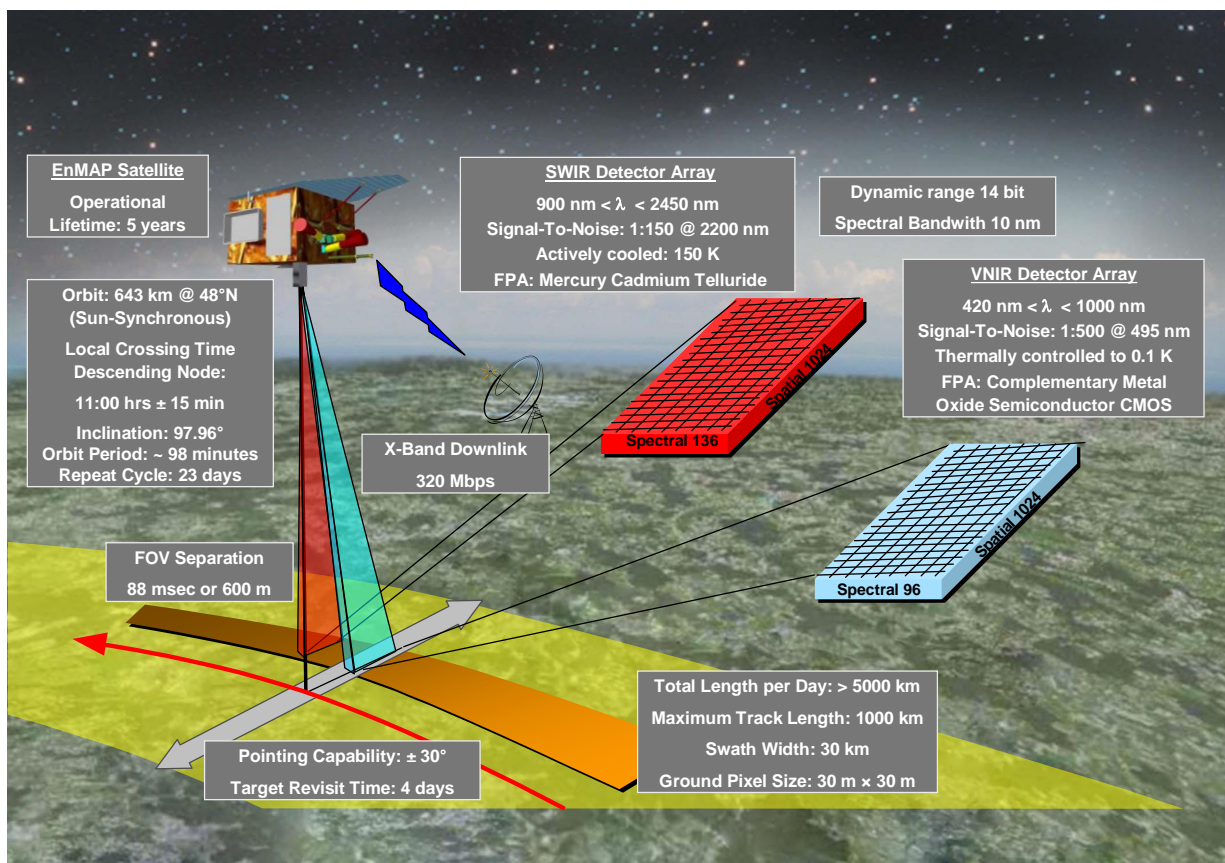


Figure 4-2 EnMAP mission and instrument characteristics

To measure frequently quantitative parameters which describe key processes on the earth's surface, the EnMAP satellite is able to revisit any location on the earth globe under a quasi-nadir observation (max. across track off-nadir pointing angle +/- 5°) each 21 days under defined illumination conditions

¹ Don't worry about names like „standard“ or „auxiliary“ geometric processing, because these are based on historical reasons. Using a global reference image database most of the EnMAP scenes will be processed using the so called „auxiliary“ geometric processing technique.

(sun-synchronous orbit at 653 km altitude with an 11:00 o'clock LTDN crossing). Utilizing the off-nadir across pointing capability of $\pm 30^\circ$ the target revisit time is within 4 days. Besides the AOCS payload consisting of three star sensors, gyros and GPS the satellite bus contains two imaging spectrometers (VNIR: Visual and Near InfraRed and SWIR: Short Wave InfraRed) operated in pushbroom configuration. The VNIR and SWIR instruments share the same telescope. During the five years of mission operations in the years from 2013-2018 data are acquired with a spatial ground sampling of approximately $30\text{ m} \times 30\text{ m}$ at nadir and a swath width of 30 km. The Hyper-Spectral Imager(HSI) is designed and realized by OHB System AG as a 2-dimensional CMOS (Complementary Metal Oxide Semiconductor) focal plane array for the VNIR spectral region and a 2-dimensional MCT (Mercury Cadmium Telluride) detector array for the SWIR channels (actively cooled down to 150 K and thermally controlled to 0.1 K). A spectral resolution of at least 10 nm is achieved over the broad spectral range from 420 nm up to 2450 nm with a VNIR (96 spectral channels) and a SWIR (136 spectral channels) detector. The overlapping range from 900 nm to 1000 nm will enable the processing chain to improve the atmospheric correction by resolving the water absorption band around 950 nm with sufficient signal to noise performance which is, e.g. 500 at 495 nm and 150 at 2200 nm. The data acquisition of the two spectrometers is realized with the method of in-field separation utilizing two entrance slits. This leads to a time separation of 88 msec between the VNIR and SWIR channels and means that the SWIR instrument scans the same area on ground about 20 lines delayed with respect to the VNIR instrument (a small latitude dependent offset of max.1.5 pixel@equator will be noticed in across direction due to the earth rotation). Therefore an increased effort in geometric processing is necessary in order to be better than the required co-registration accuracy of 0.2 pixel size.

The (spatial) smile effect is the change of the dispersion angle with the field position and the keystone effect is the change of magnification with the spectral wavelength. Therefore the slit image on the Focal Plane Array (FPA) changes with different wavelengths. Based on the advanced spectrometer design keystone and smile effects can be neglected, but are recognized in the algorithms.

4.5 The EnMAP Processing Chain and the generated Products

The automatic EnMAP HSI processing chain is illustrated in Figure 4-3 and in detail described in AD-19. The EnMAP geometric correction processor L1C uses as input the result of the L1B processor (systematic and radiometric corrected images from the VNIR and SWIR instrument plus metadata containing the orbit and attitude product as well as geometric calibration tables) as described in AD-15. The L1C processor orthorectifies image tiles from the VNIR and SWIR instrument independently. After orthorectification the two image tiles are co-registered (requirement better than 0.2 pixel size) and form a geometric consistent product over the whole wavelength range (RD-27).

The EnMAP products [AD-07] are derived from tiled data takes of size 1000×1024 pixels ($\sim 30 \times 30\text{ km}^2$), which are generated by the processing system on demand and delivered to the user community. Different product definitions (e.g. Committee on Earth Observation Satellites CEOS, European Space Agency ESA or from the different satellite data providers) are in common use, but a coherent assignment of the EnMAP product types to these definitions is not possible. Therefore the EnMAP standard product definitions are specified as follows

At-Sensor-Radiance Product (L1B)

The Level 1B product is radiometrically calibrated, spectrally characterized, geometrically characterized, quality controlled and annotated with preliminary pixel classification (usability mask). The auxiliary information (e.g. position and pointing values, interior orientation parameters, gain and offset, RPC) necessary for further processing is attached, but not applied.

Orthorectified Product (L1C)

The Level 1C product is derived from the L1B product and geometrically corrected (correction of sensor, satellite motion and terrain related distortions) and re-sampled to a specified grid (orthorectified). Auxiliary data for further processing are attached, but not applied.

Orthorectified and Atmospheric Corrected Product (L2A)

The Level 2A product is derived from the Level 1C product, atmospherically corrected and the data converted to ground surface reflectance values.

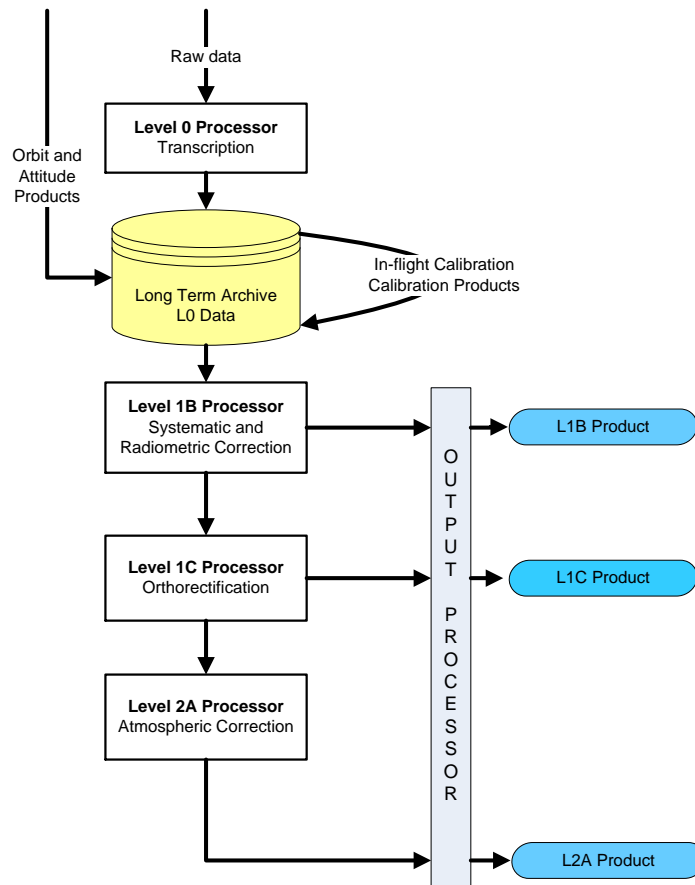


Figure 4-3 EnMAP HSI Processing Chain

4.6 How Image Tiles are processed

An EnMAP data take consists of 1000 pixel in width which corresponds to approximately 30 km swath width and $n \times 1024$ pixel in height, where $n \geq 1$. A data take is tiled into n scenes of size 1000 x 1024 pixels which correspond to approximately 30 x 30 km². Such a scene defines a delivery product.

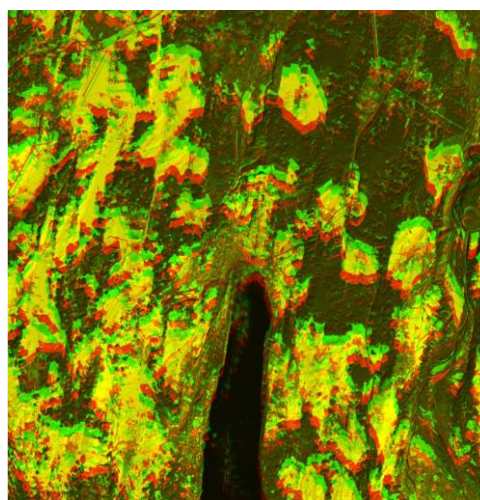


Figure 4-4 Simulation of time synchronized overlay of the VNIR and SWIR part of a L1B product (descending orbit). Green: VNIR tile; Red: SWIR tile. The usable overlap area is about 1004 lines x 998 columns depending on the latitude (loss of about 2% of data)

Due to the time separation of about $\Delta t = 88m \text{ sec}$ between data collection of the VNIR and SWIR instrument the ground coverage collected by the VNIR instrument is shifted in flight direction of about

20 pixels w.r.t. the VNIR collected data according to about 600 m on ground (the maximum across shift of about 1.5 pixel is reached at latitude 0° due to earth rotation). The L1B product which serves as input for the L1C processor consists of the time synchronized VNIR and SWIR image tile. An overlay of the VNIR and SWIR image tile of the L1B product is shown in Figure 4-4.

Consider a data take of 3 tiles as shown in Figure 4-5. The data acquisition for the VNIR instrument starts at time t_0 and for the SWIR instrument at time $t_0 + \Delta t$ which leads to a shift in flight direction x of about 600 m. For orthorectification the previous tile (if existing) of the SWIR part (slave) are merged with current selected tile to cover the corresponding VNIR part (master). Assume $h=20$ image lines due to the time separation. An additional oversize of $h_{oversize}=10$ image lines is assumed for the VNIR and SWIR part which is necessary to avoid boundary effects if contiguous orthorectified scenes are mosaicked. The procedure of tile processing is

1. append to current SWIR tile ($h+h_{oversize}$) lines of previous tile (if existing)
2. crop ($h-h_{oversize}$) lines at end of current SWIR tile
3. append $h_{oversize}$ lines of previous and next tile (if existing) to current VNIR tile
4. orthorectify VNIR and SWIR tiles
5. perform VNIR \wedge SWIR operation

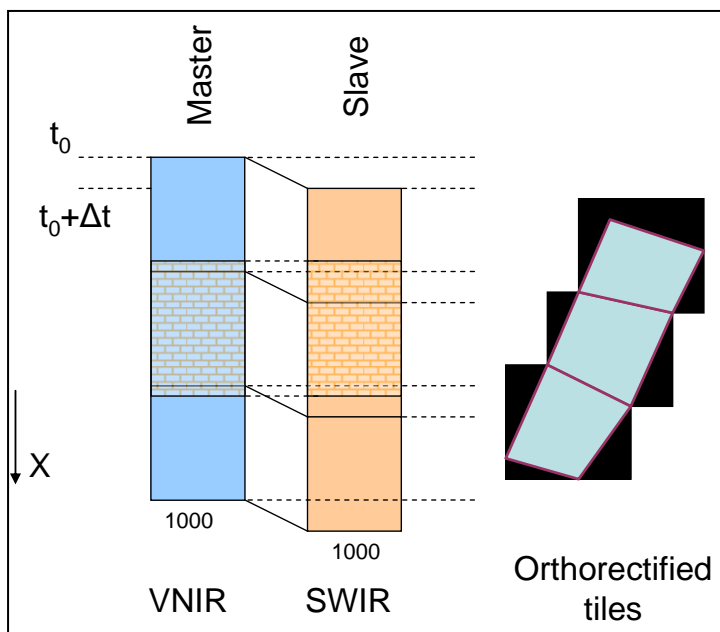


Figure 4-5 Tile processing by orthorectification. The example shows a data take with 3 image tiles. The second tile is the current one which is processed. The right part shows a seamless mosaic of the three orthorectified tiles.

5. Algorithm Description of Direct Georeferencing

This chapter starts with a generic description of the DG model followed by the specific description of the DG model used for the EnMAP HSI. The further chapters describe the HSI sensor model starting from the pixel position in the focal plane to earth location of the object point seen by the pixel.

5.1 Direct Georeferencing (generic)

The basis for all Direct Georeferencing (DG) formulas is the collinearity concept, where the coordinates of an object point \mathbf{r}^m expressed in any earth bound mapping coordinate frame (index m used for a unique mapping coordinate frame) are related to image coordinates \mathbf{r}^{sensor} derived from the measured pixel position in the sensor's coordinate frame. The concept of DG is shown in Figure 5-1

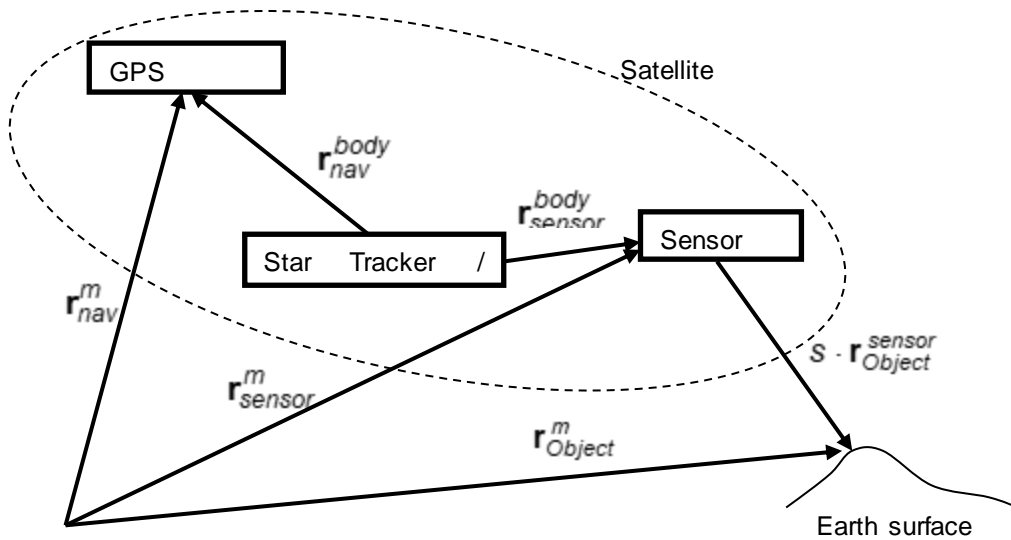


Figure 5-1 Concept of Direct Georeferencing

The rigorous relationship between 2D image coordinates (plus focal length) and 3D object coordinates is given by

$$\mathbf{r}_{object}^m = \mathbf{r}_{sensor}^m + s \cdot \mathbf{R}_{body}^m \cdot \mathbf{R}_{sensor}^{body} \cdot \mathbf{r}_{object}^{sensor} \mathbf{1} \quad 5.1-1$$

where $\mathbf{r}_{object}^{sensor}$ is the pixel view vector described in the sensor coordinate frame that is calibrated by laboratory and/or in-flight calibration procedures (mapping of image pixel location on the focal plane to pixel view vector by the formula $N \rightarrow R^3 : i \rightarrow \mathbf{r}^{sensor} = (x_i^s, y_i^s, -f)^T$ with i the pixel index number and f the focal length of the optical system). The transformation $\mathbf{R}_{sensor}^{body}$ denotes the rotation around the angles $\boldsymbol{\varepsilon} = (\varepsilon_1, \varepsilon_2, \varepsilon_3)$ from the sensor to the body coordinate frame (boresight alignment angles or instrument mounting angles), which is pre-launch characterized and refined (and modeled) by in-flight calibration due to gravity release and thermal effects. The transformation \mathbf{R}_{body}^m denotes the rotation around the angles $\boldsymbol{\psi} = (\omega, \phi, \kappa)$ from the body to a mapping coordinate frame, which is derived from the angular measurements by the on-board attitude system. The expression $\mathbf{r}_{Los}^m = \mathbf{R}_{body}^m \cdot \mathbf{R}_{sensor}^{body} \cdot \mathbf{r}_{object}^{sensor}$ denotes the (pixel) Line-of-Sight vector. The position of the sensor projection centre

¹ The lower indices of vectors (bold lower case letters, for example: $\mathbf{r}, \mathbf{a}, \dots$) indicate the position of the points, whereas the upper indices denote the coordinate frame the vector is measured. Missing lower indices denote an arbitrary vector. The notation of the indices of transformation matrices (bold capital letter, for example: $\mathbf{R}, \mathbf{T}, \dots$) indicates the transformation direction where the lower index represents the source system and the upper index the destination system. Missing indices denote an arbitrary transformation matrix.

$$\mathbf{r}_{sensor}^m = \mathbf{r}_{nav}^m - \mathbf{R}_{body}^m \mathbf{r}_{nav}^{body} + \mathbf{R}_{body}^m \mathbf{r}_{sensor}^{body} \quad 5.1-2$$

is calculated from the measured position \mathbf{r}_{nav}^m and reduced by pre-mission calibrated lever arm values \mathbf{r}_{nav}^{body} (vector from the body frame origin to the position measurement device) and $\mathbf{r}_{sensor}^{body}$ (vector from the body frame origin to the sensor projection centre), both expressed in the body coordinate frame. For single imagery the scale factor s is determined by the intersection of the pixel view vector with the earth surface given by a Digital Elevation Model DEM (RD-04, RD-06, RD-29)

Additionally to the pure geometric description by the DG formula also physical effects influence the mapping from the pixel location to real world coordinates, which are

- Atmospheric refraction
- Light aberration due to constant speed of light

Because the DG formula extensively uses coordinate transformations a short summary of orthogonal transformations and realizations of Cartesian coordinate frames is given in Appendix A: Orthogonal Transformations (Basics).

Using information from GCP a refinement of DG model parameters by iterative least squares adjustment can be achieved in order to improve the geometric accuracy of the EnMAP orthoimages..

5.2 EnMAP Satellite Coordinate Frames and Alignment Cubes

The EnMAP satellite owns different Cartesian coordinate frames shown in Figure 5-2. Most of them are defined by an alignment cube used to measure the relative orientation of the satellite and payload components.

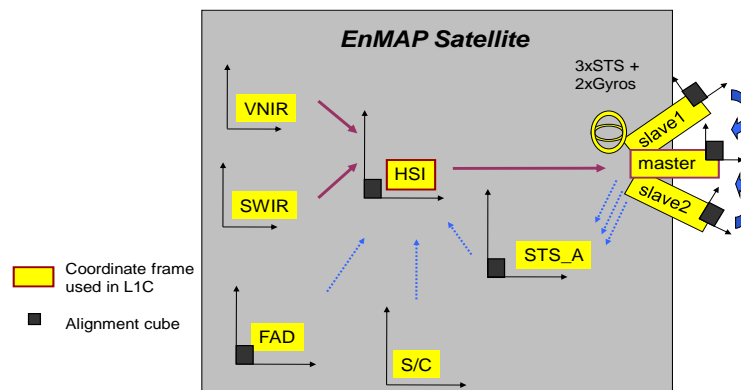


Figure 5-2 Scheme of coordinate frames and alignment cubes of the EnMAP satellite. The blue dashed arrows show the alignment measurements on ground between the coordinate frames using the installed alignment cubes. The red arrows show the coordinate frame transformations finally used in the geometric correction processor L1C.

On ground the three Star Tracker Sensors (STS) are calibrated (aligned) to the Star Tracker Sensor Assembly (STS_A). The STS_A coordinate frame is calibrated (aligned) to the cube coordinate frame of the HSI and is only used to define the satellite “Begin-of-Life” alignment. The STS_A and the HSI alignment cube are rigidly mounted on the Instrument Optic Unit (IOU) structure. The Spacecraft (S/C) coordinate frame is approximately parallel to the HSI coordinate frame and serves as guidance coordinate frame. The pixel LoS of the VNIR and the SWIR instrument is calibrated by laboratory measurements. The Full Aperture Diffuser (FAD) is calibrated to the HSI cube, which is needed for in-flight solar calibration measurements.

In orbit (early phase) the two slave STS are calibrated to the master STS, which defines further on the body coordinate frame. Using GCP information the alignment angles between the master STS and the HSI coordinate frame are determined and re-calibrated as well as modeled on a regular basis.

5.3 Direct Georeferencing (EnMAP HSI)

For the EnMAP HSI the relation between an object point $\mathbf{r}_{object}^{ECR}$ given in real world coordinates and the object point $\mathbf{r}_{object}^{HSI}$ measured by the pixel location and coordinated in the sensor coordinate frame at the acquisition time t is given by

$$\mathbf{r}_{object}^{ECR}(t) = \mathbf{r}_{HSI}^{ECR}(t) + s \cdot \mathbf{R}_{STS}^{ECR}(t) \cdot \mathbf{R}_{HSI}^{STS} \cdot \mathbf{r}_{object}^{HSI} \quad 5.3-1$$

The relation between generic and EnMAP specific mnemonics of coordinate frames is given in Table 5-1 and the elements of the collinearity equation are described in Table 5-2.

Table 5-1 Mnemonic synonym of coordinate frame terms

Generic term	EnMAP specific term	
body	STS	Body or StarTracker coordinate frame (master STS)
sensor	HSI	Sensor or HSI coordinate frame of the hyperspectral instruments

Table 5-2 Description of the collinearity equation components

$\mathbf{r}_{object}^{ECR}$	Vector to an object point located on the earth surface and sensed by the corresponding instrument pixel. This vector is coordinated in the Cartesian coordinate frame ECR.
$\mathbf{r}_{object}^{HSI}$	Vector from the sensor projection centre towards the object point on earth passing the corresponding focal plane element of the instrument. The mapping from the pixel location (pixel index number) to Cartesian coordinates of the sensor frame is derived from laboratory and/or in-flight calibration tables.
\mathbf{r}_{HSI}^{ECR}	Position of the sensor at time t , when a scan line is collected by the on-board GPS system with 1 Hz. This vector is coordinated in the Cartesian coordinate frame ECR.
\mathbf{R}_{HSI}^{STS}	Rotation matrix to transform the vector $\mathbf{r}_{object}^{HSI}$ to the STS coordinate frame. This transformation describes the mounting angles between the sensor and the body or master StarTracker STS coordinate frame and depends on temperature influences caused by sun exposure during satellite orbit revolution.
\mathbf{R}_{STS}^{ECR}	Rotation matrix to transform the vector $\mathbf{R}_{HSI}^{STS} \cdot \mathbf{r}_{object}^{HSI}$ to the earth centered rotated ECR coordinate frame. This transformation is based on on-board Startracker/Gyro measurements, which are post-processed by the EnMAP Ground Segment.
s	Scale factor, which is determined by the intersection of the vector $\mathbf{R}_{STS}^{ECR} \cdot \mathbf{R}_{HSI}^{STS} \cdot \mathbf{r}_{object}^{HSI}$ with the earth surface, given by a Digital Elevation Model (DEM).

The following adjustments are applied to the generic DG model for the EnMAP DG model.

Lever arms

The distance between the Startracker (STS) and the sensor projection center as well as the distance between STS and GPS antenna is small (<1 m) w.r.t. the pixel size of 30 m.

$$\mathbf{r}_{nav}^{body} \approx \mathbf{0} \text{ and } \mathbf{r}_{sensor}^{body} \approx \mathbf{0} \Rightarrow \mathbf{r}_{sensor}^m = \mathbf{r}_{nav}^m$$

5.4 Line-Of-Sight Vector

The establishment of the Line-of-Sight (LoS) vector of Earth Observation Sensors requires a careful characterization of the image/pixel generation process: from the focal plane location of the instrument pixel to an Earth surface location in terms of earth bound coordinate frames. The following chapters describe step by step the transformations from the pixel index number of the HSI to the time dependent pixel Line-of-Sight (LoS) vector within the earth bound coordinate frame ECR.

5.4.1 Interior Orientation

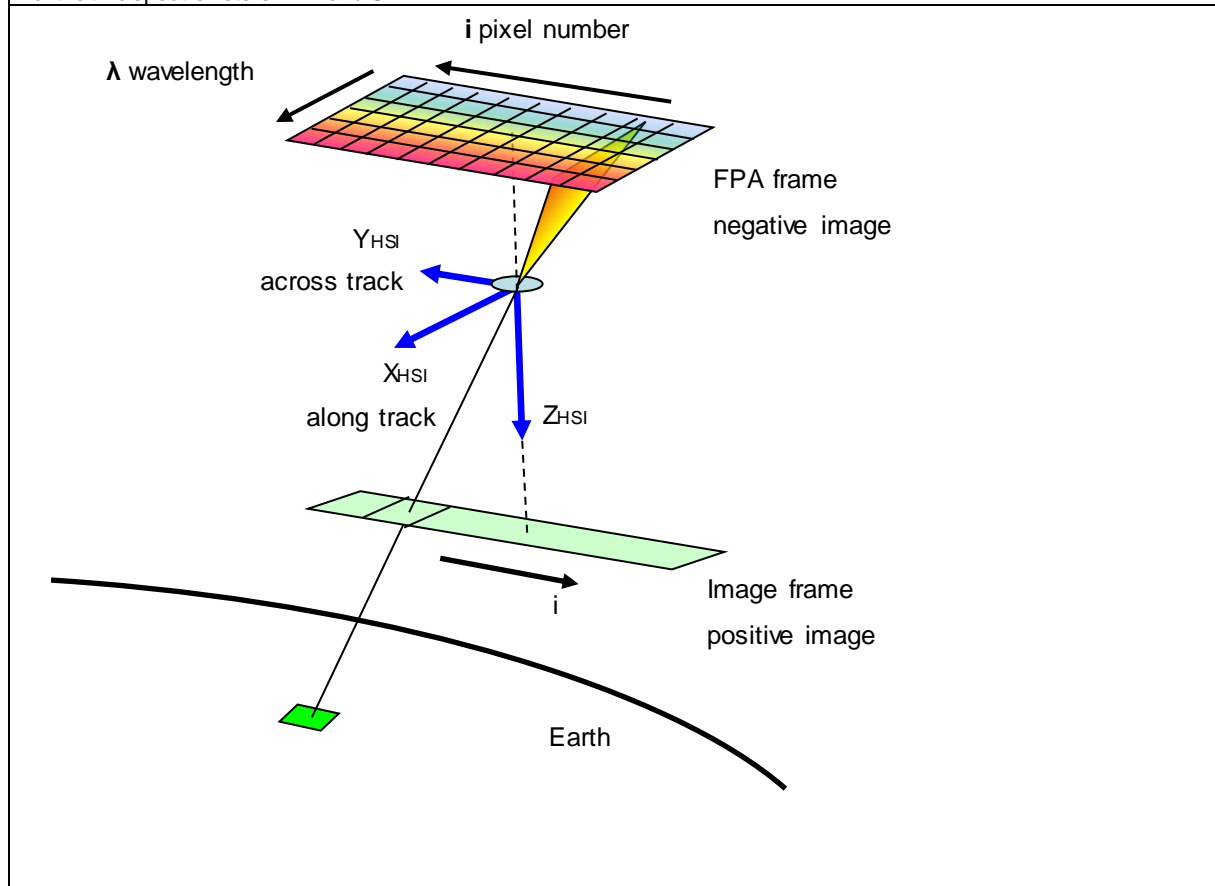
The Hyper Spectral Instrument (HSI) is designed as a 2-dimensional CMOS (Complementary Metal Oxide Semiconductor) focal plane array for the VNIR spectral region and a 2-dimensional MCT (Mercury Cadmium Telluride) detector array for the SWIR channels. In order to address the pixels of the FPA for each of the instruments by integer numbers the index i is used.

The index i address a pixel in a scan line in the positive image of the camera in such a way that for a descending orbit the counting starts with the western part of the scan line (for the negative image of the camera the pixel counting is reverse). At a time t the instrument collects pixels of one image line in all wavelengths. A collection of image lines forms an image scene.

A pixel i in an image line is mapped to the Cartesian sensor coordinate frame of the HSI defined as follows (see Table 5-3)

Table 5-3 Definition of Sensor Coordinate Frame

TYPE	Title / Name	Mnemonic
Instrument fixed	Sensor Coordinate Frame	sensor or HSI
Definition <ul style="list-style-type: none"> Z_{HSI} is the instrument LoS and defines the optical axis for the SWIR and the VNIR instrument (roughly spoken the nadir direction) Y_{HSI} is parallel to the entrance slits (roughly spoken the across track or scan direction) X_{HSI} completes the right handed triad (roughly spoken the along track or flight direction) Origin: Centre of the double slit for VNIR and SWIR 		
Rationale The sensor coordinate frame is realized as a Cartesian frame and describes the view direction of pixels in an image line (VNIR & SWIR). The keystone effect is taken into account.		
Comment The HSI consists of one telescope and two spectrometers for VNIR and SWIR spectral range. The data acquisition of the two spectrometers is realized with the method of in-field separation utilizing two entrance slits. The HSI coordinate frame is valid for the two spectrometers VNIR and SWIR.		



The internal geometry of the EnMAP HSI is extensively characterized in the laboratory by highly accurate measurements of the direction angles of single illuminated pixels (gravity center of the pixel) to the (adjusted) collimator axis. For each pixel two angles on object side completely describe the internal camera geometry. This also includes (possible) geometric keystone effects.

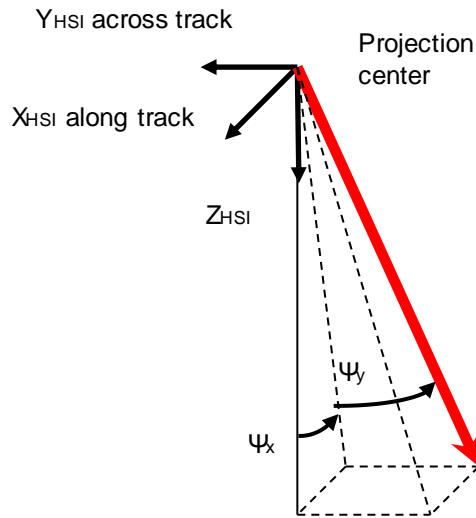


Figure 5-3 **Definition of object sided pixel view direction angles**

The pixel view direction of an HSI pixel (SWIR and VNIR channels respectively) is given by the two object sided angles ψ_x and ψ_y , as illustrated in Figure 5-3. The angles are in decimal degree.

$$\mathbf{r}_{object}^{sensor} \equiv \mathbf{r}_{object}^{HSI} = \frac{1}{\sqrt{\tan(\psi_x)^2 + \tan(\psi_y)^2 + 1}} \begin{pmatrix} \tan(\psi_x) \\ \tan(\psi_y) \\ 1 \end{pmatrix} \quad 5.4.1-1$$

The two angles for the pixel i are described by a 2nd order polynomial. The initial polynomial coefficients are derived from pre-launch geometric calibration (about 20 support points) with an accuracy of better than 1.0 arcsec. The keystone is described by wavelength depended coefficients accounting for possible keystone effects.

$$\begin{aligned} \psi_x &= \psi_x(i, \lambda) = a_x(\lambda) + b_x(\lambda) \cdot di + c_x(\lambda) \cdot di^2 \\ \psi_y &= \psi_y(i, \lambda) = a_y(\lambda) + b_y(\lambda) \cdot di + c_y(\lambda) \cdot di^2 \end{aligned} \quad 5.4.1-2$$

where

$di = i - i_0$ pixel column number with $i = 13, \dots, 1013$ (illuminated pixels in one image line) and $i_0 = 527.5$ for VNIR and $i_0 = 511.5$ for SWIR (from OHB laboratory calibration, AD-21)

$\psi_x(i, \lambda)$ along track look angle, which depends on the wavelength λ if keystone effect recognized

$\psi_y(i, \lambda)$ across track look angle, which depends on the wavelength λ if keystone effect recognized

$g_x(d\lambda)$ polynomial $g_x(\lambda) = g_{1,x} + g_{2,x} \cdot d\lambda + g_{3,x} \cdot d\lambda^2$ and $g_x(d\lambda) \in \{a_x(d\lambda), b_x(d\lambda), c_x(d\lambda)\}$

$g_y(d\lambda)$ polynomial $g_y(\lambda) = g_{1,y} + g_{2,y} \cdot d\lambda + g_{3,y} \cdot d\lambda^2$ and $g_y(d\lambda) \in \{a_y(d\lambda), b_y(d\lambda), c_y(d\lambda)\}$

Where $d\lambda = \lambda - \lambda_0$ and $\lambda_0 = 659 \text{ nm}$ for VNIR and $\lambda_0 = 1675 \text{ nm}$ for SWIR (from OHB laboratory calibration, AD-21). The central wavelength λ is tabulated w.r.t. the channel number in the metadata (central wavelength values are determined at pixel index $i = 500$). The calibration coefficients are listed in Table 5-4.

Table 5-4 **Initial (pre-launch) polynomial coefficients to calculate the look direction angles for pixels of the VNIR and SWIR instrument. Values from OHB laboratory calibration, AD-21.**

	$a_{1,x}(\lambda)$	$a_{2,x}(\lambda)$	$a_{3,x}(\lambda)$	$b_{1,x}(\lambda)$	$b_{2,x}(\lambda)$	$b_{3,x}(\lambda)$	$c_{1,x}(\lambda)$	$c_{2,x}(\lambda)$	$c_{3,x}(\lambda)$
name	A_1_X	A_2_X	A_3_X	B_1_X	B_2_X	B_3_X	C_1_X	C_2_X	C_3_X
VNIR	- 0.032028 74987677 443	0.0	0.0	- 4.521812 10868148 7e-06	0.0	0.0	- 1.151444 02143658 2e-08	0.0	0.0



EnMAP Ground Segment
 Level 1C Processor (Geometric Correction) ATBD
 Restriction: Public

Doc. ID EN-PCV-TN-5006
 Issue 1.7
 Date 07.10.2024
 Page 27 of 73

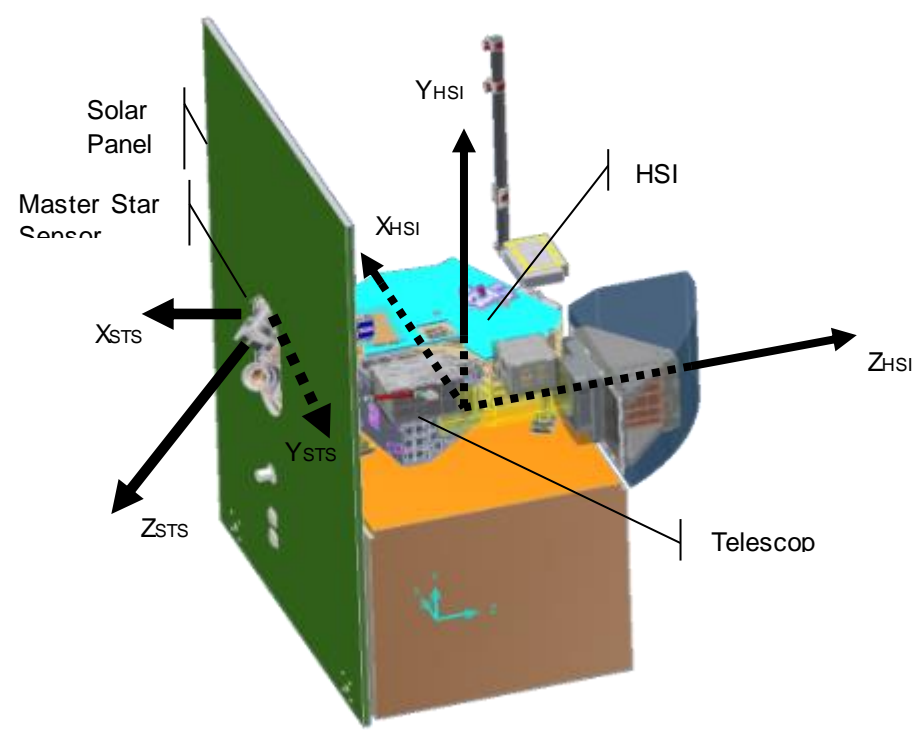
SWIR A	0.021540 52397971 6425	0.0	0.0	- 4.521812 10868148 7e-06	0.0	0.0	- 1.151444 02143658 2e-08	0.0	0.0
SWIR B	0.021540 52397971 6446	0.0	0.0	- 4.521812 10867645 6e-06	0.0	0.0	- 1.151444 02143658 2e-08	0.0	0.0

	$a_{1,y}(\lambda)$	$a_{2,y}(\lambda)$	$a_{3,y}(\lambda)$	$b_{1,y}(\lambda)$	$b_{2,y}(\lambda)$	$b_{3,y}(\lambda)$	$c_{1,y}(\lambda)$	$c_{2,y}(\lambda)$	$c_{3,y}(\lambda)$
name	A_1_Y	A_2_Y	A_3_Y	B_1_Y	B_2_Y	B_3_Y	C_1_Y	C_2_Y	C_3_Y
VNIR	0.000480 23005003 884855	0.0	0.0	0.002630 89307552 63725	0.0	0.0	0.0	0.0	0.0
SWIR_A	- 0.004325 87289955 9228	- 377.7042 81765347 96	0.0	0.002630 99230657 83135	0.070240 01860878 16	0.0	0.0	0.0	0.0
SWIR_B	- 0.004243 10256007 0171	- 377.7987 20191993 4	0.0	- 0.002631 25546942 44133	- 0.070203 44079992 458	0.0	0.0	0.0	0.0

5.4.2 Instrument Mounting Angles (Boresight Alignment Angles)

The boresight alignment angles describe the relation between the coordinate frames of the payload instruments – namely the body (STS) and the sensor (HSI) coordinate frame. The master STS coordinate frame serves as intermediate coordinate frame to connect the sensor and STS coordinate frames and is described as follows (Table 5-5). During Commissioning Phase, STS 1 was selected as the master STS.

Table 5-5 Definition of Body Coordinate Frame

TYPE	Title / Name	Mnemonic
Instrument fixed	Spacecraft coordinate frame	Body or STS
Definition <ul style="list-style-type: none"> • Z_{STS} Line-of-Sight of the master STS coordinate frame • Y_{STS} Arbitrary direction defined by the STS alignment cube • X_{STS} completes the right handed triad • Origin: Centre of the alignment cube of the master STS coordinate frame 		
Rationale The STS coordinate frame is used to describe the attitude measurements by the STS and Gyro units (Kalman filtered solution).		
Formula $\mathbf{R}_{sensor}^{body} \equiv \mathbf{R}_{HSI}^{STS}$ $\mathbf{r}^{STS} = \mathbf{R}_{HSI}^{STS} \cdot \mathbf{r}^{HSI} \quad \text{and} \quad \mathbf{r}^{HSI} = \mathbf{R}_{STS}^{HSI} \cdot \mathbf{r}^{STS}$		
Comments The attitude measurements by the combined STS and Gyro units are initially given w.r.t. the ECI coordinate frame. On-ground processing by the Flight Dynamics Sub-System of the Mission Operating System transforms the attitude from the ECI to the ECR coordinate frame, which serves as input for the geometric processor. The ECI to ECR transformation is also described in the appendix "Quasi Inertial Coordinate Frame (ECI Earth Centered Inertial)" NOTE: The STS is directly mounted on the HSI base plate in order to reduce thermal influences on the boresight alignment angles.		
Diagram 		

The HSI instrument mounting angles with respect to body coordinate frame are determined in a first step by pre-launch laboratory calibration. Due to gravity release effects these values are refined in a second step by in-flight calibration during the commissioning phase. In order to account for rotational variations of the instrument mounting angles during satellite orbit cycles – which are mainly affected by

thermal influences due to the sun exposure time of the satellite – an additional rotational matrix in small angle approximation is introduced.

$$\mathbf{R}_{sensor}^{body} \equiv \mathbf{R}_{HSI}^{STS} = \begin{pmatrix} 1 & \kappa_{var} & -\phi_{var} \\ -\kappa_{var} & 1 & \omega_{var} \\ \phi_{var} & -\omega_{var} & 1 \end{pmatrix} \cdot \mathbf{R}_z(\kappa_{init}) \cdot \mathbf{R}_y(\phi_{init}) \cdot \mathbf{R}_x(\omega_{init}) \quad 5.4.2-1$$

with $\kappa_{init}, \phi_{init}, \omega_{init}$ are the initial (begin-of-life) Euler angles and $\kappa_{var}, \phi_{var}, \omega_{var}$ are the thermal influenced Euler angles to rotate the HSI coordinate frame into the STS coordinate frame around the x, y, z axes, respectively. The initial instrument mounting angles are part of the product metadata and given in Table 5-6.

Table 5-6 Initial mounting angles valid for the VNIR and SWIR instrument (after first update during commissioning phase)

Parameter	ω_{init} [°]	ϕ_{init} [°]	κ_{init} [°]
name	OMEGA_INIT	PHI_INIT	KAPPA_INIT
VNIR & SWIR	144.802912665	-29.9977482452	-12.8673432247

The variation of the instrument mounting angles is described by polynomial functions. The coefficients $n_{x0...10}, n_{y0...10}$ and $n_{z0...10}$ are set to zero initially and modeled if a noticeable variation is detected. The polynomial coefficients are described in Table 5-7.

$$\begin{aligned} \omega_{var} &= n_{x0} + n_{x1} \cdot s^1 + n_{x2} \cdot s^2 + \dots + n_{x10} \cdot s^{10} \\ \phi_{var} &= n_{y0} + n_{y1} \cdot s^1 + n_{y2} \cdot s^2 + \dots + n_{y10} \cdot s^{10} \\ \kappa_{var} &= n_{z0} + n_{z1} \cdot s^1 + n_{z2} \cdot s^2 + \dots + n_{z10} \cdot s^{10} \end{aligned} \quad 5.4.2-2$$

with the normalized time period $s = t_{acc}/T$ (t_{acc} : accumulated time the satellite is exposed to the sun before a scene is acquired; T : orbit period of 98.7 minutes) the satellite is exposed to the sun before image acquisition.

From the satellite position (latitude ϕ and longitude λ) and the number of days d of the year the sun exposure time t_{acc} is calculated using the equation for the sun zenith angle θ_{zenith} given by

$$\cos \theta_{zenith} = \cos \phi \cdot \cos \delta \cdot \cos \omega + \sin \phi \cdot \sin \delta \quad 5.4.2-3$$

with the time dependence of the Earth declination δ

$$\sin \delta = \sin(23.44^\circ) \cdot \sin\left(\frac{2\pi \cdot (d-81)}{365}\right) \quad 5.4.2-4$$

and the Greenwich hour angle ω at UTC time t'

$$\omega = \frac{360^\circ}{24} \cdot (t' - 12) + \frac{24}{360^\circ} \lambda + \frac{-7.65 \cdot \sin\left(2\pi \frac{d-3}{365}\right) + 9.86 \cdot \sin\left(4\pi \frac{d-81}{365}\right)}{60} \quad 5.4.2-5$$

The satellite is exposed to the sun light as long as the angle θ_{zenith} is smaller than 103° , which accounts for the orbit height of about 653 km.

Table 5-7 Name of coefficients used in the product metadata file

Parameter	$n_{x0...10}$	$n_{y0...10}$	$n_{z0...10}$
name	N_X_i with $i=0, \dots, 10$	N_Y_i with $i=0, \dots, 10$	N_Z_i with $i=0, \dots, 10$
Updated during mission (initially set to zero) Current values can be found in the metadata file of the scene			

5.4.3 Atmospheric Refraction Correction

An atmospheric refraction correction is performed on the view direction vectors of each pixel. Let $\mathbf{r}_{object}^{body} = (x, y, z)^T = \mathbf{R}_{Sensor}^{body} \cdot \mathbf{r}_{object}^{sensor}$ the look direction vector expressed in the body coordinate frame then the atmospheric corrected view direction is

$$\begin{pmatrix} x' \\ y' \\ z' \end{pmatrix}_{object}^{body} = \frac{1}{\sqrt{\delta \cdot x^2 + \delta \cdot y^2 + z^2}} \begin{pmatrix} \delta \cdot x^2 \\ \delta \cdot y^2 \\ z^2 \end{pmatrix} \quad 5.4.3-1$$

with $\delta = \frac{\tan(\theta - \Delta\theta)}{\tan(\theta)}$
 $\theta = \arctan\left(\frac{x^2 + y^2}{z}\right); \quad \Delta\theta = 2.316 \cdot \tan(\theta) \cdot \left(\frac{P_1 - P_2}{H} - 43.11 \cdot \frac{P_2}{T}\right) + \delta_1 + \delta_2$

$$\delta_1 = \tan(\theta) \frac{2 + 3 \cdot \tan^2(\theta)}{5} \cdot \delta_1'; \quad \delta_2 = 0.129 \cdot \tan(\theta) \frac{e_1 - e_2}{H} + 95 \cdot \frac{e_2}{T}$$

- H nominal satellite altitude in mm (=653e+6).
- P₁ standard atmospheric pressure at ground in hPa (=1013.25).
- P₂ atmospheric pressure at the satellite altitude in hPa (=0).
- T atmospheric temperature at satellite altitude in K (=999).
- δ₁' earth curvature correction coefficient in radian (=0.812e-6).
- e₁ vapor pressure at ground in hPa (=17.06).
- e₂ vapor pressure at satellite altitude in hPa (=0)

The magnitude of the ground displacement caused by atmospheric refraction is for 10° off nadir view about 0.5 m, for 20° about 1.1 m and for 30° about 2.1 m.

Although the atmospheric refraction changes with the wavelength, for this correction the difference between the wavelengths is negligible. For more information on atmospheric refraction effects see also [RD-57].

5.4.4 Attitude

In precise satellite mode the attitude determination utilizes the measurements of three Star Sensors (3 axes information each) and two Gyros (3 axes information each). [AD-02][AD-03]

Star Sensors (STS)

Each star sensor provides 3 axes attitude information with high absolute accuracy (measurements with respect to the celestial sphere) with an update rate of 1 Hz. Nominally two star sensors are hot for the measurements, but due to blinding by sun or moon only one star sensor serves for attitude determination. The star sensor selection is part of the downlinked AOCS data.

Gyros

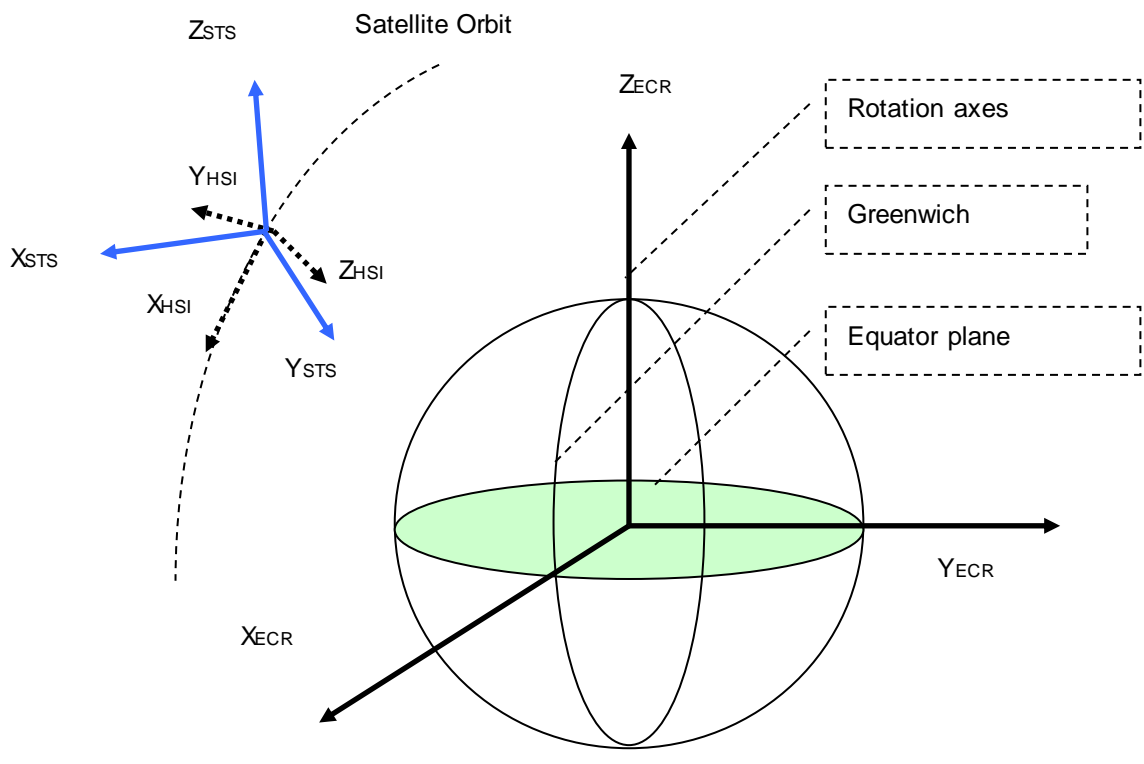
The on-board gyro unit – inertial measurement unit IMU - allows highly precise relative measurements of the attitude rate utilizing the Sagnac effect of a ring laser. The orthogonal configuration of three ring lasers allows the measurement of a 3 axes attitude rate. A continuous calibration of the gyros is necessary to account for drifts. In precise satellite mode the update rate of the gyros is 10 Hz.

Attitude Solution

The attitude measurements of the star sensors are corrected and improved by means of gyro measurements exploiting a Kalman filter. The attitude solution uses one of the star sensor measurements only and is gyro-corrected on-board. These values are updated with 1 Hz in precision satellite mode, describing the attitude with respect to the Earth Centered Inertial (ECI) frame. On ground processing transforms the attitude data to quaternions expressed in Earth Centered Rotated (ECR) frame. A pointing knowledge of 13.7 arcsec has been estimated during pre-launch characterization (half cone angle with a cumulative probability greater than 68%) according to ~43.0 m on ground for the orbit reference height of 653 km.

The attitude is measured with respect to the ECR frame, which is defined as follows (see Table 5-8)

Table 5-8 Definition of ECR Coordinate Frame

TYPE Earth fixed	Title / Name Earth Centered Rotated Earth Centered Earth Fixed	Mnemonic ECR or ECEF
Definition <ul style="list-style-type: none"> • Z_{ECR} Direction to the north pole along the mean earth rotation axes • X_{ECR} Direction through the Greenwich meridian • Y_{ECR} completes the right handed triad • Origin: Mass centre of earth including the atmosphere 		
Rationale The ECR coordinate frame is used to describe the pixel view vectors in an earth bound coordinate frame.		
Formula $\mathbf{r}^{ECR} = \mathbf{R}_{STS}^{ECR} \cdot \mathbf{r}^{STS} \quad \text{and} \quad \mathbf{r}^{STS} = \mathbf{R}_{STS}^{ECR T} \cdot \mathbf{r}^{ECR}$ $\mathbf{R}_{body}^{ECR} \equiv \mathbf{R}_{STS}^{ECR}$		
Comments The master STS will be defined after launch and will serve as body coordinate frame. Therefore the orientation of the master STS in the diagram do not reflect the actual orientation.		
Diagram 		

The quaternions $q = (q_0, \underline{q}) = (q_0, q_1, q_2, q_3)$, with q_0 the scalar (real part of the 4-tupel quaternion vector describing the rotation angle) and \underline{q} the vector (imaginary part of the 4-tupel quaternion vector describing the rotation axes) can be written as direction cosine matrix

$$\mathbf{R}_{body}^{ECR} \equiv \mathbf{R}_{STS}^{ECR} = \begin{pmatrix} c_{11} & c_{12} & c_{13} \\ c_{21} & c_{22} & c_{23} \\ c_{31} & c_{32} & c_{33} \end{pmatrix} = \begin{pmatrix} 1 - 2(q_2^2 + q_3^2) & 2(q_1q_2 - q_0q_3) & 2(q_1q_3 + q_0q_2) \\ 2(q_1q_2 + q_0q_3) & 1 - 2(q_1^2 + q_3^2) & 2(q_2q_3 - q_0q_1) \\ 2(q_1q_3 - q_0q_2) & 2(q_2q_3 + q_0q_1) & 1 - 2(q_1^2 + q_2^2) \end{pmatrix} \quad 5.4.4-1$$

From the direction cosine matrix Euler angles of a specific rotation sequence are extracted (see Appendix C: Composed Rotation Matrix and Rotation Angle Extraction). For EnMAP the sequence yaw-pitch-roll is used, which leads to the Euler angles

Euler angle	Formula
roll angle	$\omega = \arctan\left(-\frac{c_{32}}{c_{33}}\right)$
pitch angle	$\phi = \arcsin(c_{31})$
yaw angle	$\kappa = \arctan\left(-\frac{c_{21}}{c_{11}}\right)$

NOTE: S/W code has to use the *atan2* function for the arctan calculation.

The resulting rotation matrix is then given by

$$\mathbf{R}_{body}^{ECR} \equiv \mathbf{R}_{STS}^{ECR} = \mathbf{R}_z(\kappa)\mathbf{R}_y(\phi)\mathbf{R}_x(\omega) = \begin{pmatrix} \cos \kappa & \sin \kappa & 0 \\ -\sin \kappa & \cos \kappa & 0 \\ 0 & 0 & 1 \end{pmatrix} \begin{pmatrix} \cos \phi & 0 & -\sin \phi \\ 0 & 1 & 0 \\ \sin \phi & 0 & \cos \phi \end{pmatrix} \begin{pmatrix} 1 & 0 & 0 \\ 0 & \cos \omega & \sin \omega \\ 0 & -\sin \omega & \cos \omega \end{pmatrix}$$

5.4.4-2

5.4.5 Light Aberration (Speed of Light Correction)

The aberration of light for satellite observations is an effect caused by the final speed of light c ($c = 299792458 \text{ m/sec}$) and the high speed v of a satellite in orbit ($v_{along} \approx 7000 \text{ m/sec}$). This causes an angular deviation in along track of about $\delta_{along} = \sin^{-1}\left(\frac{v_{along}}{c}\right) = 23.3\mu\text{rad}$ of the viewing direction which corresponds to about 15 m on ground. In across track direction the maximum deviation is reached at earth equator, where a earth rotation speed of about $v_{across} \approx 460 \text{ m/sec}$ is assumed which leads to an angle of $\delta_{across} = \sin^{-1}\left(\frac{v_{across}}{c}\right) = 1.5\mu\text{rad}$ corresponding to about 1 m on ground. The expression for light aberration correction is in Galileo Transformation given by

$$\mathbf{r}_{LoS}^{ECR\ c_corr} = \frac{\mathbf{r}_{LoS}^{ECR} - \frac{v_{Satellite}^{ECR}}{c}}{\left| \mathbf{r}_{LoS}^{ECR} - \frac{v_{Satellite}^{ECR}}{c} \right|}$$

5.4.5-1

NOTE: Due to nearly circular orbit the deviation δ_{along} is constant and can be account as additional boresight alignment angle.

5.4.6 State Vector

The state vectors (position and velocity) of the satellite are measured with a frequency of 1 Hz. The orbit data are GPS navigation solutions from the on board single frequency MosaicGNSS GPS receiver. The state vectors are given in Cartesian coordinates referenced to the ITRF 2000 coordinate frame.

5.5 Time Synchronization and Approximation

5.5.1 Time Scale for Data Synchronization

The atomic GPS time scale serves as unique time base to synchronize the data streams. The GPS time starts at midnight 5th to 6th January 1980 and is not perturbed by leap seconds.

For the attitude and orbit product the *timeGPS* (coarse time given in seconds; UINT64) and the *timeGPSFraction* (fraction of GPS time in seconds; float64Type) is used to calculate the measurement time of the position, velocity and attitude data records. The time is given for the position / velocity data record by

$$t_{position/velocity} = timeGPS_{position/velocity} + timeGPSFraction_{position/velocity}$$

and for the attitude data record containing the quaternions by

$$t_{attitude} = timeGPS_{attitude} + timeGPSFraction_{attitude}$$

The acquisition time of a scan line of the HSI is coded as CTIME (coarse time given in seconds; UINT32) and FTIME (fine time given in μsec ; UINT32) in the VNIR and SWIR virtual channels respectively. For the VNIR instrument a time correction value to account for the image jitter is provided in the virtual channel. Leap seconds are not included. Therefore the acquisition time of a scan line is given by

$$t_{VNIR_scanline} = CTIME_{VNIR} + FTIME_{VNIR} \cdot 10^{-6} + JitterCorrectionTime$$

$$t_{SWIR_scanline} = CTIME_{SWIR} + FTIME_{SWIR} \cdot 10^{-6}$$

The JitterCorrectionTime is part of the VNIR virtual channel.

5.5.2 Position and Velocity Approximation

For each HSI scan line (separately for the VNIR and the SWIR instrument) the position and velocity data are calculated using Spline Approximation technique provided by the SciPy [RD-53] library. The on-board measurement frequency of the ephemeris data is given by 1 Hz. The ephemeris data are re-processed on ground by orbit models in order to increase the accuracy.

5.5.3 Attitude Approximation

The attitude data are given by (unit) quaternions with a frequency of 1 Hz. The quaternions are transformed to Euler angles prior to the HSI scan line synchronization. The precise AOCS mode – meaning that the gyro data are updated with a frequency of 10 Hz - is entered before each datatake and stopped after each datatake. For the maximum datatake length of 1000 km about 140 attitude measurements and for a minimum datatake length of 30 km (according to one image tile) about 4 attitude measurements are available.

Two different approximation methods were taken into consideration for the determination of the attitudes for every image line: Chebyshev Approximation and Spline Approximation.

5.5.3.1 Chebyshev Approximation

The three attitude angle measurements can be approximated by Chebyshev polynomials for the whole datatake duration – including 5 values before (t_s) and 5 values after (t_e) the datatake acquisition. The expected smooth and periodic behavior of the satellite attitude induced by the the AOCS control system can be very well reconstructed by Chebyshev polynomials¹.

The attitude Euler angles $\alpha(t) \in \{\omega(t), \phi(t), \kappa(t)\}$ can be approximated in the given time interval $t \in [t_s, t_e]$ by the Chebyshev series of degree n by

$$\alpha(\tau) \approx \sum_{k=0}^n c_k \cdot P_k(\tau) \tag{5.5.3-1}$$

The Chebyshev polynomials are defined in the range $\tau \in [-1, +1]$, which leads to a linear mapping of the time interval $[t_s, t_e]$ to $[-1, +1]$ by

$$\tau = \frac{t - \frac{1}{2}(t_e + t_s)}{\frac{1}{2}(t_e - t_s)} \tag{5.5.3-2}$$

The Chebyshev coefficients c_0, \dots, c_n are the unknowns of the approximation problem and the orthogonal Chebyshev polynomials $P_0(\tau), \dots, P_n(\tau)$ are constructed by the recurrence relation

$$\begin{aligned} P_0(\tau) &\equiv 1 \\ P_1(\tau) &= \tau \\ P_{k+1}(\tau) &= 2 \cdot \tau \cdot P_k(\tau) - P_{k-1}(\tau), \quad \text{for } k \geq 1 \end{aligned} \tag{5.5.3-3}$$

¹ Moral Principle by John P. Boyd 2001 in Chebyshev and Fourier Spectral Analysis

- 1) when in doubt, use Chebyshev polynomials
- 2) unless you are sure another set of basis functions is better, use Chebyshev polynomials
- 3) unless you are really, really sure that another set of basis functions better, use Chebyshev polynomials

Given a set of $j = 1, \dots, m$ attitude angle measurement points y_j in the time interval $[t_s, t_e]$ the Chebyshev coefficients can be determined by least squares method. Re-writing the Chebyshev series

$$\mathbf{P} \cdot \mathbf{c} \equiv \begin{pmatrix} P_0(\tau_1) & P_1(\tau_1) & \dots & P_n(\tau_1) \\ P_0(\tau_2) & P_1(\tau_2) & \dots & P_n(\tau_2) \\ \dots & \dots & \dots & \dots \\ P_0(\tau_m) & P_1(\tau_m) & \dots & P_n(\tau_m) \end{pmatrix} \begin{pmatrix} c_0 \\ c_1 \\ \dots \\ c_n \end{pmatrix} = \begin{pmatrix} y_1 \\ y_2 \\ \dots \\ y_m \end{pmatrix} \equiv \mathbf{y} \quad 5.5.3-4$$

The normal equations $(\mathbf{P}^T \mathbf{P}) \cdot \mathbf{c} = \mathbf{P}^T \mathbf{y}$ can be minimized in the sense of least squares to retrieve the Chebyshev coefficients.

The degree n of the Chebyshev polynomial is calculated using an adaptive procedure. The accuracy of the STS is – as mentioned before – about 13.7 arcsec. Starting with the lowest Chebyshev polynomial (order 0) the degree of the Chebyshev polynomial is increased step by step until the standard deviation at the sample points to the approximated curve is of this magnitude. By this procedure the actual attitude behavior of the satellite is approximated.

5.5.3.2 Spline Approximation

Unlike Chebyshev approximation, spline functions are more flexible when it comes to local curve deviations. Here, the function `LSQUnivariateSpline` provided by the SciPy [RD-53] library is used to fit a spline to the attitude measurements. A detailed comparison between Chebyshev and least squares spline approximation for the EnMAP image acquisition geometry has been performed in [RD-55]. The major outcome of this investigation was that interpolation (like Lagrange interpolation) is not recommended, whereas approximation techniques perform very well especially regarding co-registration accuracy. Therefore the baseline for attitude reconstruction is the least squares spline approximation with a fall back option to the Chebyshev approximation. Both methods will be implemented and can be switched easily in an update of the processor based on investigations during the commissioning phase.

5.6 DEM Intersection Model

Geometric distortions caused by the terrain are taken into account using a Digital Elevation Model (DEM). The usage of surface models (DSM) within the orthorectification is more accurate because the optical sensor collects the reflected light from the surface, whereas terrain models (DTM) lead to geometric distortion (e.g. urban and forest areas). Only DEM with ellipsoidal heights can be used for the geometric correction (geoid heights have to be transformed to ellipsoid height using e.g. the Earth Gravity Model EGM96).

5.6.1 Global DEM Database

A global digital elevation model (DEM) serves as input for the orthorectification process.

The DEM used in EnMAP is the global Copernicus DEM with up to 30 m horizontal resolution (COP-DEM GLO-30). Specifications of this dataset can be found in [RD-56] and [RD-58].

The geometric displacement Δs caused by the DEM error Δh depends on the off nadir view ω and the terrain slope angle α .

$$\Delta s = \frac{\Delta h \cdot \tan \omega}{1 - \tan \alpha \cdot \tan \omega} \quad 5.6.1-1$$

In Table 5-9 the displacements caused by a DEM error are shown for flat and mountainous areas based on the specifications for the SRTM DEM.

Table 5-9 Displacements caused by DEM error

Terrain type	Quasi nadir view (5°)	EnMAP max. off nadir view (30°)
Flat area ($\Delta h = 6m$; $\alpha = 0^\circ$)	0.5 m	3.5 m
Mountainous area ($\Delta h = 30m$; $\alpha = 20^\circ$)	2.7 m	21.9 m

5.6.2 Iterative Determination of Object Points

This step of orthorectification describes the intersection of the pixel view vector with the earth surface. For this purpose a model coordinate frame (index m) is introduced realized by a local topocentric system (LTS). To this end the LoS vectors, the state vectors and the DEM are transformed to a LTS with a fundamental point close to the scene centre (derived from the scene corner coordinates). The transformation of the DEM to the model coordinate frame includes a bilinear resampling with a pixel spacing of 30m (similar to the EnMAP HSI Ground Sampling Distance). The mathematics is described in Appendix B: Definitions of Coordinate Frames and Transformations.

The following iterative technique is established to calculate the intersection point.

Consider a reference surface at height h_0 . Starting with the analytically calculated intersection point of the sensor look direction with this surface leads to the terrain height h_1 given by the DEM. At this height again the intersection with the sensor look direction and a plane can be calculated. Repeating this procedure till the horizontal changes are less than the threshold of about half a pixel size (the threshold value is a parameter of the orthoimage processor and is set to 0.1 pixel size by default with maximal 10 iterations).

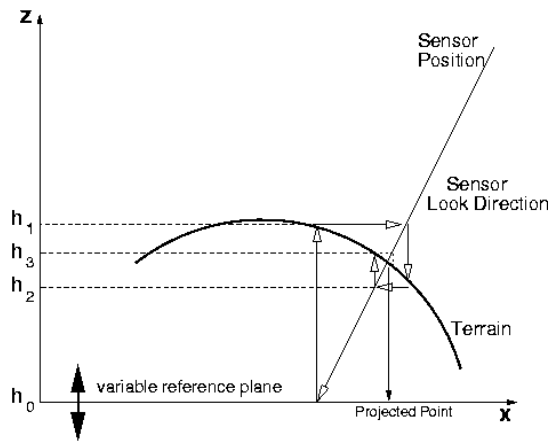


Figure 5-4 Method of determination of the actual sensor look direction with the DEM by an iterative approach

This iterative procedure is illustrated in Figure 5-4.

In order to establish the iterative procedure, first the intersection point with a plane surface at a constant height h_1 with respect to the mapping frame is considered:

Let $\mathbf{r}_{LoS}^m = \mathbf{R}_{Sensor}^m \cdot \mathbf{r}^{Sensor}$ the current pixel LoS vector and \mathbf{r}_{Sensor}^m the position of the projection centre of the sensor expressed in the mapping frame. The intersection point with a plane surface can be obtained by

$$\mathbf{r}_{Object}^m = \mathbf{r}_{Sensor}^m + \mu(h_1) \cdot \mathbf{r}_{LoS}^m \quad 5.6.2-1$$

$$\mu(h_1) = \frac{h_1 - (r_z)_{Sensor}^m}{(r_z)_{LoS}^m} \quad 5.6.2-2$$

where $(r_z)_{Sensor}^m$ and $(r_z)_{LoS}^m$ are the z-components of the vectors \mathbf{r}_{Sensor}^m and \mathbf{r}_{LoS}^m respectively. At the resulting plane co-ordinates of $(r_x)_{Object}^m$ and $(r_y)_{Object}^m$ the terrain height, given by the DEM expressed in the mapping coordinate frame, defines the new height h_2 of the plane surface, which serves as input for (3.12). Therefore the iteration can be written

$$\mathbf{r}_{Object}^m(h_{i+1}) = \mathbf{r}_{Sensor}^m + \mu(h_i) \cdot \mathbf{r}_{LoS}^m \quad 5.6.2-3$$

with h_i the terrain height value of the DEM at the plane coordinates of $\mathbf{r}_{Object}^m(h_i)$.

The starting terrain height h_0 (reference surface) has to be chosen as close as possible to the final one. Therefore the iterative procedure starts with the mean height values found for the adjacent pixels (the orthoimage processor uses the mean value of three adjacent pixels, which leads to a mean iteration of

about 1.1-1.4 cycles in moderate terrain). The point for the start value at height h_0 is calculated by intersection of the actual look direction with an ellipsoid:

Let $\mathbf{p}_{Object}^{ECR} = \mathbf{R}_{Sensor}^{ECR} \cdot \mathbf{r}_{Object}^{Sensor}$ the actual look direction of the sensor and $\mathbf{r}_{Sensor}^{ECR}$ the position of the projection centre of the sensor expressed in the ECR frame, then the intersection point with an ellipsoid can be written to

$$\mathbf{r}_{Object}^{ECR} = \mathbf{r}_{Sensor}^{ECR} + \mu(h_0) \cdot \mathbf{p}_{Object}^{ECR} \quad 5.6.2-4$$

On the other hand this intersection point has to fulfill the ellipsoid equation, where $A=a+h_0$ and $B=b+h_0$ with a the major axis, b the minor axis and h_0 the constant height above the earth ellipsoid:

$$\frac{(r_x^{ECR})_{Object}^2 + (r_y^{ECR})_{Object}^2}{A^2} + \frac{(r_z^{ECR})_{Object}^2}{B^2} = 1 \quad 5.6.2-5$$

Substituting the components of the vector (-4) in (-5) leads to the quadratic equation for the scale factor $\mu(h_0)$.

$$\left(\frac{x'^2+y'^2}{A^2} + \frac{z'^2}{B^2}\right) \cdot \mu(h_0)^2 + 2 \cdot \left(\frac{x \cdot x' + y \cdot y'}{A^2} + \frac{z \cdot z'}{B^2}\right) \cdot \mu(h_0) + \left(\frac{x'^2+y'^2}{A^2} + \frac{z'^2}{B^2} - 1\right) = 0 \quad 5.6.2-6$$

where $\mathbf{r}_{Sensor}^{ECR} = (x', y', z')^T$ and $\mathbf{p}_{Object}^{ECR} = (x, y, z)^T$.

For the two real solutions for $\mu(h_0)$ of this equation the smaller one (the first intersection with the surface) is used to determine the intersection point of the sensor look directions with a constant height above the ellipsoid surface. The found object point $\mathbf{r}_{Object}^{ECR}$ now can be transformed back to the mapping frame.

The resulting factor $\mu(h_i)$ after iteration is equivalent with the scaling factor s of (3.1).

5.7 Map Projections

Table 5-10 lists the map projections which are offered for EnMAP HSI geometric processing. The default is Universal Transverse Mercator (UTM) with the central meridian – namely the UTM zone number – derived from the scene center coordinates.

Table 5-10 Supported Map Projection

Identifier	Value range	Comment
Map_Projection	UTM_Zone_of_Scene_Center UTM_Zone_of_Scene_Center(-1) UTM_Zone_of_Scene_Center(+1) UTM_Zone_of_Datatake_Center Geographic European_Projection_LAEA	The LAEA-ETRS89 European projection can be only selected, if the acquisition area is inside the European frame.

The map projection formulas are of common engineering standard and are not redrawn here, but references are given.

5.7.1 Universal Transverse Mercator UTM

See RD-13, RD-14

In case the scene center latitude is above 84° N or below 80° S, the respective Universal Polar Stereographic (UPS) Projection is used automatically.

5.7.2 Geographic

See Appendix B: Definitions of Coordinate Frames and Transformations

Due to the distortions in high geographic latitudes and the resulting memory usage in processing, the possible area, where the Geographic projection can be used for EnMAP products is limited to a latitude between 67° S and 67° N. If the scene center is located outside of this area and the geographic projection is selected by the user, it will be changed to the default projection, namely UTM (Zone derived from scene center coordinates).

5.7.3 Lambert Azimuthal Equal Area ETRS89 (European Projection)

See RD-13

For EnMAP, the LAEA projection will only be used if the coordinates of the scene center fulfill the following condition: Longitude must be between 30° W and 50° E and latitude must be between 25° N and 79° N. If the condition is not fulfilled and LAEA is selected by the user, the projection will be changed to the default projection, namely UTM (Zone derived from scene center coordinates).

5.8 Image Resampling

Table 5-11 lists the image resampling methods which are offered for EnMAP HSI geometric processing. The default is Bilinear Interpolation. The side effects for Nearest Neighbor and Cubic Convolution resampling are noted in the "Comment" field.

Table 5-11 Supported image resampling methods

Identifier	Value range	Comment
Image_Resampling	Nearest_Neighbor Bilinear_Interpolation Cubic_Convolution	Cubic_Convolution resampling will result in reduced atmospheric correction accuracy in case of L2A product generation and Nearest Neighbor resampling will result in reduced co-registration accuracy between SWIR and VNIR instrument.

The image resampling is based on transformed polygons (triangles) from the image space to the object space as shown in Figure 5-5. The input image grid is covered by a dense net of triangles which are mapped to the output image grid. The resulting triangles are filled by interpolated pixel values using the different resampling methods. A pixel in the output image is inside the triangle if the centre of the pixel is inside the triangle. The inside test is performed with a scan converting algorithm for each pixel in the framing rectangle.

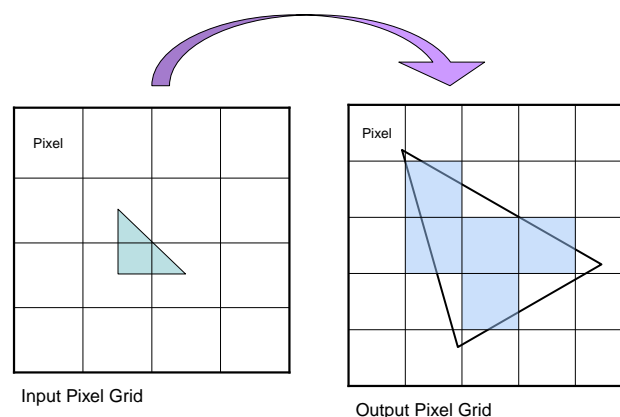


Figure 5-5 Polygons (triangles) of the input image, defined by the center of adjacent pixels, are transformed to the pixel grid of the orthoimage and filled with bilinear interpolated pixel value

The center of the upper-left corner pixel of the orthorectified scene is a multiple of the image resolution calculated by the formula

$$x_{UL} = x_{min} - drem(x_{min}, x_{res}) + \frac{x_{res}}{2} \quad \text{easting coordinate}$$

$$y_{UL} = y_{min} - drem(y_{min}, y_{res}) - \frac{y_{res}}{2} \quad \text{northing coordinate}$$

with the function $drem(a, b) = a - INT(\frac{a}{b})$

5.8.1 Nearest Neighbor

Consider a transformed triangle which contains a grid point with the coordinates (x, y) where a new pixel gray value has to be interpolated. Then the gray value at the point (x, y) is given by

$$g(x, y) = g_i(x_i, y_i) \text{ where } i = \min\{i | d_i = \sqrt{(x - x_i)^2 + (y - y_i)^2}; i = 1, \dots, 3\} \quad 5.8.1-1$$

Note: For the transformation of quality layers (e.g. cloud, land-water masks) the nearest neighbor resampling technique is applied.

5.8.2 Bilinear

Consider a transformed triangle, which contains a grid point with the coordinates (x, y) . At this point a new pixel gray value has to be interpolated. The gray value at the point (x, y) is then given by

$$g(x, y) = b_1 \cdot x + b_2 \cdot y + b_3 \quad 5.8.2-1$$

The three coefficients $\mathbf{b} = (b_1, b_2, b_3)^T$ are determined by the three gray values from the input image at the corner points $g_1(x_1, y_1)$, $g_2(x_2, y_2)$ and $g_3(x_3, y_3)$ of the transformed triangle

$$\begin{pmatrix} b_1 \\ b_2 \\ b_3 \end{pmatrix} = \begin{pmatrix} x_1 & y_1 & 1 \\ x_2 & y_2 & 1 \\ x_3 & y_3 & 1 \end{pmatrix}^{-1} \cdot \begin{pmatrix} g_1 \\ g_2 \\ g_3 \end{pmatrix} \quad 5.8.2-2$$

5.8.3 Cubic Convolution

The interpolation at point x can be described by the linear convolution operation

$$g_r(x) = f * g_d = \sum_{i=-\infty}^{\infty} f(x - x_i) \cdot g(x_i) \quad 5.8.3-1$$

Where f is the interpolation kernel, $g(x_i)$ is the discrete signal at point x_i , and $g_r(x)$ the interpolated signal at an arbitrary point x . The 4×4 kernel with the free parameter a is given by

$$f(x) = \begin{cases} (a+2) \cdot |x|^3 - (a+3) \cdot x^2 + 1 & |x| \leq 1 \\ a \cdot |x|^3 - 5 \cdot a \cdot x^2 + 8 \cdot a \cdot |x| - 4 \cdot a & 1 \leq |x| \leq 2 \\ 0 & \text{otherwise} \end{cases} \quad 5.8.3-2$$

For a 2-dimensional grid (equally spaced) the cubic convolution can be separated for the two spatial directions x and y which leads to

$$g_r(x, y) = \begin{pmatrix} f(1+d_y) & f(d_y) & f(1-d_y) & f(2-d_y) \end{pmatrix} \cdot \begin{pmatrix} g(x_1, y_1) & g(x_1, y_2) & g(x_1, y_3) & g(x_1, y_4) \\ g(x_2, y_1) & g(x_2, y_2) & g(x_2, y_3) & g(x_2, y_4) \\ g(x_3, y_1) & g(x_3, y_2) & g(x_3, y_3) & g(x_3, y_4) \\ g(x_4, y_1) & g(x_4, y_2) & g(x_4, y_3) & g(x_4, y_4) \end{pmatrix} \cdot \begin{pmatrix} f(1+d_x) \\ f(d_x) \\ f(1-d_x) \\ f(2-d_x) \end{pmatrix} \quad 5.8.3-3$$

with $d_x = x - INT(x)$ and $d_y = y - INT(y)$. For the a -factor the value $a = -2/3$ is chosen, which has to be shown to be optimal for digital images in the sense to approximate the sinc-function.

5.8.4 Dead pixel handling

Dead pixels will be interpolated in the L1B processor. Nevertheless, spatial resampling enlarges the area affected by a dead pixel.

5.9 Geolayer Generation

Instead of resampling the image data to an orthoimage as described above, it is also possible to generate a geolayer for the image data. A geolayer is a layer, i.e. additional channels, where the geolocation for each pixel is stored in geographic coordinates. Thus, each pixel is georeferenced, but the image is still in sensor geometry which is important e.g. for the smile correction. The resampling can then be done later in the processing chain with the methods described in chapter 5.8.

6. Improvements of Sensor Model Parameters

This chapter describes the improvement of the geometric accuracy of the orthorectified products using automatically extracted GCP from existing reference data sets. For the following cases the processing chain is not executed and the standard geometric processing is applied

- Reference images are not available for the area of interest
- Not sufficient GCP for the parameter improvement of the sensor model can be found and extracted from the reference images (e.g. area of interest contains only water, large differences between the EnMAP data and the reference images)

6.1 Processing Chain for Orthorectification

The processing chain uses as input the whole EnMAP datatakes (up to 1000 km in flight direction). This procedure

- increases the possibility to find sufficient GCP for the parameter improvement of the sensor model
- provides a consistent geometric correction of each image tile of the datatake based on improvement parameters valid for the whole datatake

Figure 6-1 illustrates the procedure of orthorectification using automatic GCP extraction from reference images in order to improve the geometric accuracy of the EnMAP images.

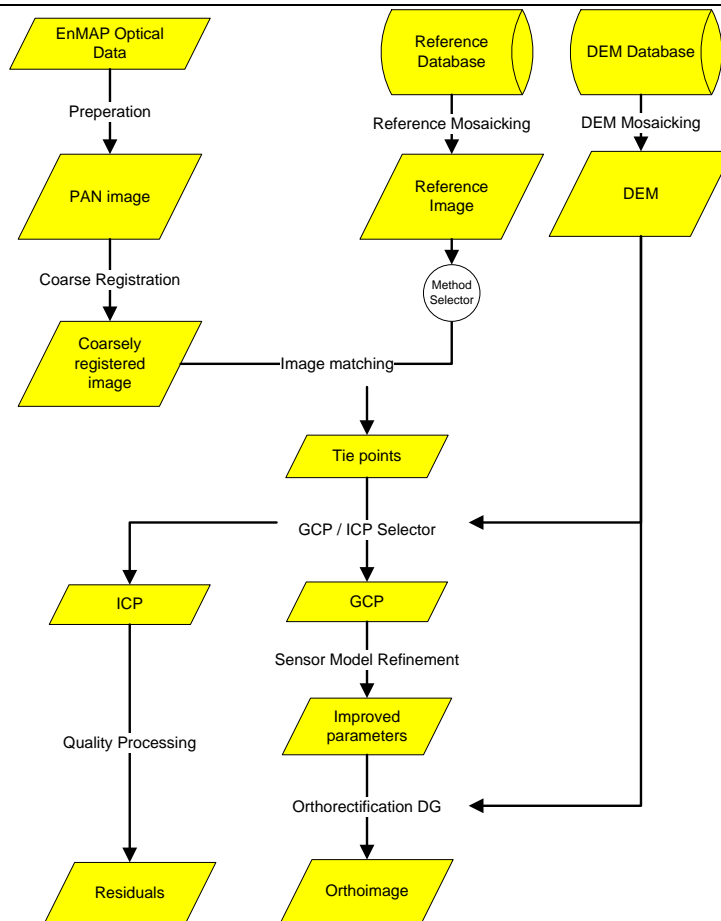


Figure 6-1 Overview of orthorectification using automatically extracted GCP

The automatic processing steps are

Preparation The preparation system selects from the EnMAP VNIR image data cube a set of channels in order to produce images which are suitable (e.g. radiometric similar for optical references) for matching with the images in the reference database. The current baseline is to generate two panchromatic images, one for VNIR and one for SWIR, using channels from the green (~500-590 nm), red (~610-680 nm), NIR (~780-890 nm) and SWIR (~1550 – 1750 nm) wavelength region respectively, but this has to be adjusted if the keystone effect cannot be neglected (in this case only one channel should be selected e.g. NIR due to the high contrast).

DEM & Reference Tile Generation Using the provided coarse image corner coordinates congruent tiles from the DEM database and from the reference image database are extracted and mosaicked with a margin of about 1 km (2 x 500 m according to the EnMAP pointing accuracy of 500 m) due to the pointing accuracy of the sensor.

Coarse Orthorectification Again based on the four image corner coordinates a coarse rectification using simple affine transformation is performed. The coarsely orthorectified images serves as input for an automatic image matching with the reference image tiles and is necessary as starting point for the hierarchical and shaded DEM matching algorithm.

Automatic tie point generation by matching In order to automatically extract GCP/ICP (Ground Control Points / Independent Control Points) from the reference data the following methods are applied (see Table 6-1)

Table 6-1 Methods of image matching techniques

Reference Source	Method of GCP Extraction for EnMAP HSI
Optical Data	Hierarchical intensity based matching
	SIFT matching

The different methods are described in detail in the following chapters.

GCP/ICP Generation The set of tie points is subdivided into GCP candidates used for the improvement of the sensor models and an ICP set used for geometric quality assessment. The selection of GCP is based on the requirement of equally distributed points over the scene with high quality figure. In order generate fully qualified three dimensional GCP the selected tie points are supplemented by bilinear interpolated DEM values extracted from the DEM tile.

Model Parameter Estimation Within the next processing step improved parameters (e.g. adjusted boresight alignment angles) for the orthorectification are estimated using the GCP information. Depending on the method and the reference data the GCP information is weighted within the Least Squares Adjustment. Iterative blunder detection is integrated, which eliminates step by step GCP with a residual greater than a threshold of 2 pixels starting with the bottom quality GCP.

Orthorectification The EnMAP VNIR and SWIR tiles are orthorectified independently using the DG technique which automatically achieves co-registered images.

Quality assessment The tie points of less quality serve as independent control points (ICP) to derive automatically a quality record (RMSE values, residual plots).

6.2 Intensity based Image Matching

6.2.1 Basic concept

The matching algorithm is described e.g. in RD-08, RD-11 and RD-12 and was originally developed for MEOSS and MOMS-2P 3-line along-track stereo scanner imagery. Figure 6-2 shows the scheme of the matching process.

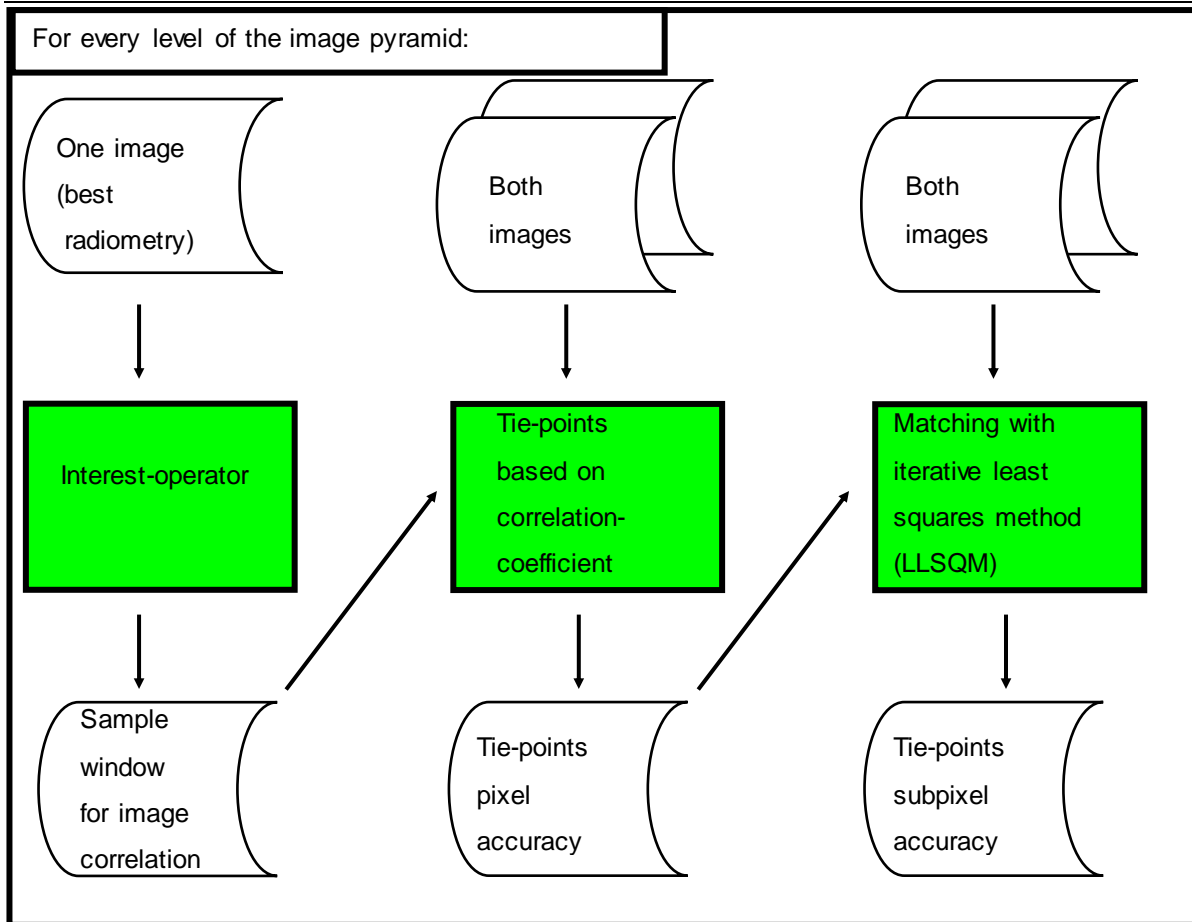


Figure 6-2 Processing scheme of the matching algorithm

Image pyramids: Image pyramids are computed for each image, e.g. the resolution is reduced by factors 2, 4, 8, 16 and 32. The optimal pyramid level is found by reducing the resolution as long as the image size is bigger than approximately 400 pixels in column or row direction. Each of the following steps will be computed for each pyramid level.

Förstner interest operator: To locate conjugate points in both reference and EnMAP images, possible matching points are selected. Patterns that are suitable for image correlation have to be selected in the reference image by applying an interest operator on the reference image. The so-called Förstner-operator, developed at Stuttgart University, is used here. For each window of a given size, the weighted center of gravity is computed by least squares technique with appropriate weighting by the first order derivatives in line and column directions. The observation equations are:

$$\begin{aligned} v_r + r &= r_0 \\ v_c + c &= c_0 \end{aligned} \tag{6.2.1-1}$$

With the weight matrix W

$$W = \begin{pmatrix} gr(r,c)^2 & gr(r,c) \cdot gc(r,c) \\ gr(r,c) \cdot gc(r,c) & gc(r,c)^2 \end{pmatrix} \tag{6.2.1-2}$$

Where gr and gc are the first derivatives in line and column directions. The normal matrix is built by a summation over all coordinate pairs of the window:

$$N = \begin{pmatrix} \sum gr^2 & \sum gr \cdot gc \\ \sum gr \cdot gc & \sum gc^2 \end{pmatrix} \tag{6.2.1-3}$$

The least squares adjustment returns an error ellipse, from which roundness Q and size W are extracted.

$$Q = 1 - \left(\frac{E_1 - E_2}{E_1 + E_2} \right)^2 = 4 \frac{\det(N)}{\text{trace}(N)^2}$$

$$W = \frac{1}{E_1} + \frac{1}{E_2} = \frac{\text{trace}(N)}{\det(N)} \quad 6.2.1-4$$

Where $E_1 \geq E_2$ are the Eigenvalues of the normal matrix N. Typical values for the roundness and variance thresholds are 0.85 and 25, respectively. Normally, a promising point is detected more than once with respect to different windows. The resulting set of points lying in immediate vicinity can be replaced by a single prominent point. This prominent point is selected based on four parameters, given in descending order of priority: multiplicity of point, variance of window, roundness of error ellipse and size of error ellipse.

Search area selection: After having selected promising patterns for the matching in the reference image, corresponding search areas have to be determined in the other image. This is achieved by using a local affine transformation between the images. The six transformation parameters are determined by a least squares adjustment using already known homologous points. For the initial step at the lowest level of the image pyramid, the transformation is an identity transformation, which is sufficient at this resolution. At the other levels of the pyramid, the results of the previous pyramid level are used as input for the calculation of the transformation parameters.

Normalized correlation coefficient: Now, prominent patterns in the reference image and search areas in the second image are defined by the previous steps. For each corresponding pair a matrix C of normalized correlation coefficients c_{ij} is computed by shifting the pattern pixel by pixel in both row and column directions over the search area:

$$c_{ij} = \frac{\sum_{l=1}^{npl} \sum_{k=1}^{npc} (g1_{i+l-1, j+k-1} - g1av)(g2_{lk} - g2av)}{\sqrt{\sum_{l=1}^{npl} \sum_{k=1}^{npc} (g1_{i+l-1, j+k-1} - g1av)^2 \cdot \sum_{l=1}^{npl} \sum_{k=1}^{npc} (g2_{lk} - g2av)^2}} \quad 6.2.1-5$$

Where

$$1 \leq i \leq nsl - npl + 1$$

$$1 \leq j \leq nsc - npc + 1$$

And where nsl, npl are the number of lines in the search area and in the pattern area respectively; nsc, npc are the numbers of columns in the respective area.

The average of the grey values in the search area is calculated:

$$g1av = \frac{1}{npl \cdot npc} \sum_{l=1}^{npl} \sum_{k=1}^{npc} g1_{i+l-1, j+k-1} \quad 6.2.1-6$$

As well as the average of the grey values in the pattern area:

$$g2av = \frac{1}{npl \cdot npc} \sum_{l=1}^{npl} \sum_{k=1}^{npc} g2_{lk} \quad 6.2.1-7$$

Where g1, g2 are the grey values in the search and the pattern area respectively. The location of the maximum of the correlation coefficients defines the pixel that corresponds to the center of the pattern in the reference image. This results in matching points with pixel accuracy.

Local least squares matching: To refine the results to subpixel accuracy, a local least squares matching is performed on the imagery. Therefore, the eight parameters of a local radiometric (brightness and contrast) transformation

$$g_1 = h_1 + h_2 \cdot g_2 \quad 6.2.1-8$$

and a local affine transformation

$$\begin{aligned} r_2 &= a_1 + b_1 \cdot r_1 + d_1 \cdot c_1 \\ c_2 &= a_2 + b_2 \cdot r_1 + d_2 \cdot c_1 \end{aligned} \quad 6.2.1-9$$

between the images are estimated using an iterative least squares adjustment. As observations, the grey value differences between the images are used (Ackermann, 1984).

$$\sum (g_1(x, y) - (h_1 + h_2 * g_2(\text{traf}(x, y))))^2 \quad 6.2.1-10$$

is minimized, where g_1, g_2 are the grey values of the respective image, h_1, h_2 are offset and gain of the radiometric transformation and $\text{traf}(x, y)$ is the affine transformation. Convergence is assumed, if given thresholds for the change in values h_2 and the six parameters of the affine transformation are reached before a given number of iterations. If no convergence is reached, the subpixel position is computed via the local maximum of a parabolic fit in the correlation matrix.

6.2.2 Blunder reduction

During the matching process, several blunder reduction methods are applied in different processing steps to minimize mismatches.

Search area selection: To avoid blunders in the search window position, the results of the local affine transformation are accepted only if the RMSE for the input homologous points is less than half the possible shift of the pattern area within the search area. By changing the number of the input points and the weighting, more trials are made. If no adjustment is accepted, no matching is performed for this particular point.

Normalized correlation coefficient: The uniqueness and relative steepness of the peak in the correlation matrix are measured in a quality figure q .

$$q = \frac{1}{n} \cdot \left(c_1 + \sum_{k=2}^n \frac{c_1 - c_k}{\sqrt{(i_1 - i_k)^2 + (j_1 - j_k)^2}} + c_1 - c_1 av \right) \quad 6.2.2-1$$

where

$$c_1 av = \frac{1}{8} \left(\sum_{l=-1}^1 \sum_{k=-1}^1 c_{i_{max} + l, j_{max} + k} - c_1 \right) \quad 6.2.2-2$$

is the average of the 8 neighboring correlation coefficients in C . To avoid mismatches, each correlation process has to fulfill two conditions to be accepted: Thresholds are given for the maximum correlation and the quality figure; typical values are 0.5 and 0.2, respectively. And the maximum of the correlation coefficients must not lie on the border of the matrix. This condition helps to avoid mismatches caused by repetitive patterns.

Bidirectional correlation: After the matching in the image pyramid is performed, the results are used to start a local least squares matching on the images in both directions; reference image to second image and vice versa. Deviations from the original image coordinates are registered and afterwards used for the selection of high quality tie points based on thresholds.

6.3 SIFT Matching

The SIFT operator is a computer vision algorithm first introduced by David Lowe in 1999 [2]. The method provides a robust technique to extract distinctive features from an image. These features are invariant to image scale and rotation, which makes them well suited to match different views of an object or scene. In 2004 Lowe published a revised version of the SIFT operator with several improvements in terms of feature accuracy, stability and invariance [3].

The implementation used for EnMAP is complemented by a RANSAC algorithm for the outlier detection. It is described in detail in [RD-50].

6.4 Optical Reference Image Databases

The geometric accuracy of the EnMAP orthoimages derived by Direct Georeferencing can be improved using Ground Control Point information to refine the parameter sets of the Line-of-Sight model. Image-to-image matching algorithms (6.2, 6.3) permit the automatic extraction of Ground Control Points provided that existing orthoimages of superior geometric quality as global or local reference images are supplied. Section 6.4.1 outlines the requirements for such a reference image database. In section 6.4.2, the used global reference image database is presented.

6.4.1 Requirements for Reference Database

To assure an improvement in geolocation accuracy derived by direct georeferencing, Reference Images shall fulfill a number of requirements. These include the following issues:

- The Geometric Sampling Distance (GSD) of EnMAP is specified with 30m x 30m at nadir. The spatial resolution of reference images should be as a minimum equivalent, or superior to the EnMAP sensor.
- Reference Images are requested to feature an absolute geometric accuracy less than one EnMAP pixel (i.e. <30m) to achieve an utmost geolocation accuracy of L1C products.
- Image matching algorithms applied therein operate reasonably well with panchromatic image data or with one spectral band rich in contrast (e.g. NIR). Thus, the spectral resolution of Reference Images is of minor importance. However, multispectral bands are treated as an add-on although it entails an enormous memory capacity.
- In general, it would be desirable to use only cloud-free Reference Images, but due to persistent cloudiness in many parts of the world this is impossible. Depending on the cloud distribution, cloud covered images may be used partly. If obtainable, multiple scenes together may provide supplementary information missed by only selecting one scene or the other.
- The time of acquisition of Reference Images and images to georeference are preferably close to one another. The lesser the time lag (in years and in days), the higher the chances of success in automatic extraction of Ground Control Points, particularly in highly dynamic urban or rural regions and agricultural dominated landscapes.

6.4.2 Reference Database

A reference image database consisting of Sentinel-2 L1C images was generated for use in the EnMAP L1C processor. The Sentinel-2 system is operational since 2015. During the commissioning phase, a global coverage was created to serve as a global reference database for the processing of the Sentinel-2 data to assure a high relative accuracy for all Sentinel-2 products. Also, the absolute accuracy is defined as 12.5 m or better. This makes the Sentinel-2 reference database an optimal option for the EnMAP reference database. The selection of the Sentinel-2 scenes for the reference image database was based on cloud coverage and time of acquisition.

6.5 Mathematics of Model Parameter Estimation (inverse modeling)

Complementing the tie points found in the orthorectified reference data – assumed to be of superior absolute geometric quality – with interpolated height values from the DEM leads to fully qualified 3D GCP, which are connected to the conjugated image coordinates – expressed in line/column values – of the EnMAP HSI optical data. These GCP are used to improve the sensor model of the optical system. Especially thermal effects caused by the sun exposure time during satellite orbit revolution influences the relative alignment between the body and the sensor coordinate frames and leads to pointing errors. Therefore, by iterative least squares adjustment improved boresight alignment angles are estimated and introduced in the physical sensor model. Within the least squares adjustment simple, iterative blunder detection is integrated, which eliminates step by step GCP with a residual greater than a threshold (e.g. 1-2 pixel sizes) starting with the bottom quality GCP. Finally, the sensor model with improved parameters is applied to orthorectify the EnMAP HSI optical data. Because different reference data sets and methods are in use to extract tie points for parameter estimation, rules for weighting of the GCP have to be applied. The individual steps are described in the next chapters.

6.5.1 Least Squares Adjustment

Using GCP a refinement of model parameters by iterative least squares adjustment can be performed in order to achieve an improvement of the geometric accuracy of the orthoimages. As mentioned in the previous chapters image-to-image matching techniques can be used to generate – in combination with interpolated DEM values – automatically GCP.

The relation between image space and object space coordinates is after rearranging the collinearity equation of the form

$$\mathbf{r}_{Object}^{Sensor} = \begin{pmatrix} x_{Object}^{Sensor} \\ y_{Object}^{Sensor} \\ -f \end{pmatrix} = \frac{1}{s} \begin{pmatrix} c_{11} & c_{12} & c_{13} \\ c_{21} & c_{22} & c_{23} \\ c_{31} & c_{32} & c_{33} \end{pmatrix} \begin{pmatrix} x_{Object}^m - x_{Sensor}^m \\ y_{Object}^m - y_{Sensor}^m \\ z_{Object}^m - z_{Sensor}^m \end{pmatrix} = \frac{1}{s} \mathbf{C} \cdot (\mathbf{r}_{Object}^m - \mathbf{r}_{Sensor}^m) \quad 6.5.1-1$$

with

$$\mathbf{C} = (\mathbf{R}_{body}^{sensor} \cdot \mathbf{R}_{sensor}^{body}(\boldsymbol{\varepsilon}))^{-1}$$

where the boresight alignment matrix shall be improved by the additional angles $\boldsymbol{\varepsilon} = \{\varepsilon_1, \varepsilon_2, \varepsilon_3\}$. The equations for the x- and the y- image co-ordinates can be divided by the equation for the z- image co-ordinate. The scale factor s cancels out.

$$\begin{aligned} x_{Object}^{Sensor} &= -f \cdot \frac{c_{11}(x_{Object}^m - x_{Sensor}^m) + c_{12}(y_{Object}^m - y_{Sensor}^m) + c_{13}(z_{Object}^m - z_{Sensor}^m)}{c_{31}(x_{Object}^m - x_{Sensor}^m) + c_{32}(y_{Object}^m - y_{Sensor}^m) + c_{33}(z_{Object}^m - z_{Sensor}^m)} \\ y_{Object}^{Sensor} &= -f \cdot \frac{c_{21}(x_{Object}^m - x_{Sensor}^m) + c_{22}(y_{Object}^m - y_{Sensor}^m) + c_{23}(z_{Object}^m - z_{Sensor}^m)}{c_{31}(x_{Object}^m - x_{Sensor}^m) + c_{32}(y_{Object}^m - y_{Sensor}^m) + c_{33}(z_{Object}^m - z_{Sensor}^m)} \end{aligned} \quad 6.5.1-2$$

In this equations the functions for x_{Object}^{Sensor} and y_{Object}^{Sensor} depend on the three unknown angles $\boldsymbol{\varepsilon} = \{\varepsilon_1, \varepsilon_2, \varepsilon_3\}$. A GCP is given by the measured image coordinates $x_{GCP}^{sensor}, y_{GCP}^{sensor}$ and the corresponding object space coordinates \mathbf{r}_{GCP}^m which are inserted into the equations. To this end the non-linear functions are linearized with respect to the three unknowns $\boldsymbol{\varepsilon} = \{\varepsilon_1, \varepsilon_2, \varepsilon_3\}$ by Taylor expansion and evaluated at the interpolated exterior orientation parameters at the GCP which leads to

$$\begin{aligned} x_{GCP}^{sensor} - x_{Object}^{sensor} \Big|_{GCP} &= \sum_k \frac{\partial x_{Object}^{sensor}}{\partial \varepsilon_k} \Big|_{GCP} d\varepsilon_k \\ y_{GCP}^{sensor} - y_{Object}^{sensor} \Big|_{GCP} &= \sum_k \frac{\partial y_{Object}^{sensor}}{\partial \varepsilon_k} \Big|_{GCP} d\varepsilon_k \end{aligned} \quad 6.5.1-3$$

The left side of the equation shows the difference between the measured GCP and the calculated one, and the right side of the equation expresses the improvement by the refined boresight alignment angles. For the GCP set ($i=1, \dots, Amount\ of\ GCP$) this leads to the system of linear equations

$$\mathbf{p} = \begin{pmatrix} \vdots \\ x_{GCP}^{Sensor\ i} - x_{Object}^{Sensor\ i} \Big|_{GCP} \\ y_{GCP}^{Sensor\ i} - y_{Object}^{Sensor\ i} \Big|_{GCP} \\ \vdots \end{pmatrix} = \begin{pmatrix} \vdots \\ \frac{\partial x_{Object}^{Sensor}}{\partial \varepsilon_x} \Big|_{GCP}^i & \frac{\partial x_{Object}^{Sensor}}{\partial \varepsilon_y} \Big|_{GCP}^i & \frac{\partial x_{Object}^{Sensor}}{\partial \varepsilon_z} \Big|_{GCP}^i \\ \frac{\partial y_{Object}^{Sensor}}{\partial \varepsilon_x} \Big|_{GCP}^i & \frac{\partial y_{Object}^{Sensor}}{\partial \varepsilon_y} \Big|_{GCP}^i & \frac{\partial y_{Object}^{Sensor}}{\partial \varepsilon_z} \Big|_{GCP}^i \\ \vdots \end{pmatrix} \begin{pmatrix} d\varepsilon_x \\ d\varepsilon_y \\ d\varepsilon_z \end{pmatrix} = \mathbf{A} \cdot \mathbf{x} \quad 6.5.1-4$$

which is solved iteratively by successive approximation. The Jacobian $\mathbf{A} = \left(\frac{\partial x_i}{\partial \varepsilon_j}\right)$ changes from one iteration to the next. For a number of GCP (here min. 2 GCP) the system of linear equations is solved by iterative least squares adjustment.

$$\mathbf{x} = (\mathbf{A}^T \mathbf{A})^{-1} \mathbf{A}^T \mathbf{p} \quad 6.5.1-5$$

Introducing a weight matrix to account for the different sets of GCP derived from the three matching methods finally leads to

$$\mathbf{x} = (\mathbf{A}^T \mathbf{W} \mathbf{A})^{-1} \mathbf{A}^T \mathbf{W} \mathbf{p} \quad 6.5.1-6$$

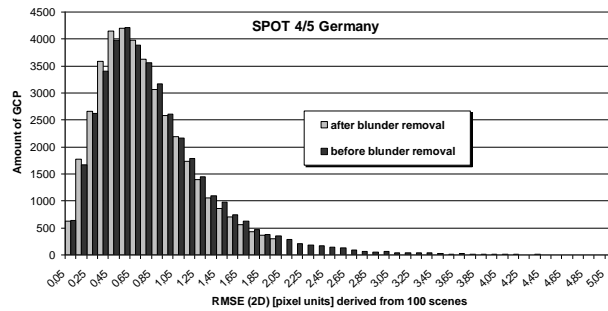


Figure 6-4 Histogram of the residuals ($RMSE_{xy}$) after least squares adjustment for 100 SPOT 4 HRVIR and SPOT 5 HRG scenes. Dark bars: before blunder removal; bright bars: after blunder removal using 2 pixel sizes as GCP rejection level.

The drawback of this method is that systematic errors for the majority of the GCP can lead to erroneous or shifted values of the estimated parameters. Another possible error source is obtained by a poor distribution of the GCP concentrated in only one part of the scene and a model estimated from such a distribution might not be ideal and consistent for the entire scene.

7. Rational Polynomial Functions

This chapter describes the Rational Polynomial Coefficients (RPC) generated from the rigorous sensor model

7.1 Generation of Rational Polynomial Coefficients

Exterior and interior orientation can be implicitly encoded in the form of rational polynomial functions (RPF) (RD-10)). This Universal Sensor Model (USM) provides the transformation of object space coordinates to image space coordinates, which is available in standard format for many remote sensing satellite systems. Each of the Rational Polynomial Functions (RPF) for row and column is given via a ratio of 2 polynomials of 3rd order in longitude λ , latitude ϕ , and ellipsoidal height h (geographic coordinates with WGS84 datum) with 20 coefficients each.

$$\begin{aligned} r &= rpf_r(\lambda, \phi, h) \\ c &= rpf_c(\lambda, \phi, h) \end{aligned} \tag{7.1-1}$$

where r/c are row and column coordinates of the image and λ , ϕ , and h are longitude, latitude and ellipsoidal height in geographic coordinates of WGS84 datum.

For numerical reasons the calculation is actually based on normalized variables restricted to the interval $[-1,+1]$ by choosing appropriate values for offset and scale which are provided together with the coefficients of the polynomials:

$$r_n = \frac{r-r_0}{r_s}, c_n = \frac{c-c_0}{c_s}, v = \frac{\lambda-\lambda_0}{\lambda_s}, u = \frac{\phi-\phi_0}{\phi_s}, w = \frac{h-h_0}{h_s} \text{ offset : } r_0, \dots, h_0, \text{ scale : } r_s, \dots, h_s \tag{7.1-2}$$

The normalized values r_n and c_n of the image coordinates are given as ratio of third order polynomials in u, v and w :

$$r_n = \frac{a_1+a_2v+a_3u+a_4w+\dots+a_{20}w^3}{1+b_2v+b_3u+b_4w+\dots+b_{20}w^3}, c_n = \frac{d_1+d_2v+d_3u+d_4w+\dots+d_{20}w^3}{1+e_2v+e_3u+e_4w+\dots+e_{20}w^3} \tag{7.1-3}$$

In summary the coefficients used in the RPF are derived from the LoS model used in Direct Georeferencing and therefore the geometric accuracy of orthorectification is less or equal to the results received from Direct Georeferencing.

The method to estimate the RPC from DG is illustrated in Figure 7-1. Using the rigorous sensor model object points (longitude, latitude, ellipsoid height) are created in a horizontal grid of 50 x 50 pixel and 10 vertical height steps between minimum and maximum height of the region of interest. Iterative least squares adjustment is applied to solve the non-linear equations for the unknown RPC.

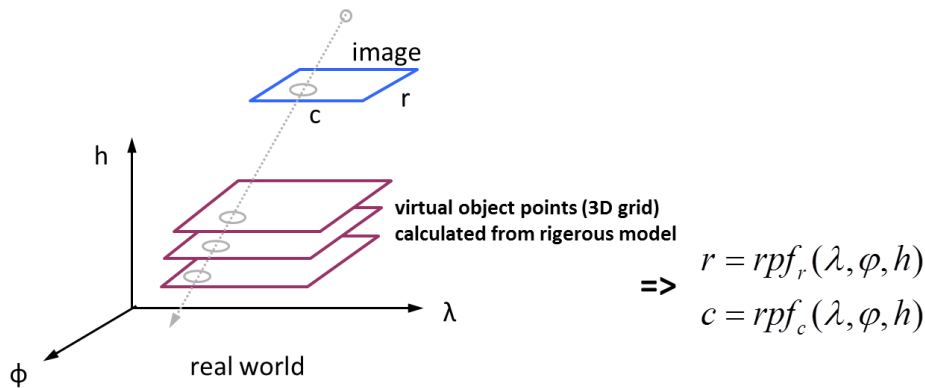


Figure 7-1 Virtual object points from rigorous sensor model to estimate RPC by least squares adjustment

8. VNIR – SWIR Co-registration

As mentioned in chapter 4.4 “The EnMAP Mission and Instrument Characteristics” the HSI consists of two instruments covering the VNIR and the SWIR spectral wavelength part. The in-field separation employing two entrance slits for the two instruments leads to a divergence angle of about 3.16 arcmin. The following chapter describes a simulation to derive the achievable co-registration accuracy using an idealized pushbroom sensor model (no internal camera geometric errors).

8.1 Simulation of Co-registration Accuracy

To evaluate the achievable co-registration accuracy, a geometric simulator for EnMAP was implemented (RD-25). This simulator works by computing artificial orbit and attitude data to virtually acquire VNIR and SWIR scenes of an existing remote sensing image. These images are then corrected using the DLR in-house developed orthorectification processor ORTHO and their relative accuracy is measured. By running the simulation once using correct AOCS data and once using AOCS data flawed by attitude controller errors, this way it is possible to evaluate the influence of the attitude controller error on the co-registration accuracy.

Here, a sinusoidal attitude error with amplitude of 0.02° and a frequency of 1/15 Hz was assumed. As the measurements of the attitude data are available only with a frequency of 1 Hz, a sinusoidal function is fitted to the attitude measurements (which themselves are flawed by an attitude knowledge error, simulated by a randomized normal distribution with a standard-dev. of 0.0037°) using least squares fitting to obtain a good estimate of the real attitude data (see Figure 8-1).

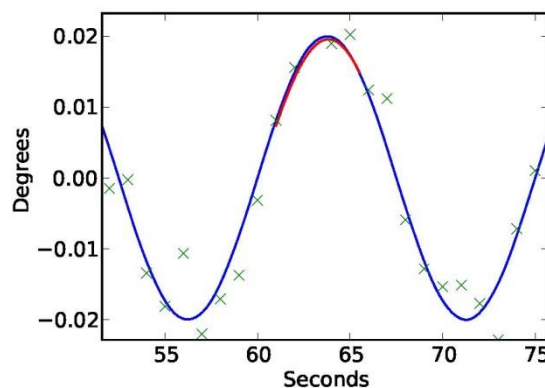


Figure 8-1 Example of the approximation of the attitude controller deviation. Blue: the real deviation; Green: periodic attitude measurements including pointing knowledge error; Red: Approximated deviation for the duration of an EnMAP scene

The co-registration accuracy between the orthorectified VNIR and SWIR scenes was calculated by acquiring point matches between the two scenes using a pyramid based matching approach with an accuracy of up to 0.1 pixels. The averaged results for 1000 simulated EnMAP scenes can be seen in Table 8-1.

Table 8-1 Absolute mean displacement and standard deviation between the matches found in the orthorectified VNIR and SWIR images in meters (generated over 1000 iterations)

		X	Y
Correct AOCS data	Mean	0.739 m	1.403 m
	Std.-Dev	3.103 m	2.640 m
Approximated AOCS data	Mean	1.122 m	1.542 m
	Std.-Dev	3.554 m	4.321 m

It should be noted that the standard deviation of ~3 m for the correct AOCs data is mostly a result of matching inaccuracies, as the absolute accuracy of these scenes was also calculated using a different, more rigid approach, and was shown to be better than 1 m (see RD-25 for more details).

The fact that the mean displacement as well as the standard deviation is only marginally better when using the correct AOCs data compared to the approximated AOCs data, shows that the co-registration accuracy for the second case is not really much worse. Assuming that here matching in-accuracies are also responsible for most of the displacements, the co-registration accuracy can be expected to be better than 3 m on average.

9. Product Quality Indicators

The following chapters describe the product quality indicators generated by the functionalities of the L1C processor. If appropriate and sufficient GCP / ICP can be automatically extracted from reference images to refine the sensor model parameters a more detailed quality record is generated. Otherwise predefined values from pre- and post-launch performance analysis are provided.

9.1 Root Mean Square Values (orthoRMSE)

The geometric accuracy of the orthoimages is assessed at the ICP that result from image matching of the EnMAP scene to reference images. The Root Mean Square Error (RMSE) is therefore a relative error with respect to the reference images. For $i=1, \dots, N$ measurements the RMSE is given by

RMSE Map Point Error 1D

Let $\Delta X_i = X_{image,i} - X_{reference,i}$ and $\Delta Y_i = Y_{image,i} - Y_{reference,i}$

$$RMSE_{E_x}^2 = \frac{1}{N} \sum_i \Delta X_i^2$$

$$RMSE_{E_y}^2 = \frac{1}{N} \sum_i \Delta Y_i^2$$

RMSE Map Point Error 2D

$$RMSE_{E_{xy}} = \sqrt{RMSE_{E_x}^2 + RMSE_{E_y}^2}$$

Relation to other error measures

Let V_i a measurement then the relation of the RMSE to the mean value μ and the standard deviation σ is given by

$$RMSE_{E_v}^2 = \frac{N-1}{N} \sigma^2 + \mu^2$$

with $\mu = \frac{1}{N} \sum_i V_i$ and $\sigma^2 = \frac{1}{N-1} \sum_i (\mu - V_i)^2$

which leads for $N \gg 1$ to the relation

$$RMSE_{E_v}^2 \approx \sigma^2 + \mu^2$$

Note: The circular error $CE90$ is the radial error, which 90% of all errors in a circular distribution will not exceed. If the ratio of the standard deviations in both directions $\frac{\sigma_{MIN}}{\sigma_{MAX}}$ is in the range of about 0.8-1.0, then the $CE90$ can be approximated to $CE90 \approx 1.52 \cdot RMSE_{E_v}$

Note: If $\sigma_x = \sigma_y$, then the "2D Map Point Error" is approximately given by the radial error $CE63$, which 63% of all errors in a circular distribution will not exceed.

Note: By Least Squares Adjustment the mean deviation μ will be minimized, which leads to $RMSE_{E_v} \approx \sigma$

If ICP are not available, the standard values are given as quality indicator for the geometric accuracy of the orthorectified scene.

$$RMSE_x = 100m, RMSE_y = 100m, RMSE_{xy} = 142m$$

9.2 Residual Plot (orthoResidual)

The geometric accuracy of the orthoimages is assessed at the ICP that result from image matching of the EnMAP scene to reference images. The residual plot is therefore a relative error with respect to the reference images. The residual plot shows graphically the deviation of ICP derived from the reference images with the calculated object points by the L1C processor. An example of a residual plot is shown in Figure 9-1.

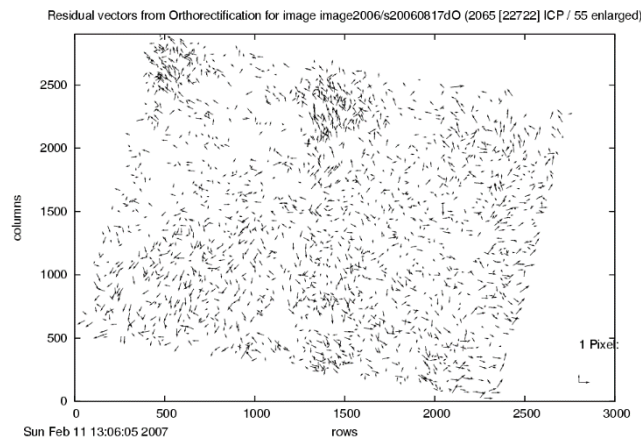


Figure 9-1 Example of a residual plot, which shows the deviations in pixel – here by factor 55 enlarged - of automatically determined ICPs from the reference image versus image coordinates of the orthorectified scene after correction with GCPs

If ICP are not available, no residual plot is provided.

9.3 DEM related Errors (orthoTerrain)

The geometric displacement (or error) Δs caused by the DEM height error Δh depends on the off-nadir view angle ω and the terrain slope angle α . The off-nadir angle is constant during acquisition of a scene. The terrain slope is the mean value derived from the DEM covering the scene area. The DEM related displacement is given by

$$\Delta s = \frac{\Delta h \cdot \tan \omega}{1 - \tan \alpha \cdot \tan \omega}$$

The DEM height error Δh is specified by the DEM database product as quality layer or at least as height error value classified for flat, hilly and mountainous areas.

10. Metadata

Besides the parameters described in previous sections, the L1C processor provides also viewing angles in the metadata. All types of angles are provided for the four corners and the center of each tile. The calculation is performed in local topocentric systems (LTS) with the fundamental point directly under the satellite on Earth surface, the y-axis pointing towards north, the x-axis pointing towards east and the z-axis pointing upwards. See section 14 (Appendix B) for details. Different LTS are used for the respective points. The calculation of the angles is described hereafter. Note that for all $\tan^{-1} \frac{a}{b}$, the atan2 function is used.

10.1 Scene Azimuth Angle

The scene azimuth angles are describing the orientation of the scene against north. They are calculated in local topocentric systems (LTS) with the origin being the point directly under the satellite at beginning and end of image acquisition respectively. The azimuth angle is then calculated as follows:

$$\alpha_i = \tan^{-1} \frac{x_{start}^{LTS\ i} - x_{end}^{LTS\ i}}{y_{start}^{LTS\ i} - y_{end}^{LTS\ i}} \quad 10.1-1$$

Where i is start or end of image acquisition and X, Y are the positions of the satellite in the respective LTS.

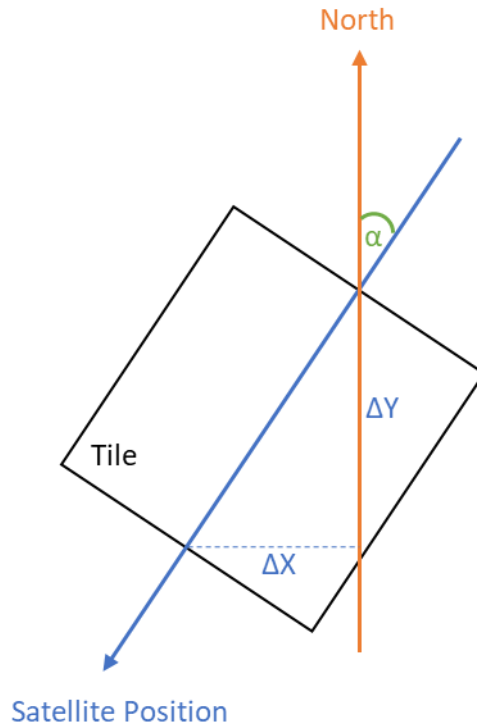


Figure 10-1: Scene azimuth angle (nadir case)

10.2 Off-Nadir Angles

The across and along track off-nadir angles are calculated using the same LTS as above, the scene azimuth angle as described above, the satellite position and the image corner coordinates. The satellite position coordinates and the corner coordinates are transformed into LTS coordinates and rotated around the z-axis by the scene azimuth angle.

$$\begin{pmatrix} X_{rot}^j \\ Y_{rot}^j \\ Z_{rot}^j \end{pmatrix} = \begin{bmatrix} \cos \alpha_j & -\sin \alpha_j & 0 \\ \sin \alpha_j & \cos \alpha_j & 0 \\ 0 & 0 & 1 \end{bmatrix} \cdot \begin{pmatrix} X_j \\ Y_j \\ Z_j \end{pmatrix} \quad 10.2-1$$

Where j is corner/center or satellite coordinate and α_j is the respective scene azimuth angle. The along track off-nadir angles are then calculated as follows:

$$\theta_i = \tan^{-1} \frac{y_{rot}^{sat} - y_{rot}^i}{z_{rot}^{sat} - z_{rot}^i} \quad 10.2-2$$

The across track off-nadir angle is calculated as follows:

$$\beta_i = \tan^{-1} \left(\cos \theta_i * \frac{y_{rot}^{sat} - x_{rot}^i}{z_{rot}^{sat} - z_{rot}^i} \right) \quad 10.2-3$$

where i is the corner/center (UL, UR, LR, LL, C) and X, Y, Z are the coordinates of the satellite position or corner respectively at the time the respective pixel was acquired, all in the rotated LTS as described above.

The along track off-nadir angle is usually quite small, while the across track off-nadir angle can vary from -30° to $+30^\circ$. If the across track off-nadir angle is negative, the satellite is looking left (wrt. flight direction), i.e. in a descending orbit it looks eastwards. If the along track off-nadir angle is negative, the satellite is looking backwards (wrt. flight direction), i.e. in a descending orbit it looks northwards.

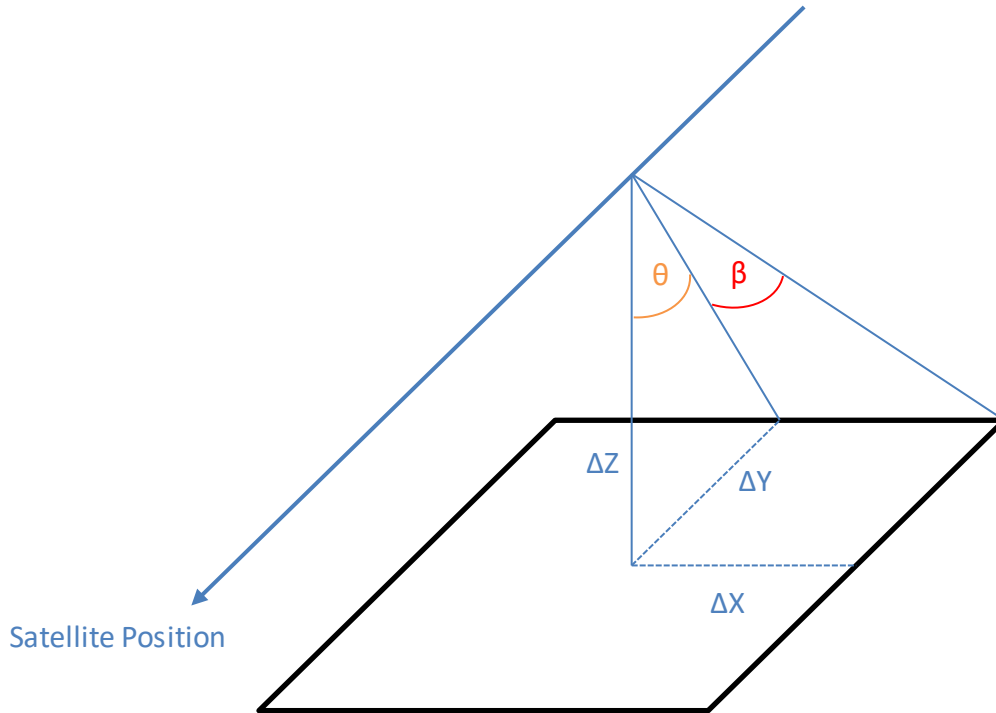


Figure 10-2: Along-track (θ) and across-track (β) off-nadir angles

10.3 Viewing Zenith Angle

Since processor version 01.05.00, the viewing zenith angles of the scene center and the four corners are calculated during processing and provided in the Lx metadata to the users. The angles are calculated in an LTS using the scene center as origin.

$$\zeta_i = \tan^{-1} \frac{\sqrt{|x_{sat}^t - x_i|^2 + |y_{sat}^t - y_i|^2}}{|z_{sat}^t - z_i|} \quad 10.3-1$$

Where i is the corner/center (UL, UR, LR, LL, C) and X, Y, Z are the coordinates of the satellite position (sat) or corner/center (i) respectively at the time of acquisition of the respective pixel (t). All X, Y, Z are transformed into the LTS as described above.

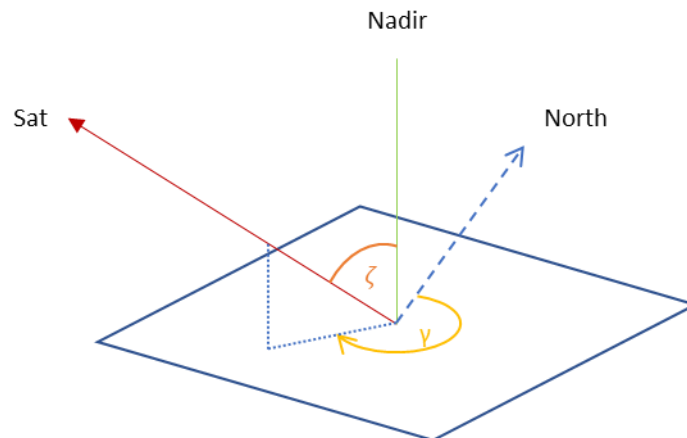


Figure 10-3: Viewing zenith and azimuth angle

10.4 Viewing Azimuth Angle

Since processor version 01.05.00, the viewing azimuth angles of the scene center and the four corners are calculated during processing and provided to the users in the Lx metadata. The angles are calculated in an LTS using the scene center as origin.

$$\gamma_i = \tan^{-1} \frac{x_{sat}^t - x_i}{y_{sat}^t - y_i} \quad 10.4-1$$

Where i is the corner/center (UL, UR, LR, LL, C) and X, Y, Z are the coordinates of the satellite position (sat) or corner/center (i) respectively at the time of acquisition of the respective pixel (t). All X, Y, Z are transformed into the LTS as described above.

11. Verification

The following sections confirm by independent evidence that the requirements for the geometric accuracy can be fulfilled.

First the geometric accuracy analysis by standard geometric processing is discussed, which uses the on-board measurement systems without refinement by GCP. Second the geometric accuracy by auxiliary geometric processing is presented, which uses a refined sensor model using GCP information automatically extracted from reference images.

11.1 Standard Geometric Processing

The estimation of the pointing knowledge is based on the error budget described in AD-20. A Monte Carlo simulation has been performed using the sensor model described in the previous sections (see AD-19 for a detailed description of the simulation). The simulation only includes fast sine, slow sine and random errors. Bias errors are assumed to be fully calibrated. Influences caused by terrain distortion are not included. Additionally, errors caused by the vibrations of the cooler compressor and reaction wheels are not included. In Table 11-1 the geometric accuracy on ground is shown for different across track viewing angles of the sensor. The yellow marked row is for nadir view, which is related to the requirement specification.

Table 11-1 Pointing knowledge simulated with sensor model used for EnMAP (not all error influences are included)

Across Track Sensor View Direction	σ_{xy} [m] CE63 (2D error)	σ_x [m] along track LE68 (1D error)	σ_y [m] across track LE68 (1D error)
0°	93.5	66.7	65.5
5°	97.1	69.4	68.4
10°	98.9	70.0	69.9
20°	105.5	72.8	76.3
30°	118.4	78.0	89.0

11.2 Auxiliary Geometric Processing

On behalf of the European Space Agency (ESA) the geometric processing chain as described in the previous sections, has been applied for different projects – namely the UrbanAtlas and Image2006 project - using SPOT 4 HRVIR, SPOT 5 HRG¹, IRS-P6 LISS III² and ALOS AVNIR-2 optical sensor data. Within these projects only the Intensity Based Matching to extract GCP are applied (RD-05)

11.2.1 Image2006

The GMES (Global Monitoring for Environment and Security) Fast Track Land monitoring Service (FTLS) is a service to provide on a regular basis land cover and land use change datasets, which can be used by a wide range of downstream services at European, national, regional and local scale. Under ESA contract DLR (German Aerospace Center) produced two multi-temporal datasets of orthorectified images covering the participating EU27 and neighboring countries (overall 38 countries). Two complete European coverages consisting of about 3700 scenes have been processed for the reference year 2006 (+/- 1 year) (referred to as Image2006). The orthorectified products are derived from a mixture of high-resolution satellite images from SPOT 4 HRVIR with 20 m GSD, SPOT 5 HRG with 10 m GSD and IRS-P6 LISS III with 23 m GSD, each with four spectral bands. About 95 % of the images could be automatically processed.

For the countries, which took part in the Image2000³ project, the reference images are the orthorectified panchromatic images derived from Landsat 7 Enhanced Thematic Mapper ETM+ imagery given in geographic projection with a resolution of 0.000115° and an accuracy of about 9-15 m RMSE_x and 7-18 m RMSE_y (except for Austria with 52 m RMSE_x and 27 m RMSE_y). For all other countries the USGS ETM+ Land Cover dataset given in UTM projection with a resolution of 28.5 m and a global accuracy of about 50 m RMSE_{xy} serves as absolute reference. It is noted that the geometric accuracy of the USGS ETM+ Land Cover dataset is for the European area is better than the official RMSE value, which is related on a global scale.

The DEM database is derived from SRTM-C band Version 2 of NASA and improved by using inputs from MONAPRO, GLOBE and SRTM-X band DEM within a fusion process. Parts of the DEM dataset are manually edited to remove blunder areas. The DEM is given in geographic projection (geodetic datum WGS84) with 1 arcsec planar resolution (~30 m) with ellipsoid heights. The height accuracy (1 σ) of the DEM is about 6m in flat areas and up to 30 m in mountainous areas. In the Alps greater parts of MONAPRO and in east Turkey greater parts of GLOBE has to be used.

¹ © CNES 2007 Distribution Spot Image S.A., France, all rights reserved; produced by DLR/Metria – data provided under an ESA contract for FTS LM IMAGE2006

² © ANTRIX Corporation Limited 2007, Distribution by Euromap GmbH, Germany, all rights reserved; produced by DLR/Metria - data provided under an ESA contract for FTS LM IMAGE2006

³ © European Communities, Source: Joint Research Centre IMAGE2000, based on Landsat 7 ETM+ © ESA, distributed by Eurimage; ortho-correction EU15 © Metria, ortho-correction other countries GISAT; mosaic production GISAT

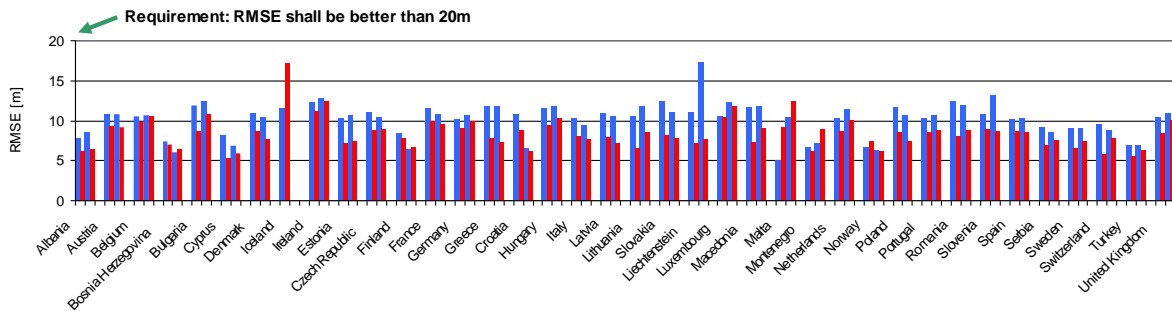


Figure 11-1 Geometric accuracy (RMSE) of Image2006 products w.r.t. reference images (relative accuracy). $RMSE_x$ (blue) and $RMSE_y$ (red) for European coverage 1 (first two columns of country) and European coverage 2 (last two columns of country)

Relative Geometric Accuracy

Figure 11-1 shows the results broken down into the processed countries and the two coverages. The first two columns of each country show the RMS errors in x (east) and y (north) direction for the first coverage. The last two columns are valid for the second coverage. For SPOT4/5 and IRS-P6 orthorectified scenes an overall geometric accuracy with respect to the reference images (relative error) of about 10 m RMSE in each direction ($RMSE_{xy}=13.2$ m) is reached (for Spot4/5: $RMSE_x=10.4$ m, $RMSE_y=8.6$ m, $RMSE_{xy}=13.6$ and for IRSP6: $RMSE_x=9.7$ m, $RMSE_y=8.0$ m, $RMSE_{xy}=12.6$), which corresponds to half a pixel size. It has to be considered that for Spot, unlike for IRSP6, an oblique view up to 30° is possible, so that DEM errors influence the geometric accuracy of the orthoimages generated from Spot. The mean number of ICPs used for quality assessment is 5496 points per scene for IRS-P6 and 1360 points per scene for SPOT 4/5 that is an average of 450 tie points per 1000 km².

Absolute Geometric Accuracy

The absolute accuracy has been manually investigated using maps of scale 1:10.000 to 1:50.000 for different areas in Europe. In this case also the absolute geometric accuracy is of same magnitude as the relative error (see Table 11-2).

Table 11-2 Absolute geometric accuracy for different zones in Europe determined by different operators to increase the reliability.

Zone	Operator	$RMSE_{xy}$ [m] $RMSE_x$ [m] , $RMSE_y$ [m]	N	Reference Source	Scale
Paris France	#1	11.3 6.7 9.1	30	Topo France GARMIN	1:25000
Madrid Spain	#1	15.4 14.3 5.7	13	Topo Espana GARMIN	1:25000
Madrid Spain	#2	15.8 9.0 12.9	20	Topo Espana GARMIN	1:25000
Montpellier France	#1	13.8 11.5 7.6	20	Topo France GARMIN	1:25000
Amiens France	#1	13,0 4.28 12.31	20	Topo France GARMIN	1:25000

Prag Czech Rep.	#1	12.7 10.3 7.4	20	Topo Czech GARMIN	1:10000
Olomouc Czech Rep.	#1	15.7 10.6 11.6	20	Topo Czech GARMIN	1:10000
Rom Italy	#1	14.4 9.9 10.5	17	Land Navigator Italia GARMIN	1:50000
Rom Italy	#2	16.5 5.4 15.6	20	Land Navigator Italia GARMIN	1:50000
Milano Italy	#1	14.4 8.6 11.5	14	Land Navigator Italia GARMIN	1:50000
Ortueri Italy	#1	12.5 11.6 4.7	16	Land Navigator Italia GARMIN	1:50000
Rzeszow Poland	#1	23.5 19.5 13.05	17	TerraSAR-X	
Marseille France	#1	12.2 7.8 9.4	17	Topo France GARMIN	1:25000
Marseille France	#2	7,1 3.1 6.3	18	TerraSAR-X	
Wessling Germany	#3	8.5 6.3 5.6	34	Arial Orthophoto	
Chiemsee Germany	#3	7.4 4.2 6.1	87	Arial Orthophoto	

11.2.2 UrbanAtlas

The GMES Land Information Service Urban Atlas provides detailed knowledge of urban land use, which is essential for monitoring and analyzing changes on a geolocated basis. Amongst other Earth Observation data the ALOS AVNIR-2 serve as input to compile major European cities and larger urban zones. The 4-channel multispectral instrument AVNIR-2 has a spatial resolution of 10 m with a across track pointing capability of 44°.

As reference image database the previously described Image2006 served as input. The relative geometric accuracy assessment is again based on the automatic extracted ICP. The number of extracted ICP varies for each image between 26 and 27515 with a mean number of approximately 5000 ICP per AVNIR-2 scene.

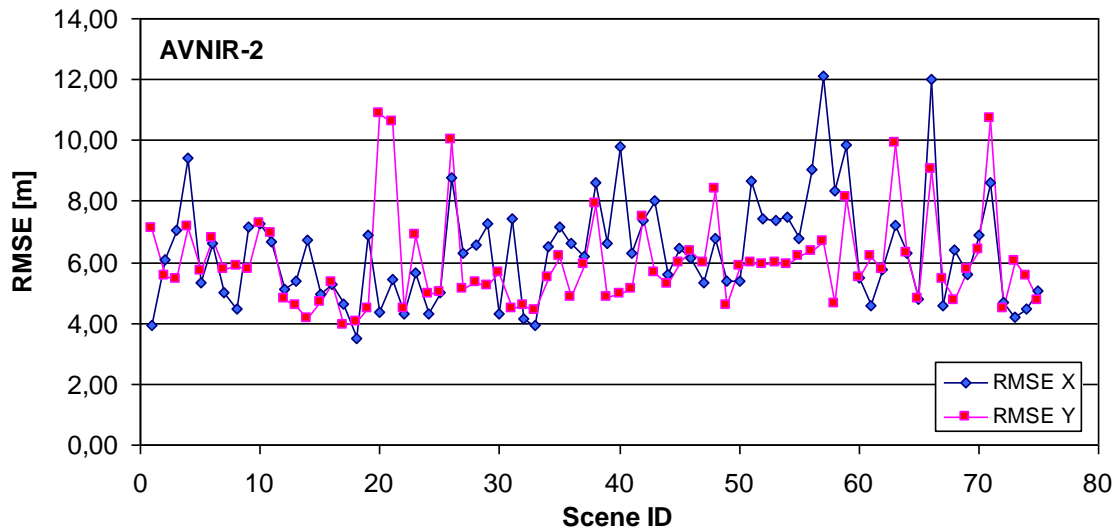


Figure 11-2 Geometric accuracy (RMSE) of ALOS AVNIR-2 orthorectified scenes w.r.t. reference images (relative accuracy). RMSE_x (blue) and RMSE_y (red)

The RMSE values in X-direction are between 3.5 m and 12.1 m and in Y-direction between 3.9 m and 10.7 m. That means that the geometric accuracy of the orthorectified AVNIR-2 scenes with respect to the used reference is in the order of about one pixel or better (see Figure 11-2)

12. Output

The following output is generated by the L1C processor

- Invoked by L0 processing
 - Boresight angles between HSI and body coordinate frame derived from a datatake if applicable
 - Orthorectified quicklooks as specified in AD-08
 - Quality indicators as specified in AD-21 and chapter 9
 - Metadata as specified in AD-08
- For L1C product generation
 - Orthorectified VNIR and SWIR tiles merged to one co-registered image
 - Transformed quality mask congruent to orthorectified scene
 - Metadata as specified in AD-09
 - Resampled DEM congruent to orthorectified scene if applicable (used by L2A processor)

13. Appendix A: Orthogonal Transformations (Basics)

Notation: The lower indices of vectors (bold lower case letters, for example: \mathbf{r} , \mathbf{a} , ...) indicate the position of the points, whereas the upper indices denote the coordinate frame in which the vector is measured. Missing lower indices denote an arbitrary vector. The notation of the indices of transformation matrices (bold capital letter, for example: \mathbf{R} , \mathbf{T} , ...) indicates the transformation direction where the lower index represents the source system and the upper index the destination system. Missing indices denote an arbitrary transformation matrix.

Consider a three dimensional Cartesian coordinate frame denoted by the index t . An arbitrary point can be described by the vector $\mathbf{r}^t = (x_1^t, x_2^t, x_3^t)^T$. Expressing the vector with the three orthonormal unit vectors \mathbf{u}_j^t , with $\mathbf{u}_j^t \cdot \mathbf{u}_i^t = \delta_{ji}$ ¹, that span the vector space one can write

$$\mathbf{r}^t = \sum_j x_j^t \mathbf{u}_j^t \tag{13-1}$$

where the components x_j^t are given by the scalar product (orthogonal projection onto the basis vectors)

$$x_j^t = \mathbf{r}^t \cdot \mathbf{u}_j^t = |\mathbf{r}^t| \cos(\mathbf{r}^t, \mathbf{u}_j^t) \tag{13-2}$$

Now consider a second set of unit basis vectors \mathbf{v}_k^s , with $\mathbf{v}_k^s \cdot \mathbf{v}_i^s = \delta_{ki}$, spanning the Cartesian frame with the same origin denoted by the index s . Expanding the basis vectors \mathbf{u}_j^t in the s -frame yields

$$\mathbf{u}_j^t = \sum_k c_{kj}^s \mathbf{v}_k^s \tag{13-3}$$

The vector \mathbf{r}^t now can be expressed in the s -frame, denoted by \mathbf{r}^s with

$$\mathbf{r}^s = \sum_j x_j^t (\sum_k c_{kj}^s \mathbf{v}_k^s) = \sum_k (\sum_j x_j^t c_{kj}^s) \mathbf{v}_k^s \tag{13-4}$$

Therefore the components of the vector $\mathbf{r}^s = (x_1^s, x_2^s, x_3^s)^T$ are given by

$$x_k^s = \sum_j x_j^t c_{kj}^s \tag{13-5}$$

which can be also written in matrix notation (omitting the upper index of the matrix elements)

$$\mathbf{r}^s = \begin{pmatrix} x_1^s \\ x_2^s \\ x_3^s \end{pmatrix} = \begin{pmatrix} c_{11} & c_{12} & c_{13} \\ c_{21} & c_{22} & c_{23} \\ c_{31} & c_{32} & c_{33} \end{pmatrix} \cdot \begin{pmatrix} x_1^t \\ x_2^t \\ x_3^t \end{pmatrix} = \mathbf{R}_t^s \cdot \mathbf{r}^t \tag{13-6}$$

or

$$\mathbf{r}^s = (\mathbf{u}_1^s \quad \mathbf{u}_2^s \quad \mathbf{u}_3^s) \cdot \begin{pmatrix} x_1^t \\ x_2^t \\ x_3^t \end{pmatrix} \tag{13-7}$$

Multiplying equation (11-3) with the basis vectors \mathbf{v}_k^s the matrix elements c_{kj}^s are

$$\mathbf{v}_k^s \cdot \mathbf{u}_j^t = \cos(\mathbf{v}_k^s, \mathbf{u}_j^t) = c_{kj}^s \tag{13-8}$$

These nine direction cosines $c_{kj}^s = \cos(\mathbf{v}_k^s, \mathbf{u}_j^t)$ fully describe the orientation between the two Cartesian coordinate frames. The direction cosines also give the relation between the coordinates of vectors expressed in the different frames. It is noted, that for this kind of transformation only three independent parameters are necessary and therefore the direction cosines are not independent. Because the length of a vector is not changed by the transformation it can be shown, that \mathbf{R}_t^s is an orthogonal matrix².

¹ The definition of the discrete Kronecker delta is $\delta_{ji} = \begin{cases} 1 & \text{for } j = i \\ 0 & \text{for } j \neq i \end{cases}$

² Using Einstein summation convention the invariance of the length of the vector during an orthogonal transformation can be written $\mathbf{X}_k^s \cdot \mathbf{X}_k^s = \mathbf{X}_k^t \cdot \mathbf{X}_k^t$. With (7-5) it follows

$\mathbf{X}_k^s \cdot \mathbf{X}_k^s = (c_{kj}^s x_j^t)(c_{ki}^s x_i^t) = c_{kj}^s (x_j^t c_{ki}^s) x_i^t = c_{kj}^s (c_{ki}^s x_j^t) x_i^t = c_{kj}^s c_{ki}^s x_j^t x_i^t$. In order to hold the condition it follows $c_{kj}^s c_{ki}^s = \delta_{ji}$

$$\mathbf{R}_t^{s^{-1}} = \mathbf{R}_t^T = \mathbf{R}_s^t \quad 13-9$$

The transformation of a matrix can be derived as follows. Consider a linear mapping in the s-frame, given by $\mathbf{y}^s = \mathbf{A}^s \cdot \mathbf{x}^s$, then with (11-6) and (11-9) it is obtained:

$$\mathbf{R}_t^s \mathbf{y}^t = \mathbf{A}^s \mathbf{R}_t^s \mathbf{x}^t \quad 13-10$$

$$\mathbf{y}^t = \mathbf{R}_s^t \mathbf{A}^s \mathbf{R}_t^s \mathbf{x}^t = \mathbf{A}^t \mathbf{x}^t \quad 13-11$$

which leads to

$$\mathbf{A}^t = \mathbf{R}_s^t \mathbf{A}^s \mathbf{R}_t^s \quad 13-12$$

Assuming the orthogonal transformations **B**, **C** and **D** then generally the composed transformation is not commutative,

$$\mathbf{B} \cdot \mathbf{C} \neq \mathbf{C} \cdot \mathbf{B} \quad 13-13$$

associative

$$\mathbf{B} \cdot (\mathbf{C} \cdot \mathbf{D}) = (\mathbf{B} \cdot \mathbf{C}) \cdot \mathbf{D} \quad 13-14$$

and the following holds.

$$(\mathbf{B} \cdot \mathbf{C})^T = \mathbf{C}^T \cdot \mathbf{B}^T \quad 13-15$$

It is noted, that a composed orthogonal transformation is again an orthogonal transformation. Till now the transformation matrix was considered to act on the coordinate frame and the vector was not changed (only the representation in the different frames), but the transformation matrix can be also regarded as operator, which acts on the vector itself (changing the vector components in the same coordinate frame). The formalism is the same, except that the transformation direction is reverse.

It is noted, that throughout the text the transformation acts on the coordinate frame.

The relative orientation of two Cartesian coordinate frames can be described in addition to the nine direction cosines by three Euler angles^{1.}, where the rotation matrix \mathbf{R}_s^t is a sequence of the basic rotations around the axes x, y and z.

$$\mathbf{R}_x(\omega) = \begin{pmatrix} 1 & 0 & 0 \\ 0 & \cos \omega & \sin \omega \\ 0 & -\sin \omega & \cos \omega \end{pmatrix}, \mathbf{R}_y(\phi) = \begin{pmatrix} \cos \phi & 0 & -\sin \phi \\ 0 & 1 & 0 \\ \sin \phi & 0 & \cos \phi \end{pmatrix}, \mathbf{R}_z(\kappa) = \begin{pmatrix} \cos \kappa & \sin \kappa & 0 \\ -\sin \kappa & \cos \kappa & 0 \\ 0 & 0 & 1 \end{pmatrix} \quad 13-16$$

For a right handed coordinate system a positive angle describes a counterclockwise rotation from the source to the destination frame when looking along the positive rotation axis to the origin of the coordinate system.

, which is the orthogonality condition (meaning that the columns or rows of the transformation matrix are orthonormal basis vectors). The inverse transformation can be written to

$$\mathbf{x}_k^s = \mathbf{C}_{kj}^s \mathbf{x}_j^t = \mathbf{C}_{kj}^s (\mathbf{C}_{ji}^t \mathbf{x}_i^s) = \mathbf{C}_{kj}^s \mathbf{C}_{ji}^t \mathbf{x}_i^s, \text{ which only holds if } \mathbf{C}_{kj}^s \mathbf{C}_{ji}^t = \delta_{ki}. \text{ This is in matrix notation}$$

$$\mathbf{R}_t^s \mathbf{R}_s^t = \mathbf{R}_t^s \mathbf{R}_t^{s^{-1}} = \mathbf{I}, \text{ with } \mathbf{I} \text{ the unit matrix. Assuming the summation } \mathbf{C}_{kl}^s \mathbf{C}_{kl}^s \mathbf{C}_{ij}^t, \text{ then with the orthogonality}$$

condition and the inverse matrix it follows $\mathbf{C}_{kl}^s \mathbf{C}_{kl}^s \mathbf{C}_{ij}^t = \delta_{ij} \mathbf{C}_{ij}^t = \delta_{ij} \mathbf{C}_{kl}^s$, which means $\mathbf{C}_{ij}^t = \mathbf{C}_{ij}^s$ the transpose of an orthogonal transformation is the inverse transformation

The commonly used term for the angles of sequential rotations, meaning rotations around the already rotated axes, are Euler angles. This is also the definition here. Sometimes in literature the above angles of the basic rotations are called Cardan angles, which are normally used in technique scope, whereas Euler angles are defined by a rotation sequence, where one rotation axis is used twice. For example first rotating around z, second rotating around x and finally rotating again around z (short form: 3-1-3). This definition is normally used in physics.

From the resulting transformation matrix the Euler angles (ω, ϕ, κ) can be directly recalculated from the matrix elements c_{ij} (see Appendix C).

Every sequence of rotations can be reduced to a sequence of these three basic rotations by comparison of the matrix elements, which leads to the three basic rotation angles.

Assuming small rotation angles the first order approximation for the sine and cosine terms of the rotation matrix elements can be used

$$\mathbf{R}_x(d\omega) \cdot \mathbf{R}_y(d\phi) \cdot \mathbf{R}_z(d\kappa) \approx \begin{pmatrix} 1 & d\kappa & -d\phi \\ -d\kappa & 1 & d\omega \\ d\phi & -d\omega & 1 \end{pmatrix} = \mathbf{I} - \Psi \quad 13-17$$

where \mathbf{I} the unit matrix and Ψ the skew matrix of small rotation angles. The rotation sequence around the axes does not affect the result of the rotation using the small angle approximation. A vector transforms therefore in the small angle approximation

$$\mathbf{r}^s = \mathbf{R}_t^s \mathbf{r}^t \approx (\mathbf{I} - \Psi) \cdot \mathbf{r}^t = \mathbf{r}^t - \Psi \times \mathbf{r}^t \quad 13-18$$

where $\Psi^t = (d\omega, d\phi, d\kappa)^T$ is a axial or pseudo vector of the (infinitesimal) rotation angles.

For angular rates describing the relative orientation of two frames with respect to time the time derivate of the transformation equation is build

$$\mathbf{v}^s = \frac{d\mathbf{r}^s}{dt} = \mathbf{R}_t^s \cdot \frac{d\mathbf{r}^t}{dt} + \frac{d\mathbf{R}_t^s}{dt} \cdot \mathbf{r}^t \quad 13-18$$

Where the differential term $d\mathbf{R}_t^s$ is the difference between the rotation at time $t+dt$ and time t . The rotation at time $t+dt$ is described by the additional rotation around infinitesimal angles

$$d\mathbf{R}_t^s = \mathbf{R}_t^s(t+dt) - \mathbf{R}_t^s(t) = (\mathbf{I} - \Psi) \cdot \mathbf{R}_t^s - \mathbf{R}_t^s = -\Psi \cdot \mathbf{R}_t^s \quad 13-19$$

Therefore the deviation of the transformation matrix is given by

$$\frac{d\mathbf{R}_t^s}{dt} = -\frac{d\Psi}{dt} \cdot \mathbf{R}_t^s = -\Omega_{ts}^s \cdot \mathbf{R}_t^s = \Omega_{st}^s \cdot \mathbf{R}_t^s = \mathbf{R}_t^s \cdot \Omega_{st}^t \quad 13-20$$

with the skew matrix

$$\Omega_{st}^t = \begin{pmatrix} 0 & -\omega_3 & \omega_2 \\ \omega_3 & 0 & -\omega_1 \\ -\omega_2 & \omega_1 & 0 \end{pmatrix} = \begin{pmatrix} 0 & -\frac{d\kappa}{dt} & \frac{d\phi}{dt} \\ \frac{d\kappa}{dt} & 0 & -\frac{d\omega}{dt} \\ -\frac{d\phi}{dt} & \frac{d\omega}{dt} & 0 \end{pmatrix}$$

13-21

of the angular velocity of the t-frame around the s-frame coordinated in the t-frame. This can also be written with the cross-product operator

$$\Omega_{st}^t = \langle \omega_{st}^t \times \rangle \quad \text{with } \omega = (\omega_1, \omega_2, \omega_3)^T \quad 13-22$$

The final transformation, which is actually the well known Coriolis law, is then given by

$$\mathbf{v}^s = \mathbf{R}_t^s \cdot (\mathbf{v}^t + \Omega_{st}^t \cdot \mathbf{r}^t) = \mathbf{R}_t^s \cdot (\mathbf{v}^t + \omega_{st}^t \times \mathbf{r}^t) \quad 13-23$$

A quite other description of rotation is the unit quaternion, which is a number represented by a four-dimensional vector in complex space (one real and three imaginary components). The advantage is that possible ambiguous rotations using Euler angles are eliminated.

14. Appendix B: Definitions of Coordinate Frames and Transformations

In order to describe positions of points related to the earth a Cartesian coordinate system with mutually orthogonal, right handed axes are in common use. Origin, orientation and scaling define this system. Several realizations (coordinate frames) of a Cartesian coordinate system are defined in order to describe locations on or near the earth. In geodesy also a lot of map projections are in use, which transforms the earth surface to a 2-dimensional space preserving partially direction, scale, distance or area. Additionally in photogrammetry and navigation some other coordinate frames, like the body, navigation (orbital) or sensor frame have to be introduced.

14.1 Geocentric Earth Fixed Cartesian Coordinate frame (ECEF or ECR)

The geocentric Cartesian coordinate system is fixed to the earth. It is a three dimensional Cartesian coordinate systems with origin at the centre of mass (including the atmosphere) of the earth. The z-axis is directed to the north pole along the mean rotation axis of the earth (CTP: Conventional Terrestrial Pole) and the related equatorial plane serves as the x-y plane where the x-z plane passes through Greenwich defined by the Bureau International de l'Heure (BIH) and the y axis completes the right handed coordinate system. The WGS84 (World Geodetic System 1984) or the ITRF90 (International Reference Frame 1990) are ECEF frames (also called Conventional Terrestrial System CTS). The IERS (International Earth Rotation Service) establishes such ECEF frames.

14.2 Ellipsoidal Geographic Coordinate Frame

The geographic coordinate frame describes positions of points in terms of the curvilinear coordinates longitude λ and latitude ϕ and the ellipsoidal height h . It is a local orthogonal system. The origin is the earth's centre of mass. The latitude ϕ is measured in the meridian plane between the equatorial plane and the normal of the ellipsoid surface and counts positive north of the equator plane from 0° to 90° and negative south of the equator plane from 0° to -90° . The longitude λ is measured in the equatorial plane with respect the zero meridian (mean Greenwich) and counts positive east from -180° to $+180^\circ$. If the height h is the length of the normal to the reference ellipsoid it is called ellipsoidal height (only in this case a unique transformation to geocentric coordinates exists). If the height h is the length of the normal to the geoid (or mean sea level) it is called geoid height (in this case the undulation has to be added to the height to obtain ellipsoidal heights for transformations between geocentric coordinates).

14.3 Local Topocentric Frame (LTS)

A local topocentric frame is a Cartesian coordinate system with an arbitrary point on the ellipsoid surface (or below or above) as origin (Index FP: fundamental point). The z-axis is perpendicular to the ellipsoid surface at the fundamental point, the y-axis is directed to north and the x-axis is directed to east. For navigation purpose a LTS with moving fundamental point according to the sensor carrying platform provides determination of the local orientation of the platform (by definition only the z-component could be non zero in this case). For orthoimage generation a LTS with earth fixed fundamental point, normally located at the centre of the area of interest, is used as Cartesian model coordinate frame.

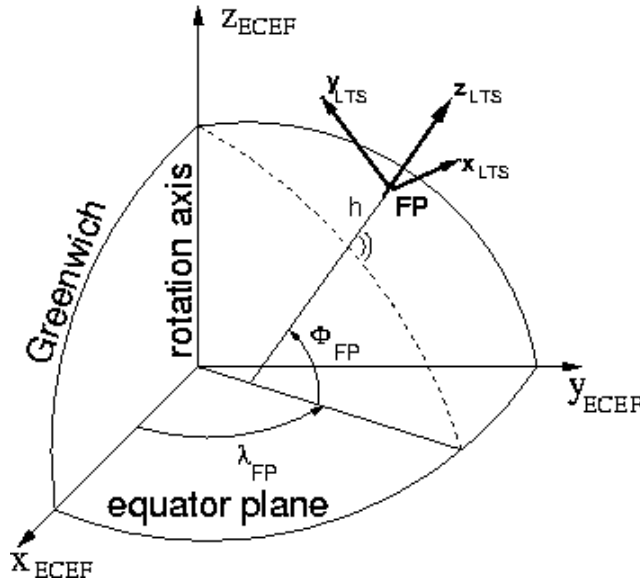


Figure 14-1 Definition of local topocentric system (LTS) and earth centered earth fixed (ECEF) co-ordinate system

14.4 Transformation between Geographic and Geocentric Coordinate Frames

The geographic coordinates, given by longitude λ , latitude ϕ and ellipsoidal height h , can be transformed to geocentric coordinates by

$$\mathbf{r}^{ECEF} = \begin{pmatrix} x^{ECEF} \\ y^{ECEF} \\ z^{ECEF} \end{pmatrix} = \begin{pmatrix} (N(\phi) + h) \cdot \cos \phi \cdot \cos \lambda \\ (N(\phi) + h) \cdot \cos \phi \cdot \sin \lambda \\ ((1 - e^2) \cdot N(\phi) + h) \cdot \sin \phi \end{pmatrix} \quad 14.4-1$$

and the inverse transformation (one of the possible solutions) from geocentric to geographic coordinates

$$\phi = \operatorname{atan} \left(\frac{z^{ECEF} + e^2 \cdot b \cdot \sin^3 \xi}{\sqrt{x^{ECEF^2} + y^{ECEF^2} - e^2 \cdot a \cdot \cos^3 \xi}} \right) \quad 14.4-2$$

$$\lambda = \operatorname{atan} \left(\frac{y^{ECEF}}{x^{ECEF}} \right) \quad 14.4-3$$

$$h = \frac{\sqrt{x^{ECEF^2} + y^{ECEF^2}}}{\cos \phi} - N(\phi) \quad 14.4-4$$

$$\text{with } e^2 = \frac{a^2 - b^2}{a^2}, \quad e'^2 = \frac{a^2 - b^2}{b^2}, \quad \xi = \operatorname{atan} \left(\frac{z^{ECEF} \cdot a}{\sqrt{x^{ECEF^2} + y^{ECEF^2} \cdot b}} \right), \quad N(\phi) = \frac{a}{\sqrt{1 - e^2 \cdot \sin^2 \phi}}$$

14.4-5

14.5 Transformation between Geocentric (ECR) and Local Topocentric (LTS) Coordinate Frame

The geocentric coordinates of \mathbf{r}^{ECR} (ECR: earth centered rotated) can be transformed to local topocentric coordinates (LTS) of \mathbf{r}^{LTS} with the fundamental point \mathbf{r}_{FP}^{ECR} given in geocentric coordinates and longitude λ_{FP} and latitude ϕ_{FP} of the fundamental point with the same geodetic datum.

$$\mathbf{r}^{LTS} = \mathbf{R}_{ECR}^{LTS} \cdot (\mathbf{r}^{ECR} - \mathbf{r}_{FP}^{ECR}) \quad 14.5-1$$

where

$$\mathbf{R}_{ECR}^{LTS} = \mathbf{R}_x \left(\frac{\pi}{2} - \phi_{FP} \right) \cdot \mathbf{R}_z \left(\lambda_{FP} + \frac{\pi}{2} \right) = \begin{pmatrix} -\sin \lambda_{FP} & \cos \lambda_{FP} & 0 \\ -\sin \phi_{FP} \cdot \cos \lambda_{FP} & -\sin \phi_{FP} \cdot \sin \lambda_{FP} & \cos \phi_{FP} \\ \cos \phi_{FP} \cdot \cos \lambda_{FP} & \cos \phi_{FP} \cdot \sin \lambda_{FP} & \sin \phi_{FP} \end{pmatrix} \quad 14.5-2$$

The vector \mathbf{r}_{FP}^{ECR} to the fundamental point FP expressed in geocentric coordinates is calculated from the longitude λ_{FP} and latitude ϕ_{FP} values of the fundamental point by the transformation formulas described above.

The inverse transformation from LTS coordinates to ECR coordinates is given by

$$\mathbf{r}^{ECR} = (\mathbf{R}_{ECR}^{LTS})^T \cdot \mathbf{r}^{LTS} + \mathbf{r}_{FP}^{ECR} = \mathbf{R}_{LTS}^{ECR} \cdot \mathbf{r}^{LTS} + \mathbf{r}_{FP}^{ECR} \quad 14.5-8$$

14.6 Geodetic Datum

For the description of positions of points on the earth different ellipsoids fitting the earth surface are used. These ellipsoidal reference surfaces are called geodetic datum. Global reference systems like WGS84 are fitting the earth surface in a global manner with an origin at the mass centre of the earth and the axes aligned to the conventional terrestrial system. Local or national reference systems approximate the earth surface best in a certain region of the earth using appropriate ellipsoids with origins normally not located at the mass centre of the earth. The relation between these different reference systems are described by a 7 parameter geodetic datum transformation (a similarity transformation also called Helmert transformation with a translation vector $\Delta \mathbf{r}$, three angles α, β, γ and a scale factor). Normally the transformation parameters are given with respect to the WGS84 system. Therefore a whole datum transformation from XYZ Cartesian coordinates to XYZ' Cartesian coordinates are given by

$$\mathbf{r}^{XYZ} \rightarrow \mathbf{r}^{WGS84} \rightarrow \mathbf{r}^{XYZ'} \quad 14.6-1$$

$$\mathbf{r}^{WGS84} = \Delta \mathbf{r} + (1 - scale) \cdot \mathbf{R}_{XYZ}^{WGS84} \cdot \mathbf{r}^{XYZ} \quad 14.6-2$$

and the reverse transformation

$$\mathbf{r}^{XYZ'} = \frac{1}{1 - scale} \cdot \mathbf{R}_{WGS84}^{XYZ} \cdot (\mathbf{r}^{WGS84} - \Delta \mathbf{r}') \quad 14.6-3$$

with

$$\mathbf{R}_{XYZ}^{WGS84} = (\mathbf{R}_{WGS84}^{XYZ})^T = \begin{pmatrix} \cos \alpha \cos \gamma & \cos \alpha \sin \gamma + \sin \alpha \sin \beta \cos \gamma & \sin \alpha \sin \gamma - \cos \alpha \sin \beta \cos \gamma \\ -\cos \beta \sin \gamma & \cos \alpha \cos \gamma - \sin \alpha \sin \beta \sin \gamma & \sin \alpha \cos \gamma + \cos \alpha \sin \beta \sin \gamma \\ \sin \beta & -\sin \alpha \cos \beta & \cos \alpha \cos \beta \end{pmatrix}$$

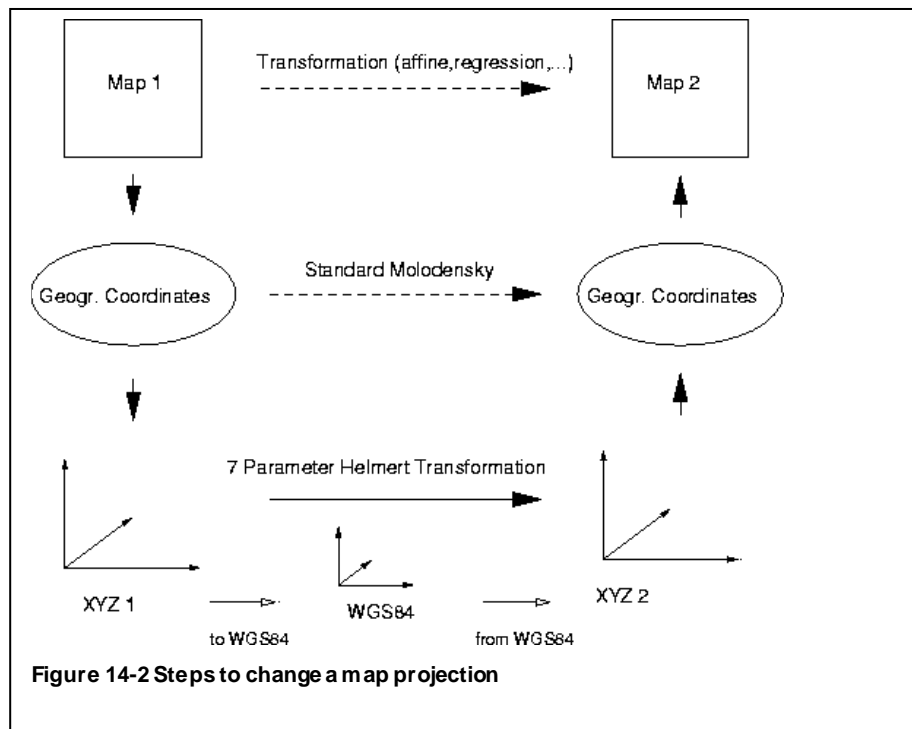
14.6-4

14.7 Map Projections

In general a map projection is a mathematical function, which maps ellipsoidal coordinates onto a plane with easting and northing coordinates ($easting = f_1(\lambda, \varphi)$ and $northing = f_2(\lambda, \varphi)$). This is in general not an orthogonal coordinate system and it occurs a scale change. Furthermore the curved surface of the earth can not be fitted to a plane without introducing some distortions. Only in small regions map projections can be assumed as a metric, orthogonal coordinate frame.

$$\mathbf{r}_{MapProjection2} = F_{MapProjection1}(\mathbf{r}_{MapProjection1})$$

14.7-1



14.8 Geoid and Ellipsoid Heights

Ellipsoids describe the earth surface in a global manner and are used to perform mathematical operation like transformation between coordinate frames. To define a horizontal position on earth, ellipsoid coordinates can be used, whereas for vertical position a reference surface derived from the earth gravity field is more appropriate. Therefore height values are given with respect to a reference surface like a

- geoid that is the equipotential surface of the earth gravity field that most closely approximates the mean sea level surface and is measured along the plumb line,
- ellipsoid that is an approximation of the geometric earth surface at the mean sea level by appropriate ellipsoid parameters and geodetic datum transformations measured perpendicular to the ellipsoid surface.

In image processing digital elevation models (DEM) are used to describe heights on earth. The generic term DEM is divided into

- digital surface models (DSM) describing the heights of the earth ground including permanent objects like buildings and forests.
- digital terrain models (DTM) describing the heights of the soil (ground).

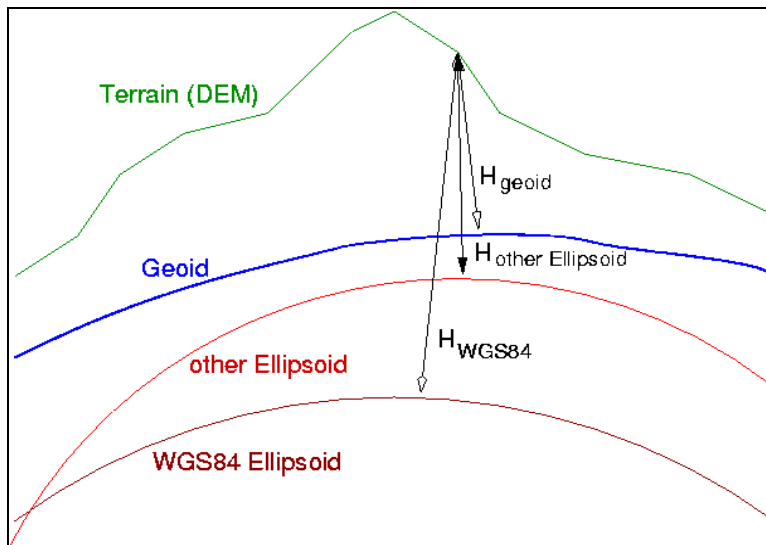


Figure 14-3 Height definitions used for digital elevation models DEM

The difference between geoid and ellipsoid heights are called undulation (U), which range world-wide from -107m to 85m relative to the WGS84 reference system. The Earth Gravitational Model 1996 (EGM96) is one of the latest global models to calculate undulations with respect to WGS84.

In good approximation the relationship between geoid and for example WGS84 ellipsoid heights can be written to

$$H_{WGS84} = H_{geoid} + U_{WGS84} \quad 14.8-1$$

If the undulation is known relative to an ellipsoid i.e. WGS84 the undulation with respect to another ellipsoid at a given point can be calculated using geodetic datum transformations.

$$H_{ellipsoid} = H_{geoid} + U_{WGS84} - \Delta H_{ellipsoid} \quad 14.8-2$$

where $\Delta H_{ellipsoid}$ is the height difference between the WGS84 ellipsoid and another ellipsoid including geodetic datum transformations. For example at the WGS84 coordinates 11.0° E and 48.0° N the undulation U_{WGS84} is 45.70m. The ellipsoid height difference to the Bessel ellipsoid and the Potsdam geodetic datum is -23.51m which leads to an undulation of 69.21m relative to the Potsdam geodetic datum.

For direct georeferencing DEM heights are needed as ellipsoid heights (except in the case of an approximate calculation of airborne imagery). To transform geoid heights to ellipsoid heights of a DEM the used undulation model for the DEM has to be known.

14.9 Quasi Inertial Coordinate Frame (ECI Earth Centered Inertial)

For completeness the inertial coordinate frame, in which Newton's Laws of motion hold, is introduced:

Earth fixed frames are moving and rotating coordinate systems with respect to a space fixed coordinate frame. The shape of a satellite orbit at any instant of time can be approximated with an ellipse in an inertial coordinate system. A realization of a space fixed coordinate system is the ICRF (International Celestial Reference System), with the z axis normal to the mean equatorial plane at the Julian epoch J2000.0 (01.01.2000, 12.00 UT), the x axis to the vernal equinox at this time and the y-axis completes the right hand coordinate system. The mass centre of the earth is the origin of this coordinate system (therefore it is only a quasi inertial system due to accelerations of the earth during movement around the sun). The transformation from the space fixed to the earth fixed system takes into account the movements of the earth polar axis (nutation of about 19 year cycles and precession of about 26000 year cycles), the movements of the polar axis with respect to the earth and the earth rotation.

The transformation matrices from ECI (J2000) to ECR (ITRF89) are provided in the metadata with a repetition rate of 1 Hz. The sequence of transformation is given by

$$\mathbf{R}_{ECI}^{ECR} = \mathbf{R}_{XY} \cdot \mathbf{R}_{GAST} \cdot \mathbf{R}_{PN} \quad 14.8-3$$

with \mathbf{R}_{XY} is the polar motion matrix, \mathbf{R}_{PN} is the nutation and precession matrix and \mathbf{R}_{GAST} accounts for the earth rotation using Greenwich Apparent Sidereal Time.

The transformation of velocity vectors from inertial (ECI) to earth rotating (ECR or ECEF) frame is given by

$$\mathbf{v}^{ECR} = \frac{d}{dt} (\mathbf{R}_{ECI}^{ECR} \mathbf{r}^{ECI}) = \mathbf{R}_{ECI}^{ECR} \mathbf{v}^{ECI} + \frac{d\mathbf{R}_{ECI}^{ECR}}{dt} \mathbf{r}^{ECI} \quad 14.8-4$$

15. Appendix C: Composed Rotation Matrix and Rotation Angle Extraction

The sequence of the three basic rotations around the axes lead to the following rotation matrices and from the resulting transformation matrix the Euler angles $(\omega, \varphi, \kappa)$ can be directly recalculated from the matrix elements c_{ij} (i:row; j:column).

Rotation Sequence: $R(\omega)R(\varphi)R(\kappa)$		
+cos(φ) cos(κ)	+cos(φ) sin(κ)	-sin(φ)
+sin(ω) sin(φ) cos(κ)-cos(ω) sin(κ)	+sin(ω) sin(φ) sin(κ)+cos(ω) cos(κ)	+sin(ω) cos(φ)
+cos(ω) sin(φ) cos(κ)+sin(ω)sin(κ)	+cos(ω) sin(φ) sin(κ)-sin(ω) cos(κ)	+cos(ω) cos(φ)

Angle Extraction: $\omega = \arctan\left(\frac{c_{23}}{c_{33}}\right)$; $\varphi = \arcsin(-c_{13})$; $\kappa = \arctan\left(\frac{c_{12}}{c_{11}}\right)$

Rotation Sequence: $R(\varphi)R(\omega)R(\kappa)$		
+cos(φ) cos(κ)-sin(φ)sin(ω) sin(κ)	+cos(φ) sin(κ)+sin(φ)sin(ω) cos(κ)	-sin(φ) cos(ω)
-cos(ω) sin(κ)	+cos(ω) cos(κ)	+sin(ω)
+sin(φ) cos(κ)+cos(φ) sin(ω)sin(κ)	+sin(φ) sin(κ)-cos(φ) sin(ω) cos(κ)	+cos(φ) cos(ω)

Angle Extraction: $\omega = \arcsin(c_{23})$; $\varphi = \arctan\left(-\frac{c_{13}}{c_{33}}\right)$; $\kappa = \arctan\left(-\frac{c_{21}}{c_{22}}\right)$

Rotation Sequence: $R(\varphi)R(\kappa)R(\omega)$		
+cos(φ) cos(κ)	+cos(φ) sin(κ) cos(ω)+sin(φ)sin(ω)	+cos(φ) sin(κ) sin(ω)-sin(φ) cos(ω)
-sin(κ)	+cos(κ) cos(ω)	+cos(κ) sin(ω)
+sin(φ) cos(κ)	+sin(φ) sin(κ) cos(ω)-cos(φ) sin(ω)	+sin(φ) sin(κ) sin(ω)+cos(φ) cos(ω)

Angle Extraction: $\omega = \arctan\left(\frac{c_{23}}{c_{22}}\right)$; $\varphi = \arctan\left(\frac{c_{31}}{c_{11}}\right)$; $\kappa = \arcsin(-c_{21})$

Rotation Sequence: $R(\kappa)R(\varphi)R(\omega)$		
+cos(κ) cos(φ)	+sin(κ) cos(ω)+cos(κ) sin(φ)sin(ω)	+sin(κ) sin(ω)-cos(κ) sin(φ) cos(ω)
-sin(κ) cos(φ)	+cos(κ) cos(ω)-sin(κ)sin(φ) sin(ω)	+cos(κ) sin(ω)+sin(κ)sin(φ) cos(ω)
+sin(φ)	-cos(φ) sin(ω)	+cos(φ) cos(ω)

Angle Extraction: $\omega = \arctan\left(-\frac{c_{32}}{c_{33}}\right)$; $\varphi = \arcsin(c_{31})$; $\kappa = \arctan\left(-\frac{c_{21}}{c_{11}}\right)$

Rotation Sequence: $R(\omega)R(\kappa)R(\varphi)$		
+cos(κ) cos(φ)	+sin(κ)	-cos(κ) sin(φ)
-cos(ω) sin(κ) cos(φ)+sin(ω) sin(φ)	+cos(ω) cos(κ)	+cos(ω) sin(κ)sin(φ)+sin(ω) cos(φ)
+sin(ω)sin(κ) cos(φ)+cos(ω) sin(φ)	-sin(ω) cos(κ)	-sin(ω)sin(κ) sin(φ)+cos(ω) cos(φ)

Angle Extraction: $\omega = \arctan\left(-\frac{c_{32}}{c_{22}}\right)$; $\varphi = \arctan\left(-\frac{c_{13}}{c_{11}}\right)$; $\kappa = \arcsin(c_{12})$



Rotation Sequence: $R(\kappa)R(\omega)R(\phi)$		
$+\cos(\kappa) \cos(\phi)+\sin(\kappa) \sin(\omega) \sin(\phi)$	$+\sin(\kappa) \cos(\omega)$	$-\cos(\kappa) \sin(\phi)+\sin(\kappa) \sin(\omega) \cos(\phi)$
$-\sin(\kappa) \cos(\phi)+\cos(\kappa) \sin(\omega) \sin(\phi)$	$+\cos(\kappa) \cos(\omega)$	$+\sin(\kappa)\sin(\phi)+\cos(\kappa) \sin(\omega) \cos(\phi)$
$+\cos(\omega) \sin(\phi)$	$-\sin(\omega)$	$+\cos(\omega) \cos(\phi)$

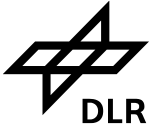
Angle Extraction: $\omega = \arcsin(-c_{32})$; $\phi = \arctan\left(\frac{c_{31}}{c_{33}}\right)$; $\kappa = \arctan\left(\frac{c_{12}}{c_{22}}\right)$



16. List of On-Going TBC & TBD

TBC To Be Confirmed
TBD To Be Determined

Number	Type	Topic	Status	Section	Due



- END OF DOCUMENT -